Liquid Metal Printing

by

Zain Karsan

M.Arch
Massachusetts Institute of Technology, 2018

Submitted to the Department of Architecture and the Department of Mechanical Engineering
in Partial Fulfillment of the Requirements for the Degrees of

Master of Science in Architecture Studies and

Master of Science in Mechanical Engineering

at the

Massachusetts Institute of Technology

JUNE 2023

Authored by: Zain Karsan
Department of Architecture
May 1, 2023

Certified by: Skylar Tibbits
Associate Professor of Design Research
Thesis Supervisor

Certified by: Anette Peko Hosoi
Professor of Mechanical Engineering
Thesis Supervisor

Accepted by: Leslie K. Norford
Professor of Building Technology
Chair, Department of Architecture Committee on Graduate Students

Accepted by: Nicolas Hadjiconstantinou
Professor of Mechanical Engineering
Chair, Department of Mechanical Engineering Committee on Graduate Students

Thesis Supervisors

Skylar Tibbits, SMarchS
Associate Professor of Design Research

Anette Peko Hosoi, PhD
Professor of Mechanical Engineering

and reader

Caitlin Mueller, PhD
Associate Professor of Architecture
Associate Professor of Civil and Environmental Engineering

Liquid Metal Printing

by

Zain Karsan

Submitted to the Department of Architecture and
the Department of Mechanical Engineering
on May 1, 2023, in partial fulfillment of the
requirements for the degrees of
Master of Science in Architecture Studies
and
Master of Science in Mechanical Engineering

Abstract

The pace of worldwide material production and its deleterious effect on the climate motivate the need for materially efficient and sustainable methods of manufacture. Additive manufacturing (AM), commonly referred to as 3D Printing, presents one approach to sustainable manufacturing, affording complexity at high resolution with minimal scrap. For example, polymer, ceramic, and metal materials have been employed in AM to produce parts across industries as varied as aerospace to construction.

Nevertheless, metal AM remains a high-cost process with slow process rates and build environments that are challenging to scale up, impeding the application of these manufacturing techniques but for products for which the cost per volume is significant. Liquid Metal Printing (LMP) is a novel approach to AM that is fast, scalable, and low cost, invented by the Self-Assembly Lab at MIT in 2020. However, this technique is nascent, and has only been developed to print with low melting point alloys that are unsuitable for any realistic use. Notwithstanding, LMP offers a new way of thinking about additive manufacturing by printing large scale, low resolution parts extremely quickly.

Therefore, this thesis explores the redesign of several of the LMP components to print aluminum, describes a set of design rules and toolpath strategies for printing 2.5D multi-layer structures, and proposes several theoretical models for characterizing the print output. Finally, through a selection of case studies, this thesis assesses the applicability of LMP as a coarse resolution, rapid additive manufacturing process in mechanical and product design.

Thesis Supervisor: Skylar Tibbits
Title: Associate Professor of Design Research

Thesis Supervisor: Anette Hosoi
Title: Professor of Mechanical Engineering

Acknowledgments

Thank you to my advisors Peko and Skylar for their generous support.

Thank you Kimball for everything, this thesis wouldn't have been possible without your help.

Thank you Chris for sharing your boundless knowledge with me.

Thank you Natalie and Nolli for your love and patience.

Contents

List of Figures

List of Tables

All images created by author unless otherwise noted.

Chapter 1

Introduction

The building sector accounts for roughly 37% of global energy and process emissions [10]. Roughly 6% amounting to approximately 6Gt of CO_2 in the extraction and processing of building related materials, including concrete, steel and aluminum. In particular, the production of aluminum represents 10% of global emissions, across its numerous applications beyond construction. Metals are among the most prevalent structural materials, second to stone, extracted and produced in large quantities. For these reasons, the efficient and sustainable use of metal is integral to the decarbonization of production related human activity. Furthermore, the lifecycle of materials needs careful consideration to discover opportunities to avoid further extraction and production of virgin material which comes at significant environmental cost.

Consider figure 1-1, which describes the alternatives to purely linear material utilization. Taking less, making less and wasting less involve strategies of material efficiency, eschewing scenarios where significant amounts of material are wasted to produce a finished part. Examples abound in aerospace and automotive industries, where the so-called "buy to fly" ratio is high, referring to the large volume of material necessary to fabricate high performing parts. Such examples involve machining away significant amounts of virgin material to achieve net shape parts. While the embodied energy associated with the process of manufacture may be relatively small depending on the material removal rate (MRR), the decision to reduce entire billets

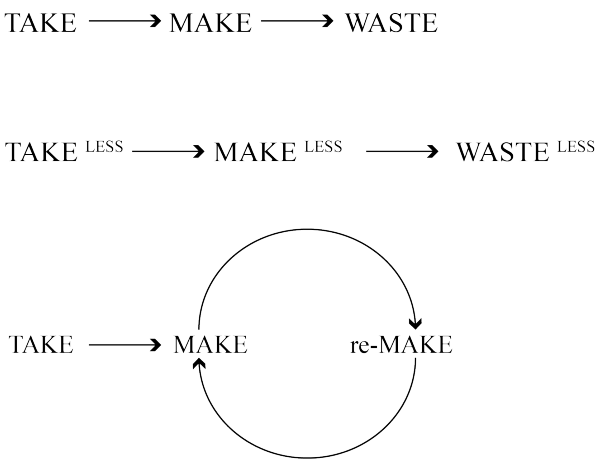

Figure 1-1: Linear and Circular Material Lifecycles

of material to chips comes at a cost, in the case of virgin aluminum for example, of $270\frac{MJ}{kg}$. Therefore the final lifecycle strategy shown in figure 1-1 describes the reuse of material, recast into billets for subsequent processing for example, to reduce the embodied energy of the manufactured part. The machining example is redolent of conventional manufacturing processes which achieve net shape through subtraction. An emerging alternative that has gained significant traction in recent decades is additive manufacturing, in particular with metal materials [2]. This trend is especially evident in industries which require high performance parts, that benefit from complex geometries that are difficult or impossible to achieve with conventional methods [27]. However, the freedom of complexity afforded by additive manufacturing comes at significant material and processing cost, as well as reduced process rate, orders of magnitude slower than conventional manufacturing techniques. To address these shortcomings, a novel manufacturing process was developed by the Self Assembly Lab in collaboration with AISIN © in 2021 called Liquid Metal Printing (LMP) [30]. This process involves the rapid deposition of molten metal into a bed of granular media to produce a form. While similar techniques have been developed that involve the deposition of molten metal through a nozzle following a toolpath, no liquid metal

additive process has utilized a bed of granular media. Instead a heated substrate and an inert environment is used, for example Drop on Demand Liquid Metal Printing (DOD) or Direct Metal Writing (DMW) [11]. Heretofore, Liquid Metal Printing has been tested with pewter, with its associated patent describing the specific process parameters. However a description of how to print with metals that have higher melting points is omitted. Furthermore, the machine configuration described by the patent cannot extend to higher melting point metals without significant revision. Therefore, this thesis will apply the liquid metal printing concept to a higher melting point material, aluminum, which is a commonly used material across a vast array of industries. Furthermore, a description of the process physics underlying Liquid Metal Printing will be presented that aim to generalize the process parameters associated with aluminum to different metals. A series of experiments and analyses have been undertaken to quantify the Liquid Metal Printing process in terms of cost, energy intensity, resolution, performance, and process rate. Finally a selection of applications are identified, with a proof of concept case study demonstrating the potential of Liquid Metal Printing. Hence the structure of the thesis begins with a background which sets LMP against a landscape of metal additive techniques, elaborating a framework for comparison. A brief history of the metal under consideration, aluminum, is presented with potential points of intervention proposed. In chapter 3, the LMP hardware is explained in detail, with illustrations elaborating the redesign of critical components necessary for high temperature metal printing. In chapter 4, an analysis of the thermal and fluid systems underlying the LMP process are presented. Chapter 5 describes a series of experiments aimed at validating the analyses presented in chapter 4, a set of geometric experiments intended to clarify design rules, and mechanical testing to assess the quality of printed components. The results of these experiments are described in chapter 6, and a discussion and next steps follows in chapter 7.

Chapter 2

Background

Manufacturing involves the production of parts and assemblies from raw material, imparting form through a vast array of techniques with different consequences to cost, time and energy. From 2-1 we can infer the range of process rates for each

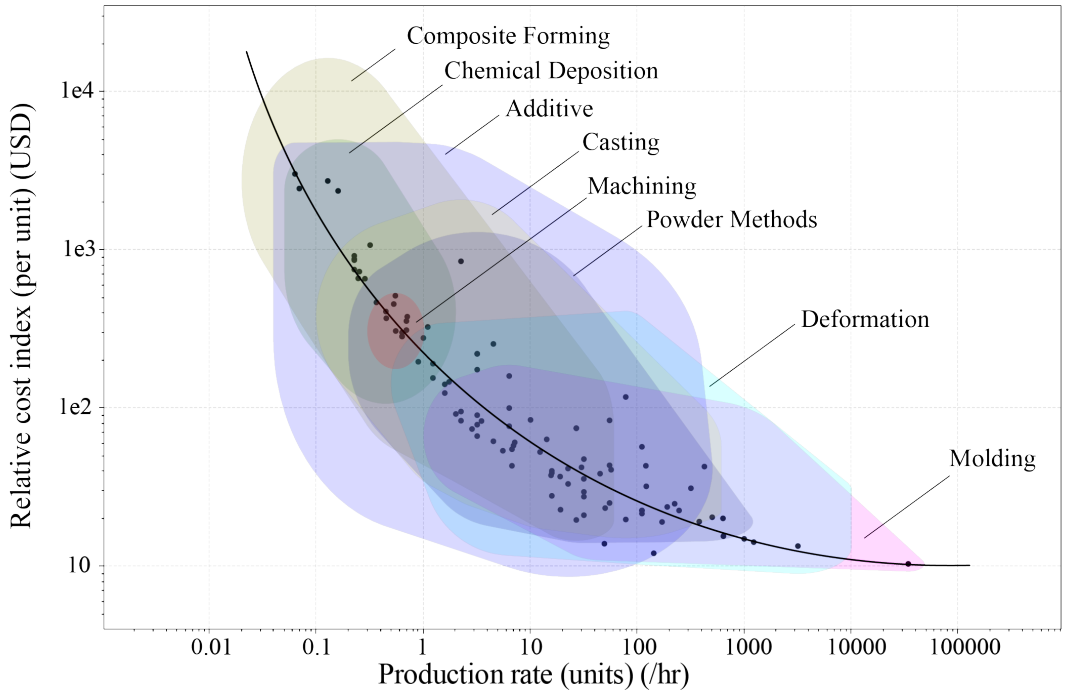

Figure 2-1: Manufacturing Processes
This figure shows the production rate and cost of various manufacturing processes. Typically parallel manufacturing can achieve higher production rates and lower cost per part.

technique can span many orders of magnitude but generally, faster production rates

lead to lower relative cost. This trend is in part, a consequence of the trade-off between customization, typical of serial processes like chemical deposition, composite manufacturing and additive manufacturing and parallel processes which involve the rapid production of several self similar components simultaneously, like die casting and injection molding. Furthermore, if we consider the production of material globally, materials produced in excess of 1 million tons per year are primarily chosen on the basis of their structural capability. Metals, especially steels and aluminum alloys, along with concrete dominate the rightmost corner of the figure, materials typically used in the built environment. Both the embodied energy and the volume of production, in the billions of tons contribute to the location of these materials in figure 2-3. Even natural materials can have significant embodied energy if used in excess, such as balsa used as filler material and insulation. Notwithstanding materials like foams and elastomers produced in the millions of tons, amongst a material's properties, its structural capacity demands the highest volume and is therefore the most environmentally intensive. Hence, the strategy to reduce embodied energy as a consequence

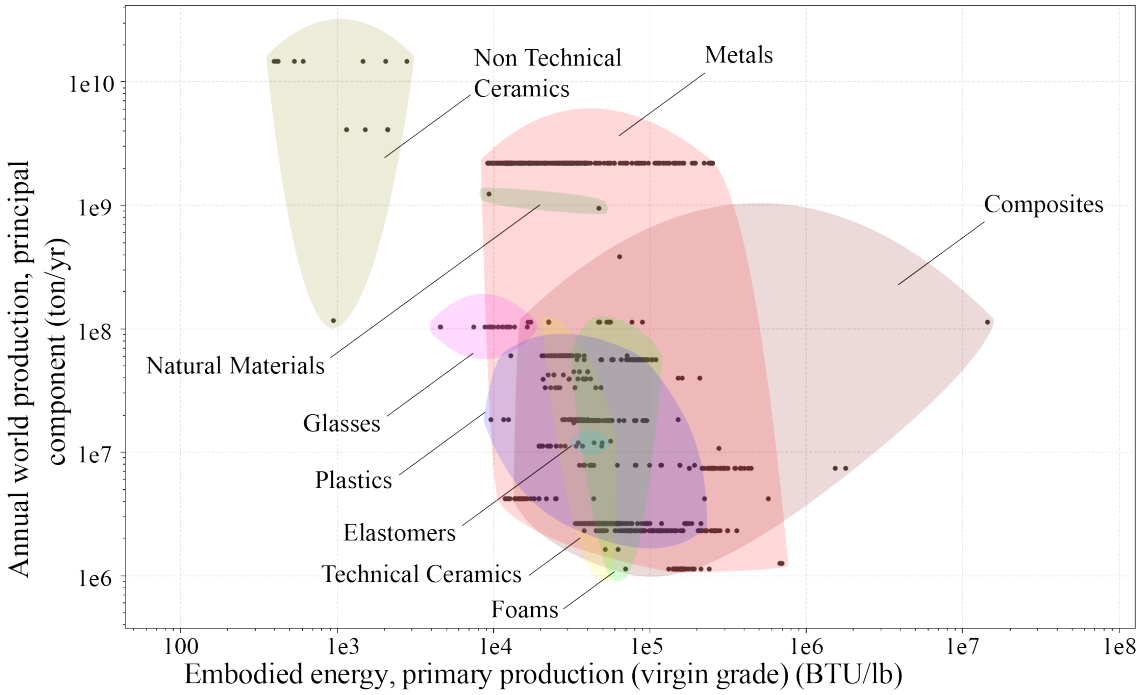

Figure 2-2: Materials produced in excess of 1 Million Tons/Year
Materials produced in the billions of tons per year are non technical ceramics like concrete, and metals like steel.

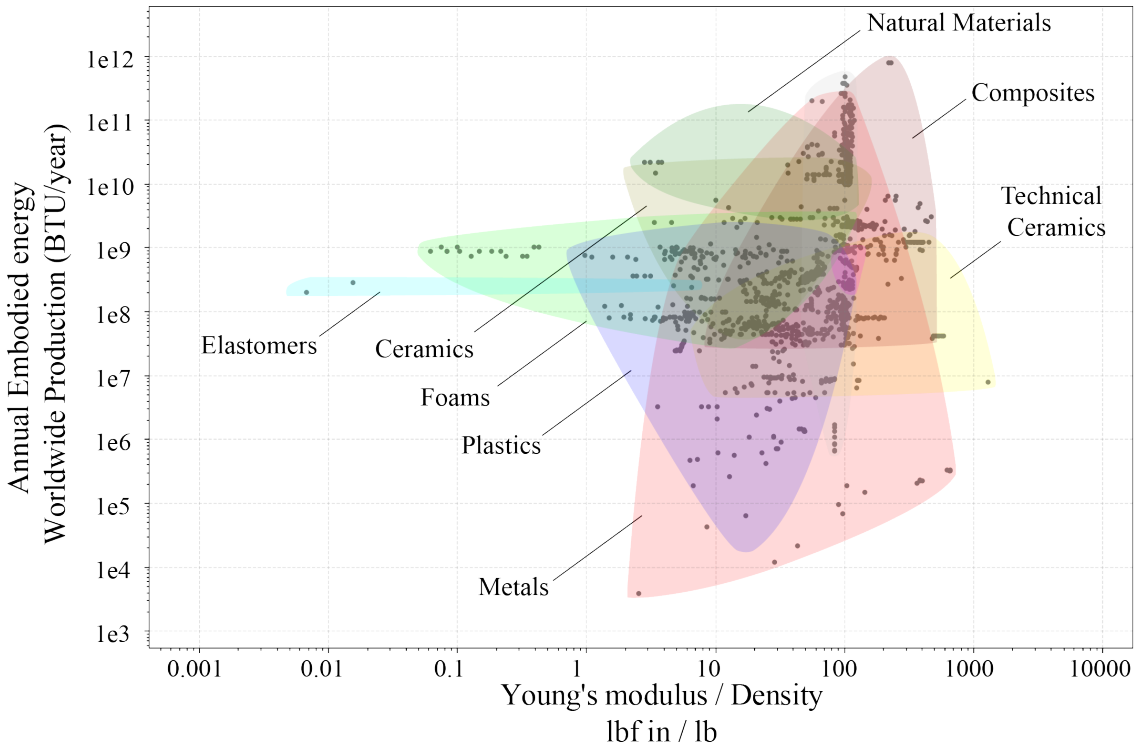

Figure 2-3: Mechanical Properties and Embodied Energy
This figure shows the correspondence between specific stiffness and embodied energy due to worldwide production. Materials occupying the top right corner of the plot are produced in large quantities because of their structural performance, characterizing primarily metals.

of global material production typically follow two parallel approaches, of reducing material where possible and reusing material rather than drawing from virgin material supply. To that end, additive manufacturing has been cited for decades as a sustainable alternative to materially intensive production processes [2] to produce high performing and materially efficient parts. Steel and concrete are among the materials produced in the billions of tons, followed by aluminum alloys and polymers. While additive manufacturing of concrete and thermoplastics have been developed at scale, the large scale manufacture of metal components remains relatively limited. There are several reasons that have inhibited the adoption of metal additive manufacturing across industry, compared with additive manufacturing of thermoplastic polymers for example. The following section will provide a review of common metal additive techniques, introduce a comparative framework with which to evaluate each technique

and consider problematic characteristics and potential opportunities for research in large scale metal additive manufacturing.

2.1 Metal Additive Techniques

Metal additive techniques can generally be categorized into direct and indirect methods, where the former involves printing by melting metal by laser, beam or another energy source, while the latter typically involves printing with some additional binder material that must be removed in an additional processing step [29]. To attempt to collate the plethora of metal additive techniques being developed, the ASTM ISO categorizes metal additive manufacturing into four classes:

- Material Extrusion
- Binder Jetting
- Powder Bed Fusion
- Direct Energy Deposition

The first two are indirect printing methods, while the later two are direct printing methods. In material extrusion, also termed Fused Filament Fabrication (FFF), the process is similar to conventional thermoplastic printing, in which a filament impregnated with metal particles is used as the feed stock. After a debinding and sintering stage, a dense metallic object is produced. Binder Jetting (BJP) operates in a similar manner to a 2D paper plotter, wherein a print head issues droplets of metal to produce 3D forms [6]. In a similar fashion to FFF, this process requires a sintering step to transition from so called green state to fully dense and strengthened part. Powder Bed Fusion (PBF) includes processes like electron beam manufacturing (EBM) or selective laser melting (SLM) both of which use a bed of powder, and a heat source to selectively bond particles of powder together, and layer by layer, build a form [16]. Direct Energy Deposition Methods (DED) involve the melting of a wire or powder directly onto a build substrate, as opposed to PBF methods that require a volume of

powder to melt. Examples of this process include welding arc additive manufacturing (WAAM) or laser metal deposition (LMD). Building up successive layers of weld is an historic process, invented at least as early as 1920 [8]. Finally, we consider a form of BJP that is direct, which is a process in its infancy, typically termed Drop on Demand printing (DOD). DOD is similar to freeform casting, wherein molten material is dispensed onto a substrate or into a medium. Contemporary iterations of liquid metal printing of aluminum and steel have been successfully demonstrated by Vader Systems in 2015 [5], and by Moqadam et al. in 2019 [19]. An approach that combines elements of DOD and material extrusion FFF has been demonstrated by Chen et al, where in a process extremely similar thixo-casting of semisolid metals, a molten metal alloy held in a reservoir is squeezed through a nozzle tip with careful control of temperature to maintain a paste-like consistency throughout the nozzle shaft [11]. For each of these approaches, the challenge of jetting droplets of material involves the fabrication of corrosion resistant tooling to handle the molten metal, and of an actuation system that can deliver repeatable droplets. Finally, the choice of environment and substrate affect the subsequent bonding of jetted material. Thus liquid metal printing is a process in its infancy, quite apart from a plethora of commercially available printing techniques. Each of these metal additive techniques are suited to different domains of production, each bearing consequences to scale, resolution, process rate, energy consumption and performance. Hence, we now elaborate a framework against which to compare these processes.

2.2 Comparative Framework for AM

Despite the plethora of literature summarizing the various kinds of metal additive manufacturing, the presentation of an holistic framework upon which to compare different techniques is surprisingly absent. Therefore, a framework that enables comparison among different techniques is presented here. In particular this framework will assess additive manufacturing techniques along a series of vectors: cost, energy, process rate, resolution and performance. While numerous sources provide compre-

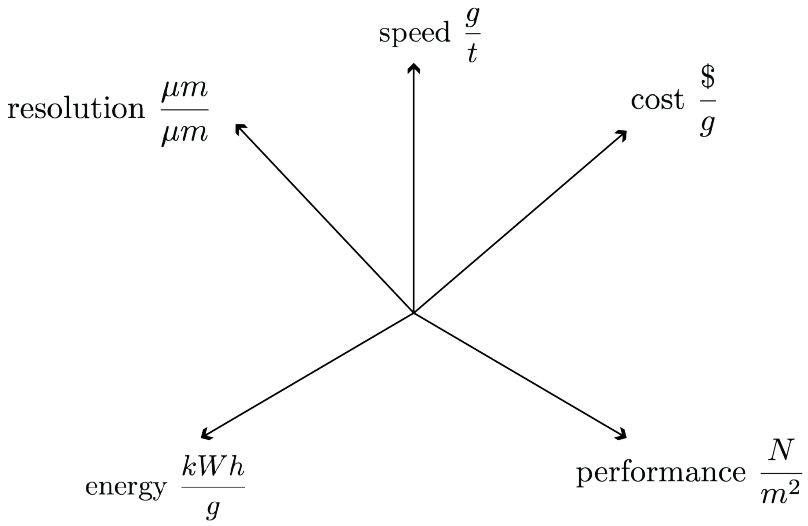

Figure 2-4: Framework

hensive expositions of a rapidly growing field, with new techniques being developed constantly, there does not yet exist a succinct framework for assessing each approach across multiple dimensions. Thus, methods of assessment typically focus on one of these vectors in isolation, for example, resolution or performance as a function of tensile strength, fatigue or porosity, are treated rather than a holistic assessment.

2.2.1 Resolution

Testing the capability of a process is challenging considering the geometric complexities that are possible with additive manufacturing. To that end, the National Institute of Standards and Technology (NIST) has developed a test bench part that includes a series of geometric features to verify dimensional accuracy, parallelism, overhangs, straightness to name a few [36]. However, this test part was intended to evaluate powder bed fusion processes and may not translate well to processes like WAAM for example. Indeed the variety of additive techniques might easily thwart attempts to develop a unified test bench that successfully characterizes the capabilities of each. Instead, consider resolution and scale as parameters that describe complexity. Ab-

solute resolution is often considered the lower bound of precision or repeatability, representing the minimum increment that can be taken along a machine's degrees of freedom [31]. While this definition pertains much more to the design of precision machines, a similar definition is adopted to describe the capability of additive manufacturing techniques, typically as a function of a process parameter like nozzle orifice diameter, or particle size. Here instead, resolution describes a minimum feature size. The proposed framework aims to generalize resolution r further by normalizing by the Euclidean norm of the printable volume, V to produce the normalized resolution r_{norm}.

$$r_{norm} = \frac{r}{|V|_2} \tag{2.1}$$

The result is a unit-less number that indicates not only minimum feature size but also the relative scale of the part. With this metric, an additive process intended to produce small parts with fine features may be compared with a coarser process intended to print much larger parts. Figure 2-5a shows the resolution without consideration of part scale, while figure 2-5b shows normalized resolution plotted against scale. It is interesting to regard the normalized resolution of construction along a similar order of magnitude as electron beam manufacturing. From figure 2-5c, there are certainly two regimes of metal additive manufacturing, one which sacrifices high resolution for scale, the other which ensures micron resolution of small parts.

2.2.2 Process Rate

The process rate of an additive manufacturing technique can include machine warm up, print time, curing or subsequent post processing steps. For example in the case of indirect methods, a sintering or infusion process is required to make functional parts [12]. Additionally the removal of support material, post machining of specific features, or heat treating, may add significant time to the manufacture of a single part. For simplicity, we restrict the definition of process rate to focus on the time rate of material itself, or deposition rate. As noted by Gutowski et al [17], there exists a trade-off in process rate, between small feature size and speed, where significant

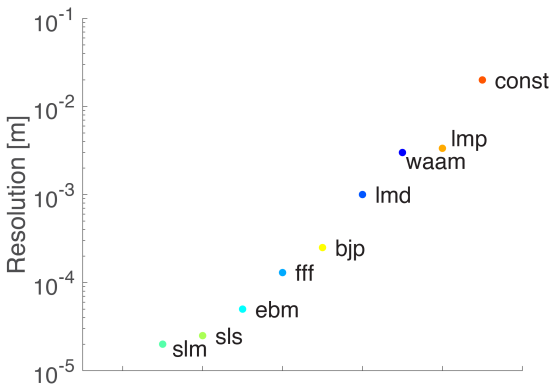

(a) Resolution

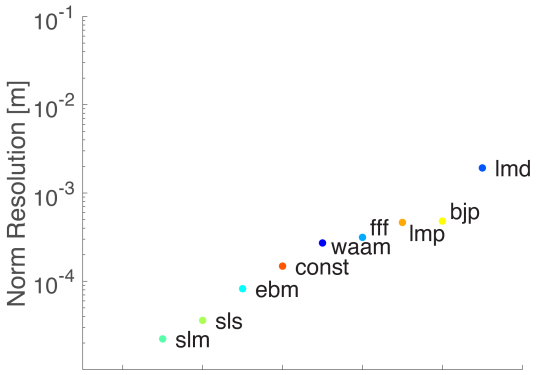

(b) Normalized Resolution

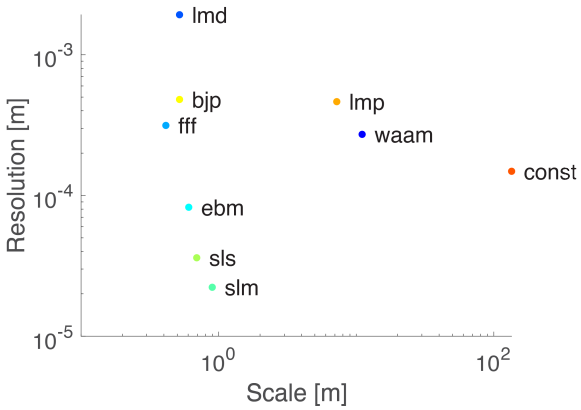

(c) Resolution and Scale

Figure 2-5: Representing Part Complexity
These figures show the correspondence of LMP with WAAM as large scale medium resolution processes

increases in process rate can be achieved by accepting larger coarser features and post processing afterward, citing Big Additive Manufacturing (BAAM) of polymers as a primary example. Alternatively, increasing the power density, build size or number of printing heads can dramatically increase production rate. Consider figure 2-6 which shows process rate for various additive manufacturing techniques. Binder jet printing (BJP) can involve multiple heads jetting material simultaneously, emulating parallel processing typical of conventional manufacturing processes like die casting or injection molding. It is interesting to note the correspondence of direct energy

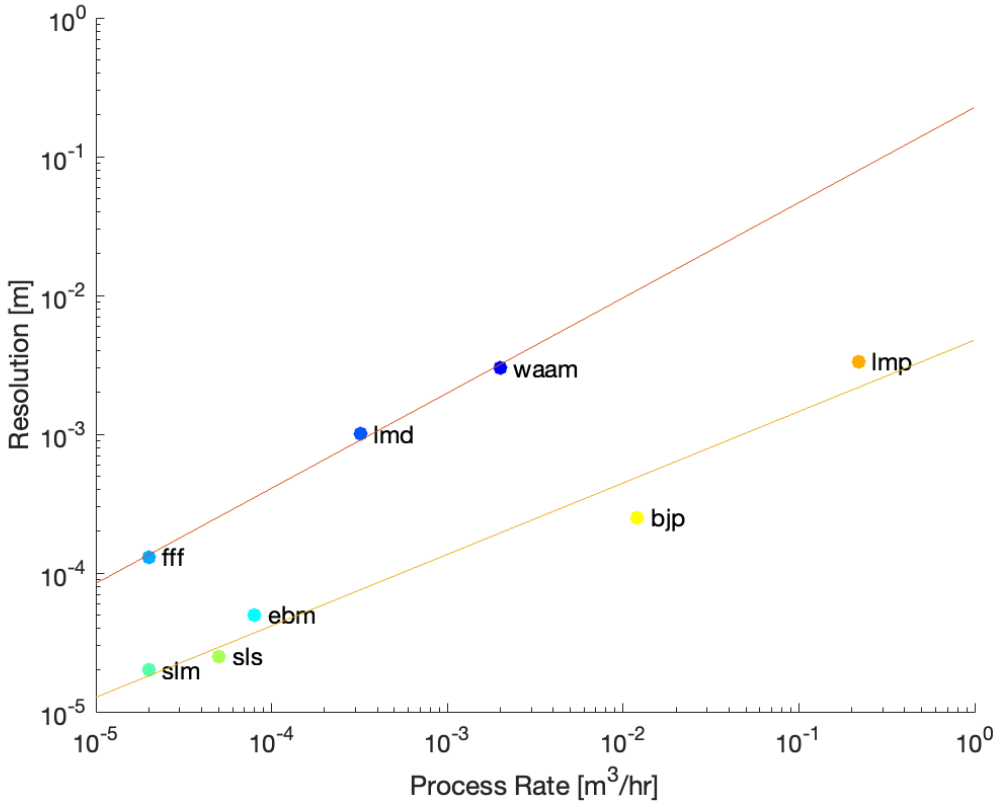

Figure 2-6: Process Rate and Resolution
This figure shows the correspondence of fine resolution printing with slow process rates.

methods and material extrusion along one regime of process and resolution. A similar correspondence can be seen between powder bed fusion methods and binder jetting. Liquid metal printing, which will be discussed in detail later occurs at the scale and speed of conventional casting but the hardware components and process are redolent

of binder jetting, where the feed stock material must be melted before being deposited unlike direct energy methods or powder methods which restrict the melting action to the workpiece itself.

2.2.3 Energy

The consumption of energy per unit mass is typically referred to as the specific energy consumption (SEC) of a process [25]. However as Liu et al. elucidate, the true energy cost associated with a process includes not only the processing energy but also the cost of powering the machine and its subunits. Hence the energy requirements of a manufacturing process include a constant rate associated with machine power and a variable rate associated with material throughput. Depending on the throughput, measured in $\frac{kg}{hr}$, machine energy costs can dominate the distribution of energy required by a manufacturing technique [17]. Figure 2-7, adapted from Gutowski et al, shows the spread of specific energy consumption for conventional metal additive manufacturing. The blue curve shows the energy required to melt aluminum under adiabatic conditions. Traditional manufacturing processes would occupy the rightmost side of the plot, with low energy intensities and typically fast process rates, while high energy intensity processes and low mass ranges, occupy the upper left portion of the plot. In some way, the specific energy consumption can be regarded as a measure of efficiency, by comparing proximity of a process to the melting energy of aluminum under adiabatic conditions. In metal additive manufacturing, the flow of energy into the workpiece and the energy lost to the print bed or substrate, reflected to the environment, or lost due to radiation or convection comprise the basis of energy consumption. Hence processes that involve shielding gas like direct energy methods for example, will suffer from excessive convective losses. Powder bed fusion processes lose heat to the powder bed, especially with high area to volume ratio parts [25]. Additionally, laser melt processes involve a laser absorption variable which is a measure of how much energy is lost during a scan or absorbed by the powder, which depends on process characteristics like material or type of laser [27]. Ultimately there exist three regimes for laser based processes, heating, melting and vaporizing

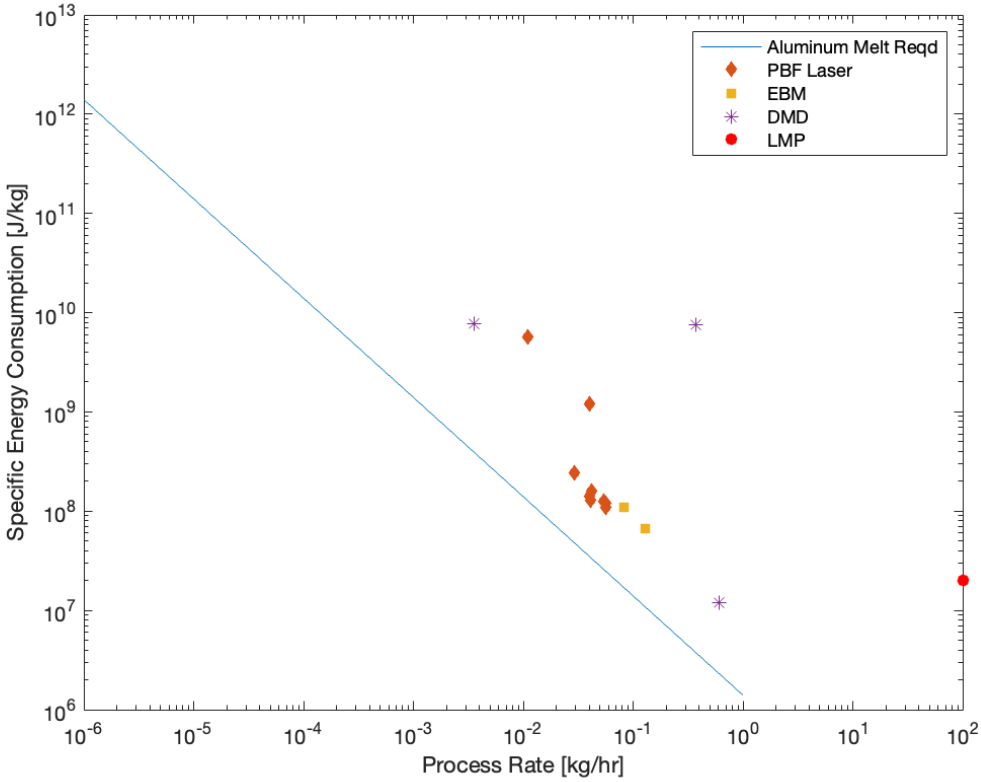

Figure 2-7: Energy Requirements
This figure shows the range of metal additive techniques with high energy intensities due to the low volume of material processed.

[20]. Traversing too fast with low power yields heating, while traversing too slowly with high power leads to vaporizing of the material. Hence the process window for laser based additive techniques involving melting is constrained between heating and vaporizing regimes.

Furthermore, energy density has a profound effect on the resulting micro structure of the part [35], where cell spacing and hence structural properties are inversely proportional to scan speed.

2.2.4 Cost

Manufacturing cost is defined by Ashby as the sum of material cost, capital equipment cost, operational cost, energy, and information [7]. The definition of cost used here will focus on the material, capital equipment and operational costs exclusively.

$$C = \frac{\rho V C_m}{1 - f_{scrap}} + \frac{C_t}{n}\left(Int(\frac{n}{n_t} + 0.51)\right) + \frac{1}{\dot{n}}\left(\frac{C_{eq}}{Lt_{wo}} + \dot{C_{op}}\right) \tag{2.2}$$

Here, C_m involves costs associated with the material of the part as well as auxiliary material, such as in the case of additive manufacturing, support material or shielding gas. C_{eq} involves the cost of machinery which is normally amortized over a write off time, t_{wo}, of 5 years, alongside operational cost C_{op} which includes setup time, overhead and energy. C_t involves the cost of tooling which, for traditional manufacturing may be significant, involving frequent replacement caused by wear such as in machining, or significant initial costs such as in injection molding or die casting. However for additive manufacturing, this term will be neglected.

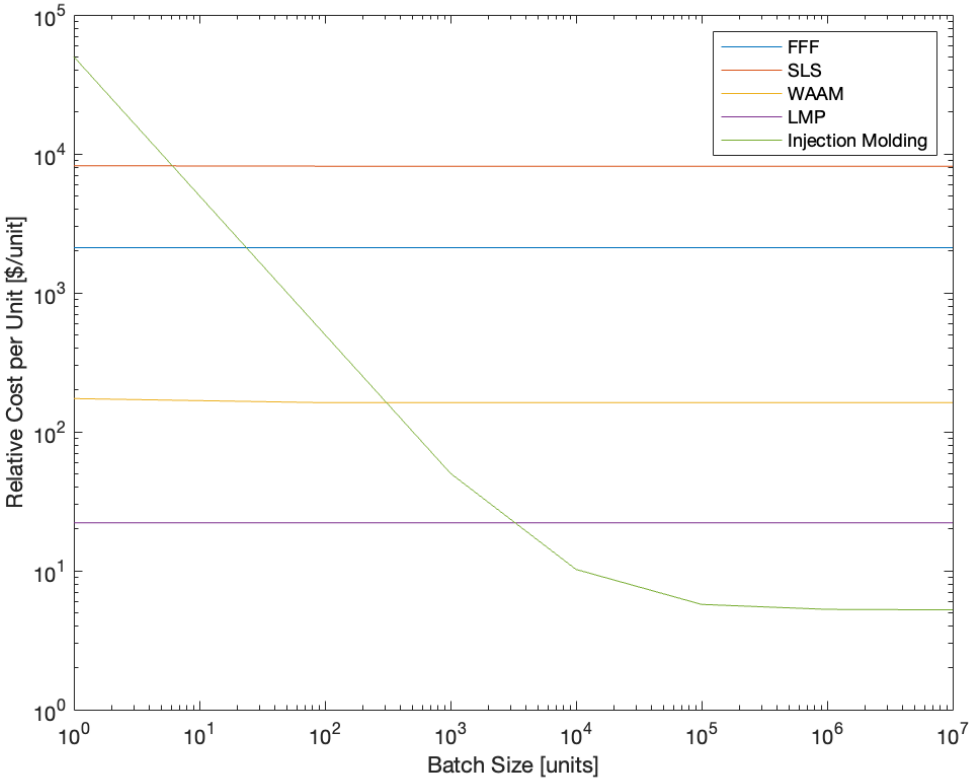

Figure 2-8: Metal Additive Cost Modelling
This figure shows the consistent relative cost per part typical of additive manufacturing compared to traditional manufacturing that can exploit economies of scale. Despite this disadvatage, LMP approaches injection molding in cost.

Table 2.1: Cost Parameters

Manufacturing Technique	C_m	f_{scrap}	C_{eq}	$\dot{n}$	C_{op}	C_t	n_t
Injection Molding	\$1.4	0.1	50000	100	1.6	50000	10000
FFF	\$84	0.1	99500	0.5	3.08	–	–
SLS	\$920	0	250000	0.1	8.2	–	–
EBM	\$920	0	500000	0.1	4.92	–	–
WAAM	\$13	0	500000	1.1	0.63	–	–
LMP	\$0	0.1	15000	100	219	–	–

Costing of additive manufacturing is deeply tied to process rate, in the case of powder bed fusion processes, to scan rate, a reconditioning time, and a lag time which involves machine warm up and part cool down [14]. Furthermore, the economies of scale enjoyed by traditional manufacturing processes that exploit standardization, parallel processing, and the reuse of tooling lead to a reduction of product cost over time. Meanwhile, the cost of additive manufactured parts remains relatively constant [12]. Notwithstanding, the cost of LMP parts comes remarkably close to injection molded parts assuming the cost of material, which is a persistent variable cost for alternative manufacturing remains zero.

2.2.5 Performance

The attraction to metal additive manufacturing is in part the ability to produce complex, high performing parts that would be difficult or impossible to manufacture with traditional methods [28]. Considering figure 2-9, allows us to appreciate the high elastic modulus offered by metals and the span across many orders of magnitude in cost per unit volume. This plot emphasizes the freedom of choice that metal manufacturing offers of mechanically high performing parts. Common areas of application for metal additive parts are thus where the weight saving benefits of a geometrically optimized part justify high costs, such as can be found in the aerospace or automotive industry [16]. Nevertheless, the promise of metal additive manufacturing comes with issues typical of a nascent industry, those related to consistency of performance and part variability as yet unresolved or in the process of being understood [6]. Hence

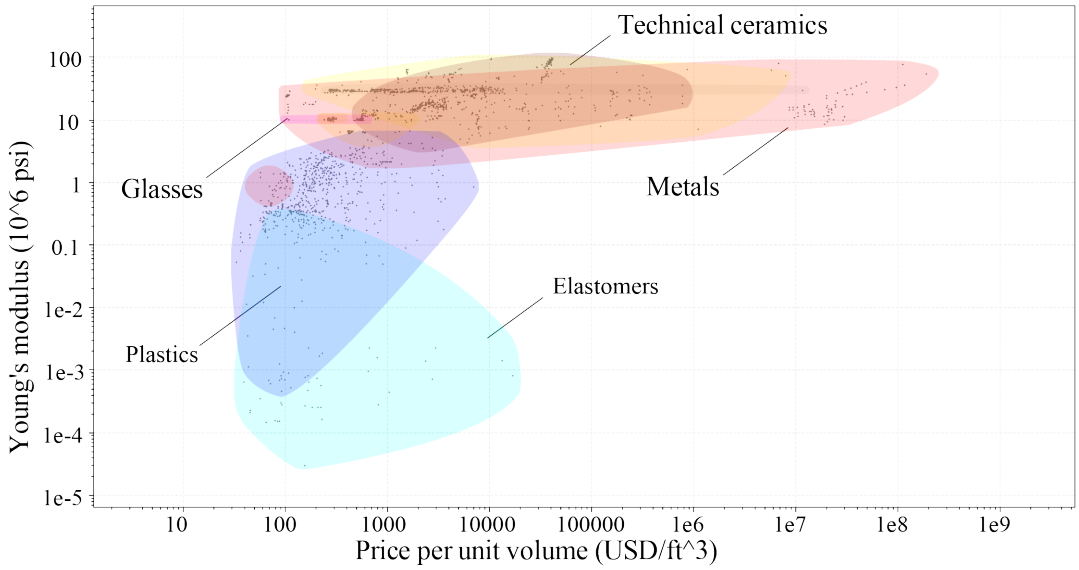

Figure 2-9: Elasticity and Cost
This figure shows the range of additive manufactured material cost, showing metal materials ranking amongst the most expensive.

issues common to metal additive techniques are elaborated here, specifically those related to structural performance.

The performance of additive manufactured parts are typically measured by porosity or surface finish as these characteristics have direct relationships with fatigue strength and ultimate tensile strength. For example porosity and surface finish play crucial roles in the final performance of the part, where surface irregularities and microscopic pores in the material can be sites of cracking and the cause of premature failure. Additionally, reduced plasticity, residual stress, shrinkage and part distortion are common issues that affect metal additive techniques due to complex thermal history involved in printing [6].

In the case of PBF methods, porosity is a direct result of laser scan speed and hence energy density, termed lack of fusion porosity [32]. The bounds of the process window are constrained by excessive energy density leading to vapour entrapment and keyholing, and insufficient energy density which leads to the heating regime instead of the melting regime explained by Ion et al [20]. Ultimately process parameters like hatch spacing, or stepover, layer thickness, scan speed, and beam power affect the

performance of final parts.

The quest for fully dense parts leads to different challenges in BJP, which involves sintering of green parts to reach a final part density roughly around 95%. However the sintering process induces shrinkage, naturally as the reduction of pores at grain boundaries leads to a reduction of volume and hence dimensional inaccuracy [24]. Paradoxically, dimensional accuracy depends on low shrinkage levels which runs contrary to the process of part densification through sintering.

Residual stress is an inherent outcome of the metal additive process, especially in direct methods like PBF and DED. The cycling of heating and cooling leads to cracking, delamination, and distortion [26]. Dimensional inaccuracy can also result from residual stresses produced in direct energy methods like WAAM. This is especially evident in the interface between the build substrate and built up welds. Furthermore, as subsequent material is deposited, a cycle of localized annealing occurs, where residual stresses are relieved and new stresses are induced elsewhere as the tool tip traverses [18].

The performance of additive manufactured parts is the subject of ongoing research, but for a basis of comparison, we shall consider porosity as a key metric in defining the quality of a metal additive manufactured part, primarily due to its role in determining the mechanical properties and indirectly, dimensional accuracy.

2.3 Aluminum and its Applications

We now consider aluminum and its applications in industry, to hypothesize potential spaces of intervention for a metal additive process like LMP. The extraction of aluminum through the Heroult process in the late 19th century coincided fortuitously with the development of the internal combustion engine, mass electrification, and flight. Each of these industries in infancy found value in the density, electrical conductivity, and fracture resistance that aluminum offers. What follows is the proliferation of aluminum in applications as broad as packaging to construction to aerospace [13].

Aluminum is one third the density of steel, easily worked and formed, almost as conductive as copper, resistant to weather, inert to liquids, and has high elasticity. The production of aluminum is extremely energy intensive, consuming roughly 15kWh to produce 1 kg. The recycling of aluminum takes roughly 5% the energy required to produce virgin aluminum. Hence it is considered an 'energy bank' because scrap can be recycled with relatively minimal input [3].

The early uses of aluminum began in the late 19th century with trinkets and novelty items, cast cooking utensils, with more applications following such as surgical equipment, scientific instruments, marine and aeronautical components [33]. The use of Duralumin in World War 1 galvanized a movement to producing alloyed aluminum capable of use in high strength applications. Alcoa developed 17S in response and a raft of heat treatable alloys followed. Further, by World War II, the use of aluminum in planes required vast quantities of material production, such that at its end, wartime surplus of aluminum led to an expansion of application, heralding the ubiquity of aluminum today.

In automotive and aerospace applications, high strength alloy sheet is used in conjunction with extrusions, offering high specific stiffness and fatigue resistance. In construction, facade elements, windows and doors, are framed with extruded profiles, with features to accept glazing and prohibit the travel of moisture, and provide stiffness. The ability of aluminum to be extruded into complex cross sections make it an exceptionally versatile material, eliminating the welding of rolled parts together hence simplifying construction [4]. To that end, its use as structural forms is possible through thinness and the manipulation of figure. Indeed the design of aluminum for a particular application might lead to the design of an extruded profile programmed with specific features.

Furthermore aluminum is cast-able, forged, formed, welded and fastened. The early applications of aluminum are invariably as cast products especially in the automotive industry [9]. Engine components, chassis members, suspension system components like wheel carriers and control arms, increasing elements of a vehicle are produced from high strength cast aluminum. Particularly with casting, the compo-

sition of material becomes the site of design. Optimization of alloying elements in a melt can affect the feeding characteristics of the material entering the mold, cracking, corrosion resistance, and strength and elongation [22].

In mechanical instruments and tooling, aluminum has played an historic roles. Being used as bearings for shafts, housings and covers, impellers and pump lobes, valves, patterns and jigs. The resistance to corrosion, inertness to fluid, light weight and high specific stiffness are favourable characteristics in this domain. Furthermore, aluminum's ability to be machined and formed with excellent surface finish make it ideal for mold tooling. Its fatigue resistance make it a useful material in machinery, from weaving looms to mining equipment [13].

The space of aluminum application is vast, as a consequence of its properties and the wide range of material processes that can give it form. Considering the framework elaborated in the previous section, the vectors of cost, resolution, energy, process rate, and performance suggest the use of LMP as a prototyping tool of medium to large scale components. While the repeatability and normalized resolution of LMP preclude its applicability to small scale and large production volume parts, the rapid ability to iterate by melting and remelting single layer structures, make LMP a potentially valuable design tool in mechanical and industrial design.

2.4 Aluminum Recycle-ability

The savings to energy that come with recycling and the so-called 'energy bank' that characterizes aluminum has been discussed. Additionally, the environmental impact of alumina and aluminum production should be considered. The processing of bauxite to produce alumina results in roughly half the ore discarded as low viscosity clay which must be contained to avoid alkali seepage into ground or fresh water sources, and left to dry out. Furthermore, the emissions of fluoride from aluminum smelting pose serious environmental hazards [4]. Modern environmental authority mandates the absorption of these emissions to acceptable levels however aluminum smelting practices in some parts of the world still do not comply. Hence the motivations for

eschewing virgin material production are manifold. The mechanism by which the secondary metal industry operates and can intervene in production will be considered here. The secondary metal industry refers to the reprocessing of aluminum for reuse as new material. Previously used aluminum parts regardless of forming operation can be recovered as feed stock toward the production of new material. Additional sources of feed stock come from process scrap, for instance the gating systems in castings, or scrap from stamping operations. Even dross skimmed from casting houses in primary aluminum production can be used as feedstock. The recycle-ability of aluminum under certain conditions can be nearly infinite, with material losses ranging from 0.1% to as much as 10% depending on the type of scrap [3]. Scrap segregation is a strategy to ensure maximum recovery of subsequent melts. The remelting and extraction of plastic parts bonded to aluminum parts is undertaken to preserve the quality of the melt. Coated or lacquered material is burned off using pyrolysis. Further separation of alloys into families and heat treatment reduces the melt loss, and can address challenges in the reuse of material for similar or the same product. The recycling of automotive components for example, poses the issue of inconsistent alloying concentration. Typically, aluminum shredded components are primarily cast which contains disproportionately high silicon and iron content. Hence additional alloying elements must be procured in order to retain the composition of the melt or the new material must be relegated to non-critical components [4].

The practice of recycling aluminum is addressed here, describing some essential characteristics of maintaining high metal recovery. For LMP to be an effective metal AM with high metal retention and quality, cleaning and careful selection of the feedstock to produce acceptable alloy concentrations in the melt should be considered. Alternatively, the production of non-structural parts from "downcycled" scrap could yield far more freedom in remelting.

Chapter 3

Liquid Metal Printing

This section describes the Liquid Metal Printing (LMP) process and its relevant components. This metal additive method closely resembles automated casting wherein a volume of metal is melted and poured. Where LMP differs is the absence of a pattern or form. Instead the molten metal is dispensed along a predetermined path, termed a toolpath, that describes a 3 dimensional form. Therein lies the essential advantage of additive manufacturing methods in general, that is myriad forms are possible without patterns or part-specific tooling. The system is gravity driven, such that the pressure head of material in the crucible initiates volume flux at the nozzle tip. To regulate the flow of molten material through the nozzle, a plug rod or stopper rod is used to close and open the orifice of the nozzle and permit or prohibit molten material to flow. Figure 3-1 shows the basic setup, of molten material (A) held in a crucible, which is subject to a significant amount of heat energy, and deposited in a print bed (C) along a toolpath, forming some printed geometry (B).

Figure 3-2 shows the major components of the LMP process. The furnace assembly houses the heating elements and crucible, as well as nozzle assembly (A). The material is deposited into a bed of granular media (B), which itself may be subject to heat. The temperature of the crucible and nozzle tip are precisely controlled with PID temperature controllers (C), ensuring the feed stock is melted sufficiently and does not solidify before exiting the nozzle tip. The work of the thesis follows roughly 2 years of development where initially, a low melting point alloy, pewter, was used as

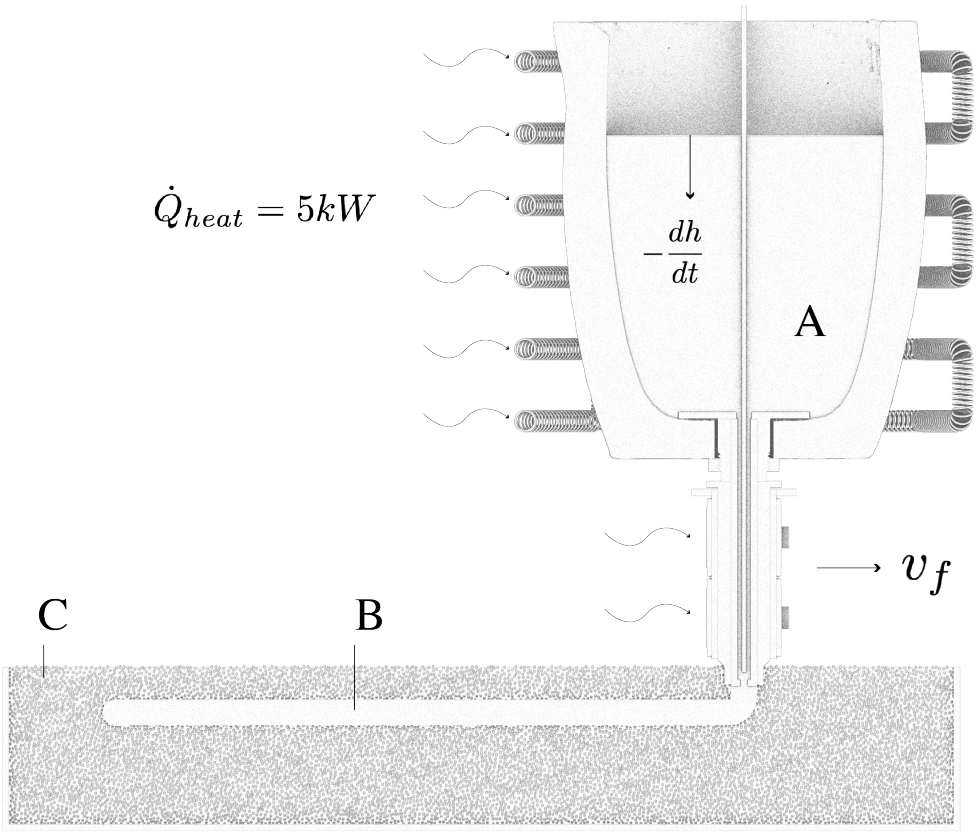

A. Molten Material B. Printed Bead C. Granular Media

Figure 3-1: LMP Process Diagram Schematic

a feed-stock material. In previous iterations, small scale, off-the-shelf components were used to heat pewter to liquid state and eject it to a bed of granular media. The result of these experiments led to larger volume and higher power requirements for the furnace and print bed. The primary goal of this research is to print structurally useful components in aluminum. Hence the current work demonstrates the necessary hardware adjustments and process parameters associated with aluminum printing.

3.0.1 Feed Stock

In previous iterations of the LMP process, a low melting point alloy was used, pewter. The feed stock was primarily of the form of 2" x 3" x 1" ingots. Additionally, recycling of previously printed pewter provided some level of material circularity. However, the

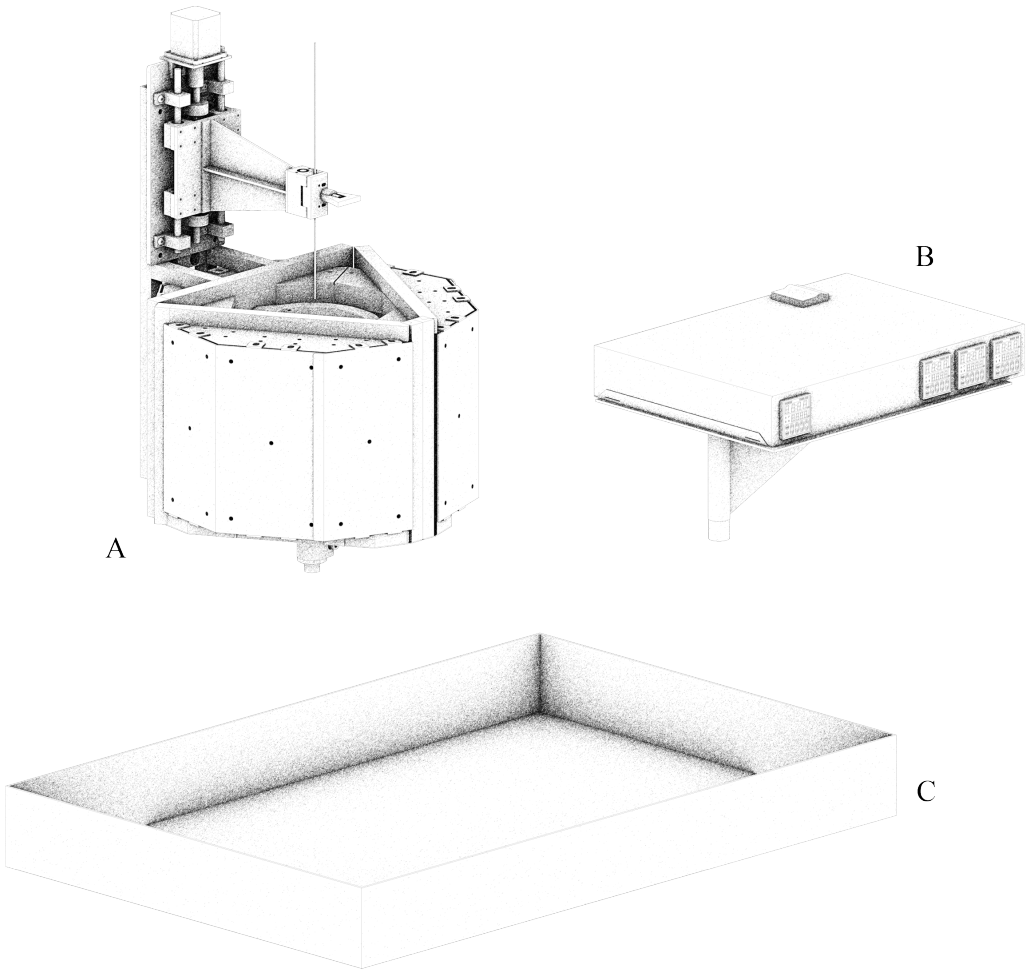

A. Furnace Assembly B. Print Bed C. Temperature Controller

Figure 3-2: System Overview

buildup of slag and impurities after subsequent melts started to affect the quality of printing and lead to irreparable clogging at the nozzle tip. These issues might have been partially resolved with the introduction of inert gas, however the complexity prohibited this strategy from proceeding, especially in building gas-tight containers that would repeatedly be opened to admit new material. The current machine is capable of melting aluminum, hence aluminum scrap has been collected from machine shops across MIT campus. The scrap ranges from plate stock previously machined by waterjet, cutoffs from turning, or short 8020 profile aluminum extrusion. The typically high surface area to volume ratio of scrap make these parts extremely attractive for

melting efficiently. Large prismatic volumes like those of the form of pewter ingots took significantly longer to melt, on the order of hours.

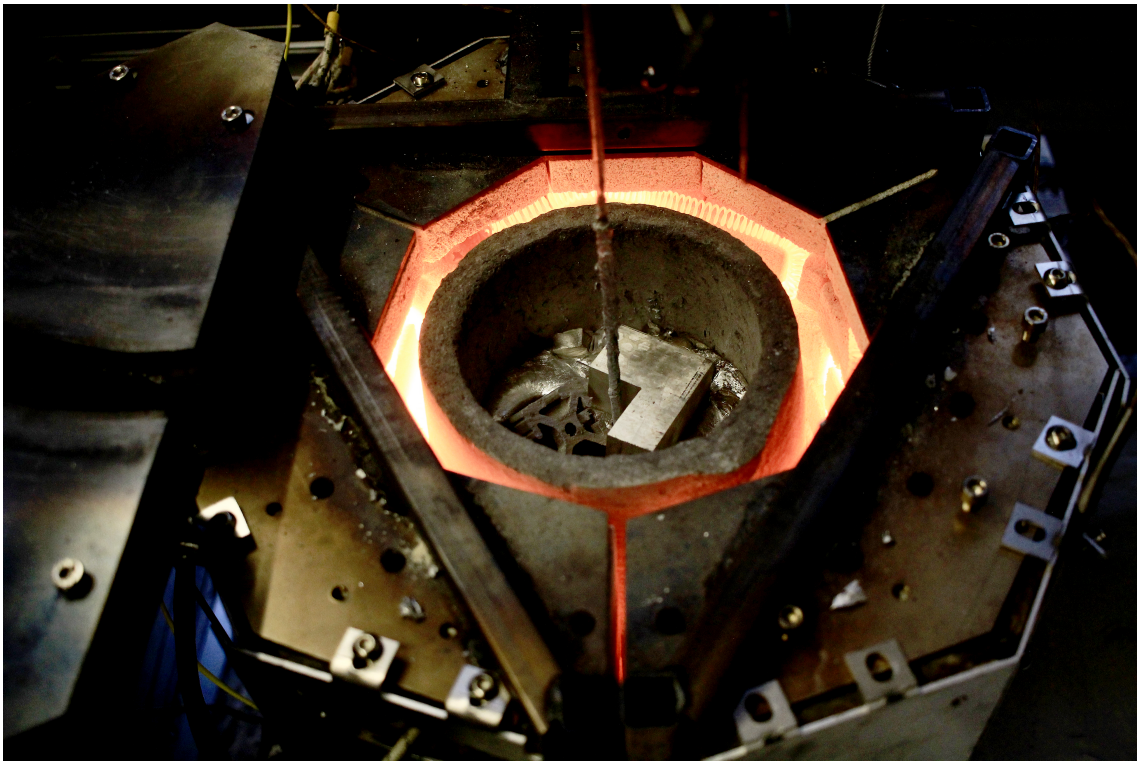

Figure 3-3: Scrap Melting

3.0.2 Furnace Assembly

The source of heat is central to the liquid metal printing process, indeed to any metal additive manufacturing process. The strategy employed in traditional foundry applications ranges from gas, induction, and electrical resistance. At each iteration of the liquid metal process, some form of resistance band heating has been used ranging in maximum set temperature and power. The Garolite Furnace, a repurposed tube furnace intended for thermal experiments requiring high precision, has been used to melt small volumes of aluminum. However, its power input and maximum heat volume were prohibitively modest for the large scale parts that the liquid metal printing process is capable of producing. Hence, a larger furnace is designed to enable faster melting of greater volumes of metal. Nichrome and Kanthal resistance wires

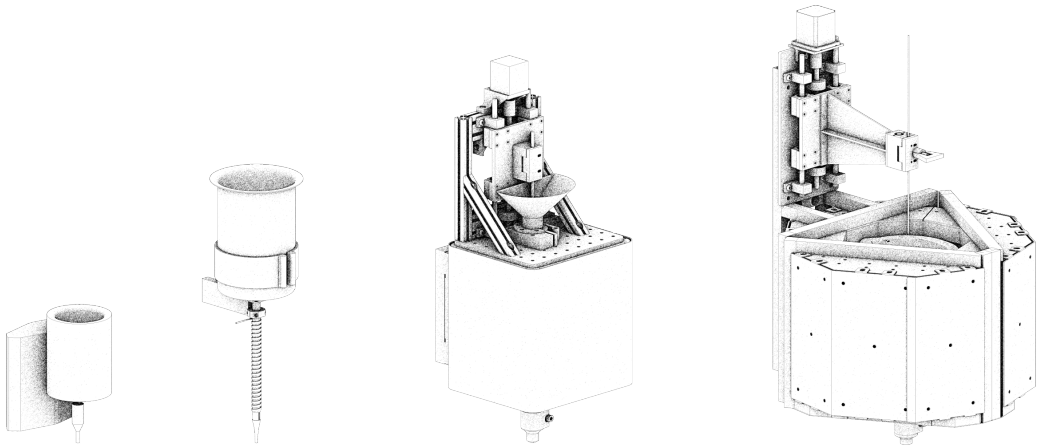

Figure 3-4: Furnace Iterations

Table 3.1: Furnace Development

	A	B	C	D
Power	500W	350W	500W	5kW
Volume	$4.6 \times 10^5 mm^3$	$1.8 \times 10^6 mm^3$	$9.5 \times 10^4 mm^3$	$2.3 \times 10^6 mm^3$
Temperature	$480°C$	$300°C$	$1100°C$	$900°C$

are commonly used resistance heating elements used here wound into helical coils using a lathe. The sizing of the coil is given by considering the maximum power draw available from a 3 phase, 120V AC supply, the space requirements of the furnace assembly, the current carrying capacity of the wire, and its resistance per linear foot.

$$P_{supply} = 120V \times 20A = I^2 R_{coil} = I^2 \times 2\pi r \frac{L}{p} \frac{\Omega}{L_{total}} \tag{3.1}$$

Table 3.2: Furnace Functional Requirements

Power	Temperature	Volume	Weight
5-8kW	900 °C	0.03 m^3	$< 50kg$

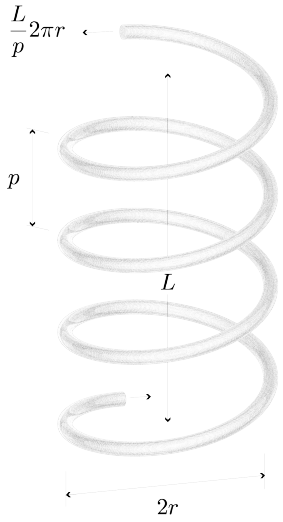

Figure 3-5: Resistance Helical Coil

The gauge of wire used is roughly 1.3mm in diameter, with a current carrying capacity beyond 20A, however with 13.5A, the coil still reaches temperatures above 900 °C. Therefore to avoid tripping circuit breakers along the supply, the current draw was restricted to 13.5A. Hence roughly 6m of resistance wire was coiled about a $\frac{1}{4}$" steel

Table 3.3: Furnace Coil Parameters

Diameter	Radius	Pitch	$\frac{\Omega}{m}$	Current	Required Length
1.3mm	6mm	2.5mm	2.2	13.5A	6.14m

mandral using a lathe. The process is shown in figure 3-6. The coiled nichrome ends are wrapped about a stainless steel $\frac{1}{4} - 20$ bolt which acts as a terminal for connection to power. For a more robust connection, the nichrome is doubled wound at these connections, to ensure additional cross section for current flow and therefore reduced resistance and heat. The firebricks act as supports for the coils to line the furnace, and as insulation. The bricks are produced by BNZ Materials ©, and can withstand furnace temperatures of roughly $1760°C$. The firebricks are soft and can be machined and carved with typical woodworking tools. Dovetail troughs were cut

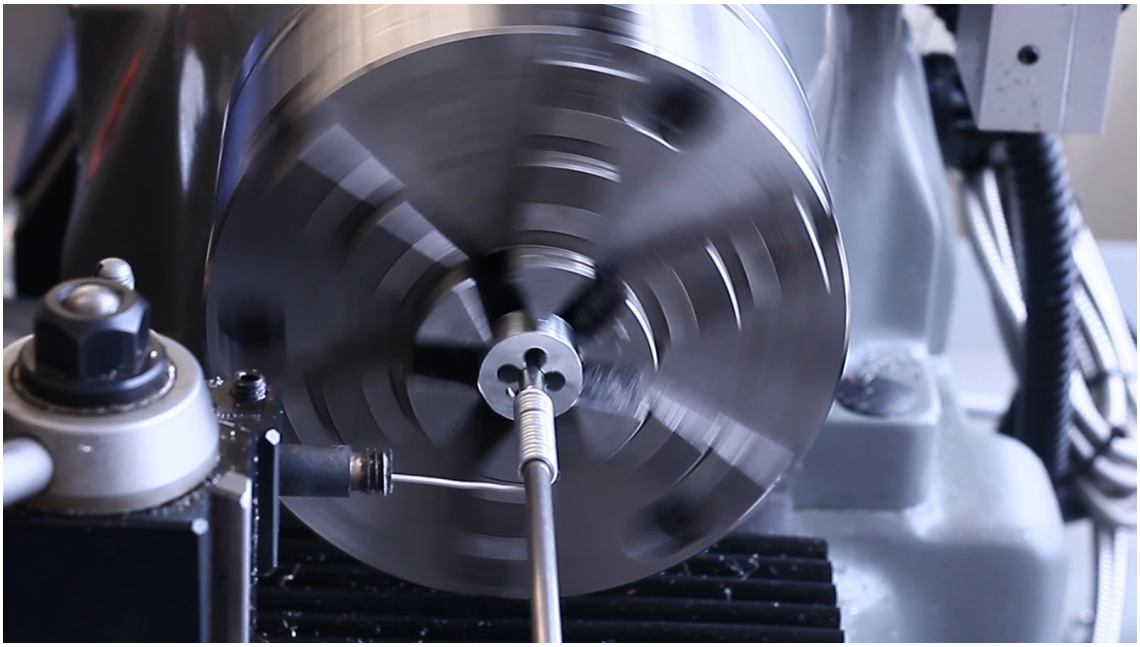

Figure 3-6: Coil Fabrication

using a hand router, and angled cuts were achieved using a bandsaw. The troughs convey coil windings, and the angled cuts enable the bricks to fit the polygonal shape of the furnace. The volume enclosed by the furnace is roughly $7 \times 10^6 mm^3$, and 228mm tall with a radius roughly of 98mm. A rough estimate of melting time can be given by considering the energy required to melt aluminum and the radiant heat transfer provided by the coils. The energy required to melt the metal is given by:

$$Q_{melt} = \rho V(c_p \Delta T + H_f) \tag{3.2}$$

The heat flux into the system provided by the coils is given by:

$$\dot{q_{in}} = \epsilon \sigma A(T_{coil}^4 - T_\infty^4) \tag{3.3}$$

Equating these two equations and solving for time to melt gives:

$$\dot{q_{in}} t_{melt} = Q_{melt} \tag{3.4}$$

$$t_{melt} = \frac{\rho V(c_p(T_{melt} - T_\infty) + H_f)}{\epsilon \sigma A(T_{coil}^4 - T_\infty^4)} \tag{3.5}$$

The resulting time is roughly 52 minutes, assuming adiabatic conditions and absolute efficiency of the nichrome coil in transferring radiation energy to the aluminum. Once the machine is warmed up, this time estimate is accurate, melting nearly the full capacity of a number 10 crucible takes almost an hour. To comply with some soft requirements like easy loading and unloading of crucible and nozzle assembly from the furnace, and based on the size of firebricks and crucibles available, the furnace was designed in the shape of a 9 sided polygon. Each third of the furnace holds three

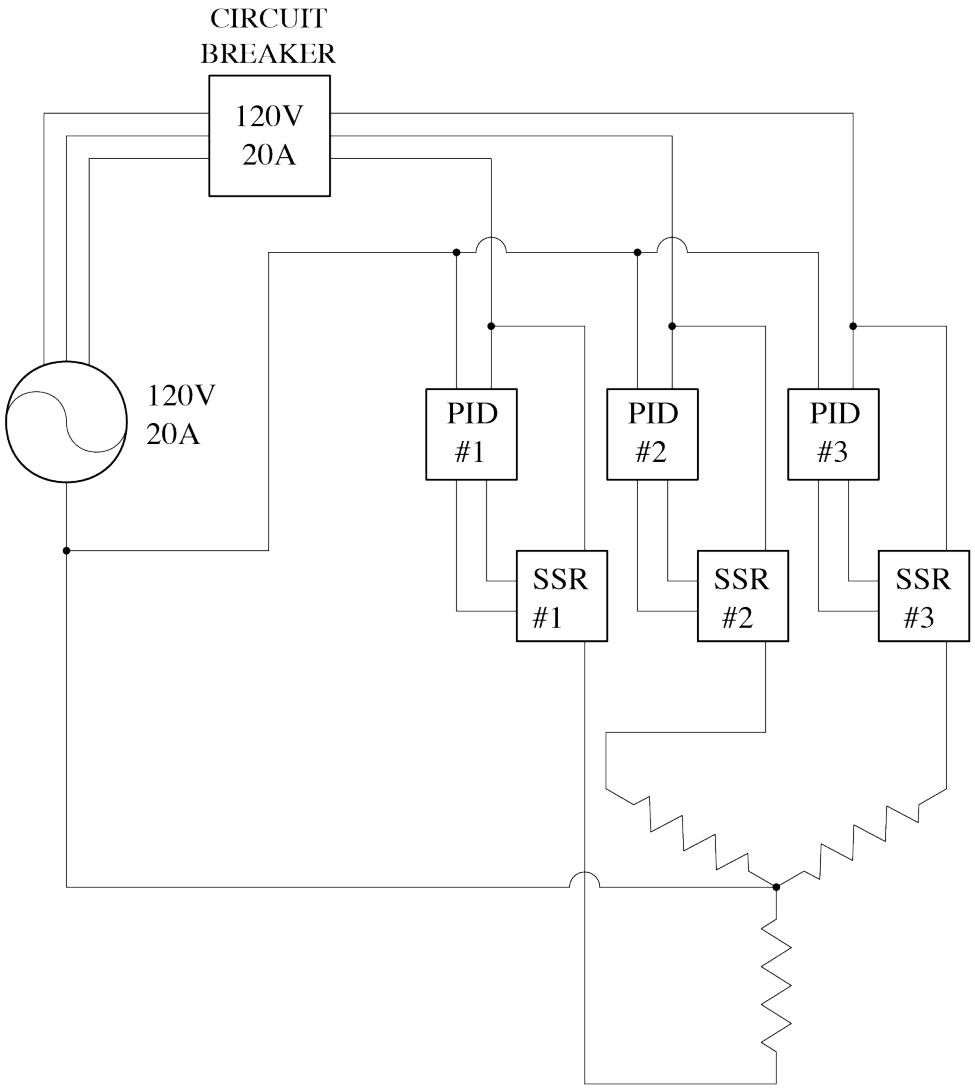

Figure 3-7: Furnace Wiring Schematic

firebricks and one third of the coil overall length, and is serviced by one leg of the three

phase supply. Hence the wiring of the furnace follows a wye scheme, with one neutral connecting all branches. A circuit breaker is included for additional protection. The nozzle assembly is serviced by a separate power supply. Figure 3-7 shows the furnace wiring, and includes with each leg of the supply, a PID controller and solid state relay (SSR) responsible for switching power based on controller signal. Each third of the furnace is therefore independently controlled. Thermocouple probes are places at the bottom of the middle brick, registering temperature at the assembly's cold spot.

3.0.3 Nozzle Assembly

The nozzle assembly is responsible for maintaining high temperatures to convey molten metal from the crucible into the sandbox without freezing and without interfering with the printed bead. This entails a twofold challenge of high power density in a small package. Furthermore, the dispensing of molten metal requires extremely resilient materials due to their highly corrosive nature, especially of molten aluminum. Initially, the nozzle shaft, which is the main conduit for aluminum to travel from the crucible to the print bed, has been stainless steel. However, molten aluminum readily wets to and dissolves stainless steel, especially in thicknesses less than 1/8". Therefore, a ceramic material is chosen, high strength alumina, which does not react to molten aluminum. The nozzle assembly must also connect in a watertight manner to the crucible. As noted earlier, the aggressive surface wetting of aluminum to stainless steel makes it an effective waterproof connector, especially in thicknesses sufficient to resist gradual corrosion from contact with molten aluminum.

Consider figure 3-9 which shows the connection of the nozzle assembly to the crucible. The stainless coupling (B) provides the waterproofing of the crucible and the connection to the ceramic. The alumina tube (C) is held by the coupling (B). Further, the alumina tube also includes the nozzle tip, which is a slight reduction of the inner diameter, termed the orifice diameter or vena contracta. The copper bushing (D) conducts heat from the band heaters (F) to the alumina tube(C). A thermocouple, not shown is sleeved into the copper bushing at the outer surface of the alumina through a small machined slot. The stainless tube (E), connects the

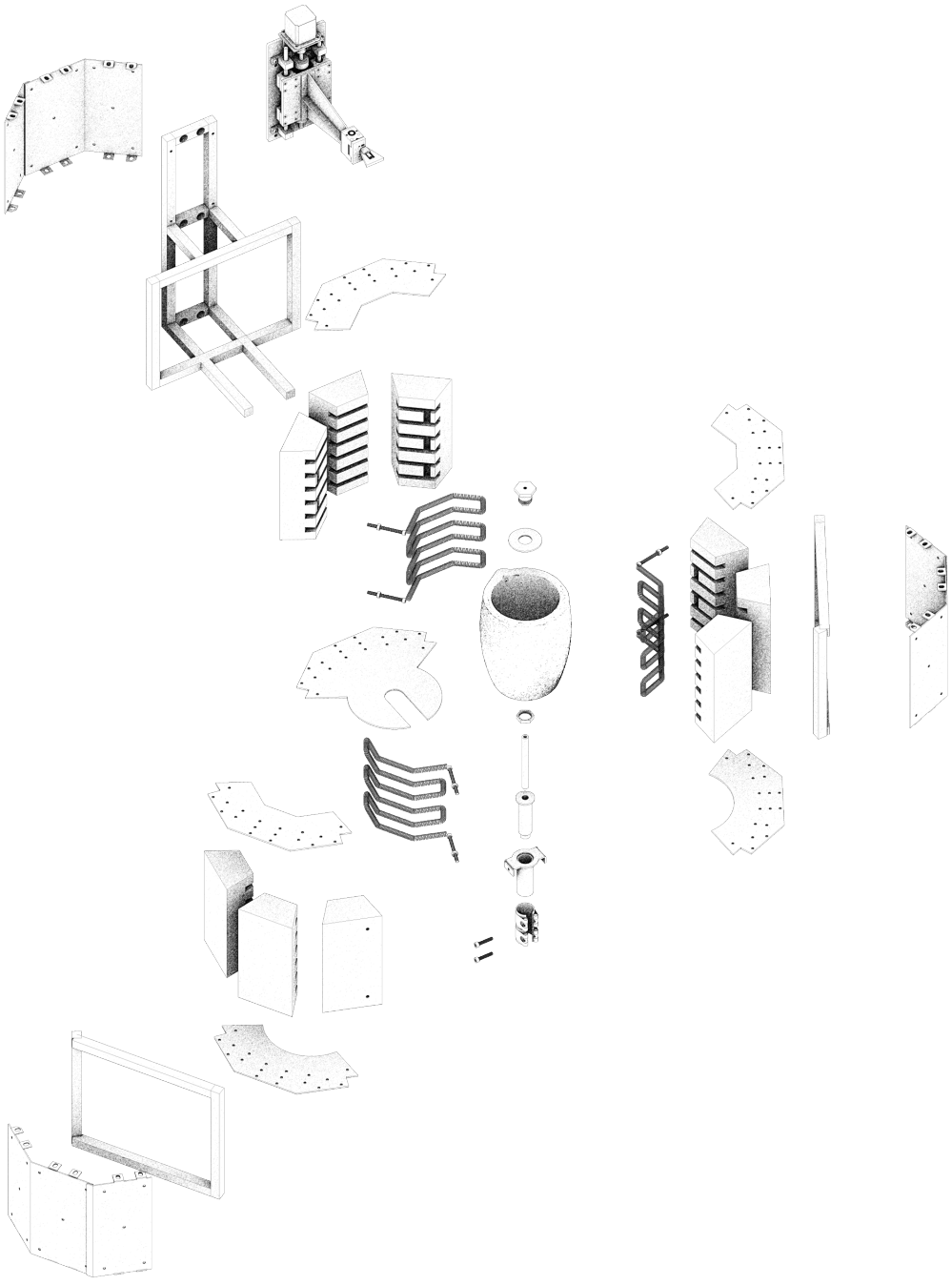

Figure 3-8: Exploded Axonometric Drawing of Furnace Assembly

band heater and copper parts to the furnace frame.

Some parts of the fabrication of the furnace and nozzle assembly are shown in

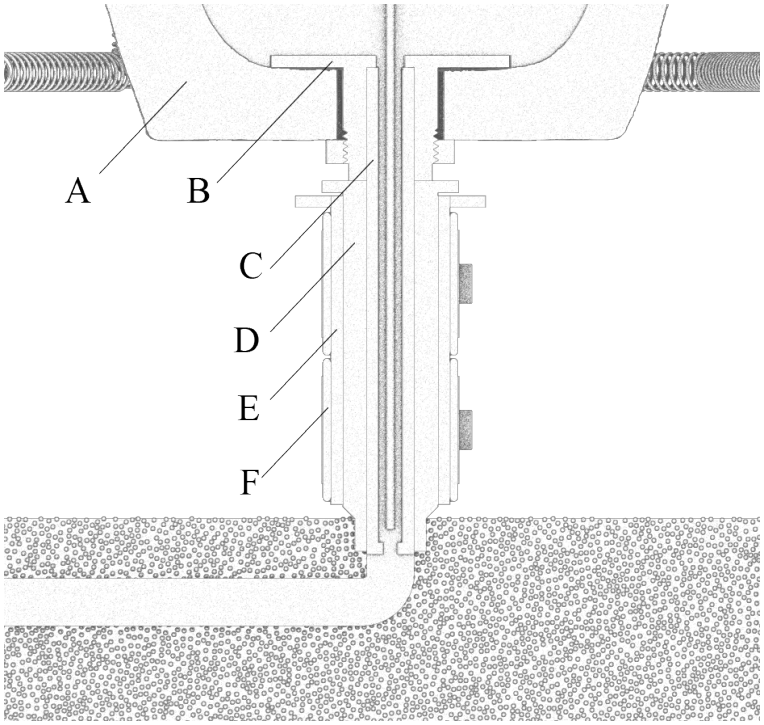

Figure 3-9: Nozzle Section
A. Crucible B. Stainless Coupling C. Alumina Tube D. Copper Bushing E. Stainless Tube F. Band Heater

figure 3-10. The crucible is machined on a lathe, a clearance hole is drilled on center for a stainless steel coupling to fit. The stainless steel coupling shown in figure 3-10b is a 1"-14 threaded shaft which has an interior bore of 0.5" reamed to 0.005" over to accommodate a high strength alumina ceramic shaft shown being installed in figure 3-10c. The fit between the stainless coupling and alumina ceramic is tight, but loosens as the furnace heats, so a set screw in the stainless coupling ensures the ceramic stays tight to the interior bore of the stainless. This assembly is sleeved into the furnace and band heater assembly shown in figure 3-10d. Finally the furnace is turned on, the coils begin to radiate heat, and the furnace is closed, shown in figures 3-10e and 3-10f.

3.0.4 Print Bed

The print bed is similary the subject of a series of iterations. Previous versions of the print bed have ranged from a plywood box, to stainless steel food-safe containers, to

(a) Crucible Machining

(b) Stainless Steel Coupling

(c) Alumina Nozzle Shaft

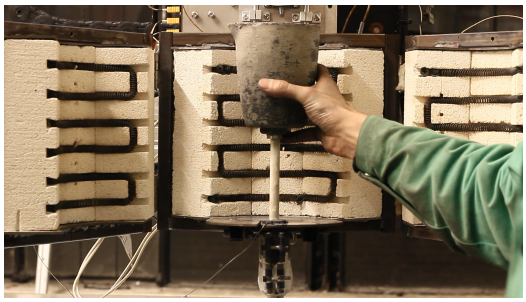

(d) Installing the Nozzle and Crucible

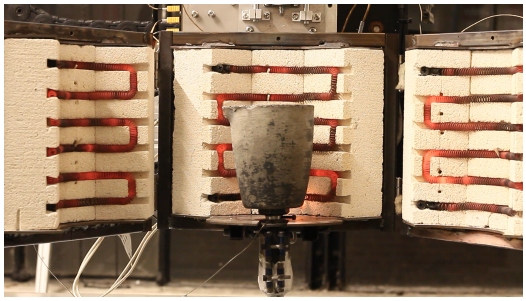

(e) Furnace Heating Up

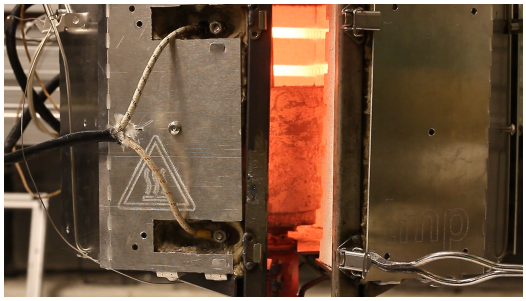

(f) Closing the Furnace

Figure 3-10: Fabrication of the Furnace Assembly

oversized plate steel welded together to form a box. The later two have accommodated the possibility of bed heating, which was an important part of the LMP process when pewter was being used as a feedstock. Invariably, the lower power of the nozzle and crucible assembly for that iteration of the machine were not sufficient to keep the nozzle tip from freezing during a print. Hence, a series of infrared heaters were used to apply power to the print bed and raise the temperature of the enclosed glass bead to roughly $150°C$. However, the size of the bed has never approached the limits of machine travel the Shopbot is capable of. Additionally, the power of the heated bed becomes trivial when printing with aluminum because the current 5kW furnace is sufficient to keep the nozzle from freezing during a print. Nevertheless, the print bed is redesigned with the option of installing a heater assembly. A simple experiment involving a thermocouple at the nozzle tip recording the temperature variation during a print was done to verify if heating the bed would substantially change the outcome of prints. The nozzle temperature was found not to waver regardless of length of printing time. Hence, the new print bed is designed such that heat treating or intentionally slowing the solidification rate of printed beads would be possible. Additionally, the print bed is sized to exploit the maximum travel in X and Y of the machine. Finally, the depth of the print bed considers the limited print depth the current machine is capable of, roughly 90mm maximum depth. To determine a possible range of temperatures that would make a significant impact to the printing of aluminum, the maximum print bed temperature should approach the melting point of aluminum. Chvorinov's rule describing the solidication of molten metal in a sand mold is analogous to the LMP process, where the similar heat transfer scenario occurs. If the sand mold is held at a higher temperature, the cast metal takes much longer to cool. In casting, the grain structure is a direct result of the rate of solidification, where slower rates may lead to grain segregation and larger characteristic cell dimension which in turn affects the yield strength. Hence in general, a slower solidification rate poses detriment to the quality of the finished part, however in the LMP process, this slower solidification may enable bonding over longer distances, despite the instantaneous oxidation of molten aluminum. Solidification of molten metal in

a sand mold is modelled as a 1D heat transfer problem with a semi-infinite mold in Flemings Solidifcation Processing [15]. Here, the thickness solidified S is given by:

$$S = \frac{2}{\sqrt{\pi}} \left(\frac{T_{alum} - T_0}{\rho_{alum} H} \right) \sqrt{\kappa_g \rho_g c_g} \sqrt{t} \tag{3.6}$$

The mold contribution to the formula is given with κ_g, ρ_g, c_g which denote thermal conductivity, density and specific heat of the glass bead respectively. The metal contribution to the formula includes the metal melting temperature T_alum, density rho_{alum} and heat of fusion H. Typically the metal and mold terms are lumped together as a constant C and the equation reduces to Chvorinov's rule which is given by:

$$t = C \left(\frac{V}{A} \right)^n \tag{3.7}$$

Here, S is decomposed as a ratio of volume to surface area, and an empirically found constant n describes the power relationship between solidification time t and the thickness. Typically n is between 1.5 and 2. As a rough estimate of solidification, we assume $n = 2$. For this problem the mold temperature is of interest, so consider C^* instead:

$$C^* = \frac{\sqrt{\pi}}{2} (\rho_{alum} H) \left(\frac{1}{\sqrt{\kappa_g \rho_g c_g}} \right) \tag{3.8}$$

Therefore equation 3.7 reduces to:

$$t = \frac{C^*}{(T_{alum} - T_0)} \left(\frac{V}{A} \right)^n \tag{3.9}$$

A plot showing solidification time as a function of bed temperature shows that time goes asymptotic at melt temperature, i.e. the material does not solidify, as expected. Additionally it shows the quadratic relationship between bed temperature and solidification time. Finally, it shows that at if the print bed reaches temperatures around $400°C$, the a print may be bonded to up to 6 minutes later. There are several simplifying assumptions here that must be noted. This formula is a closed form way to calculate how long the latent heat of fusion escapes a characteristic thickness of material S into a semi-infinite mold. Obviously these conditions are not accurate in

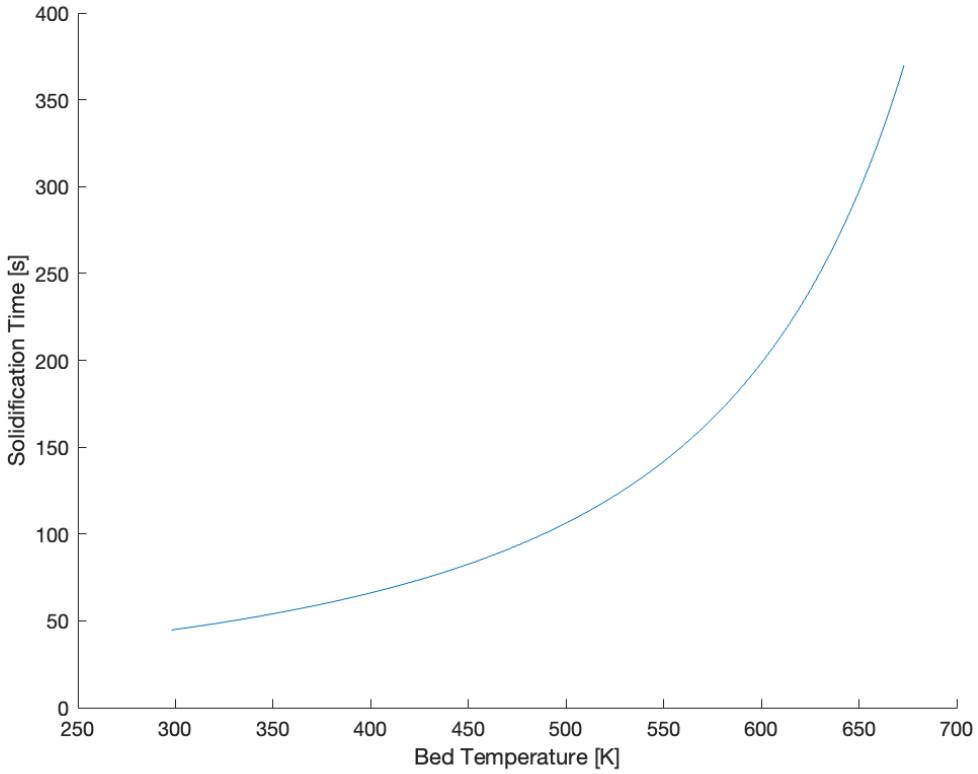

Figure 3-11: Solidification Time
This figure shows an estimate of solidification time based on bed temperature, non-linearly increasing until the bed temperature reaches aluminum melting point.

the current setup and the insulating capability of granular media especially near the surface of the print bed are not applicable. Furthermore, the moment the liquidus temperature is reached, and the heat of fusion starts to leave the print, the material will enter a mushy state wherein the material is neither completely soldified, nor completely liquid. In this case it may not be possible to bond to the solidifying material. While the analysis shown here points toward the potential of bonding over significant time with a heated bed, the simplifications involved may not accurately model the LMP process. The measure of solidification rate and hence bonding potential over time will be the subject of further research. Nevertheless, a revised print bed is designed and fabricated shown in figure 3-12, with the option of integrating a series of heating elements to experiment with the rate of solidification and potential heat treating of freshly printed parts.

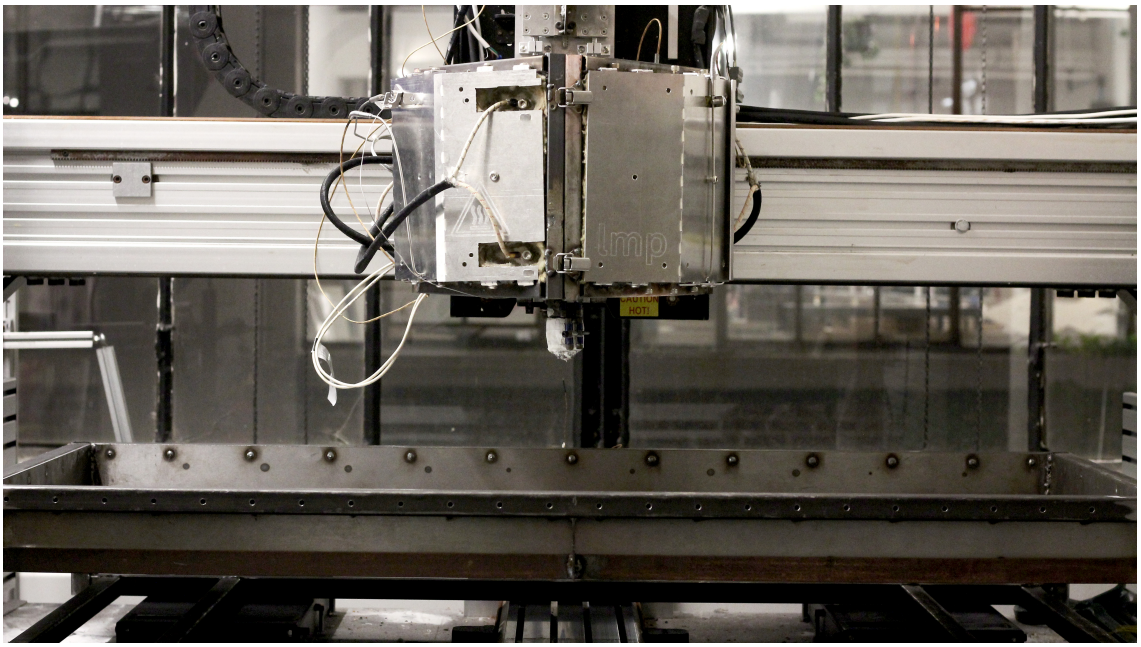

Figure 3-12: Print Bed Fabricated by Kimball Kaiser

Chapter 4

Process Analysis

4.1 Nozzle Thermal Performance

Nozzle performance is extremely sensitive to the thermal behaviour at the tip. At typical operating temperatures, the thermal loss due to radiation must be considered. However, analytical techniques prove intractable when these nonlinear terms are included. Instead, the transient and steady state behaviour across the nozzle assembly can be modelled numerically, using a finite difference scheme in one dimension, with radial symmetry. The system is modelled as a $2 \times N$ grid of nodes, where one column of nodes represents the stream of molten aluminum, the second facilitates leakage through the enclosing nozzle material. Nodes along the stream of aluminum are subject to conduction radially into the enclosing nozzle wall thickness, as well as conduction between neighboring nodes, ie along the stream of molten aluminum. These nodes are modelled by equation 4.1.

$$\frac{dT}{dt} = k_m \frac{\partial^2 T(z)}{\partial z^2} - k_c A \frac{\partial T(z)}{\partial z} \tag{4.1}$$

The nozzle nodes are subject conduction to the aluminum nodes, convective and radiation leakage to the ambient environment. Additionally, either a source equivalent to band heater wattage density, or zero is applied to the nozzle nodes, determined by $\alpha(z)$ which is a discontinuous function assigning source terms. These nodes are mod-

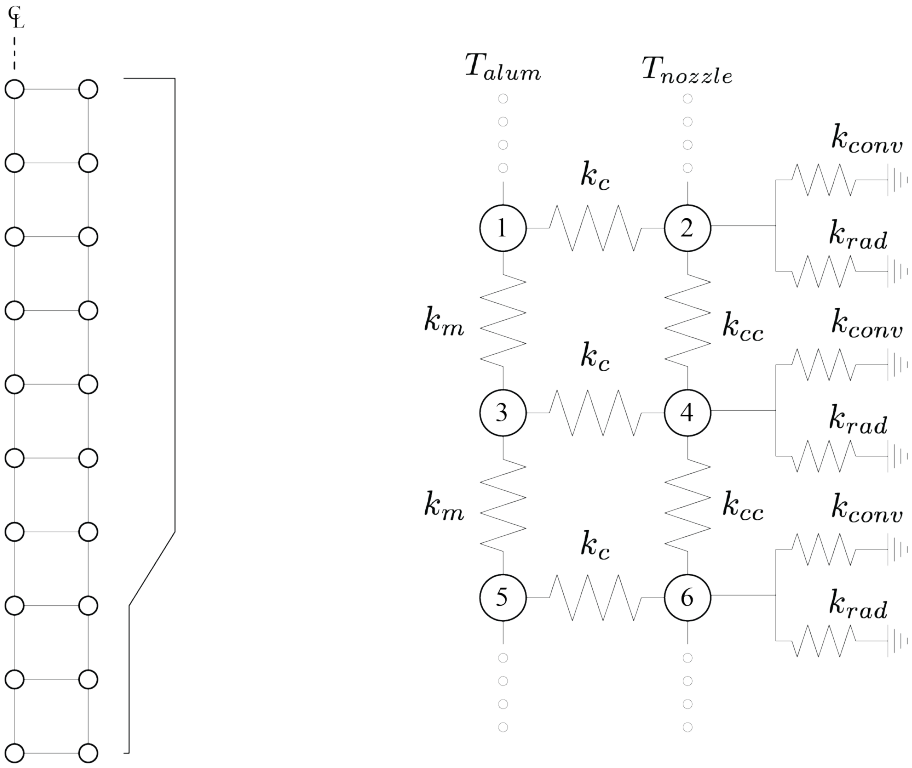

Figure 4-1: Finite Difference Node Schematic
This figure shows the general arrangement of nodes and the connections between aluminum and nozzle nodes with each other and ambient environment.

elled by equation 4.2. The value of $\alpha(z)$ corresponds to part of the nozzle assembly being heated and the portion nearest the nozzle tip being unheated.

$$\frac{dT}{dt} = k_m \frac{\partial^2 T(z)}{\partial z^2} - k_c A \frac{\partial T(z)}{\partial z} - \sigma\epsilon(T_0^4 - T_\infty^4) - \bar{h}(T_0 - T_\infty) + \alpha(z) \tag{4.2}$$

Each aluminum node connected to a leakage node, which communicates heat flow to the environment through unforced convection and radiation. The environment is assumed to hold a consistent ambient temperature T_∞. The discretized formulations of these constitutive equations for each node is given by the following:

$$\frac{dT_{alum}}{dt} = k_m \frac{2T_i - T_{i+2} - T_{i-2}}{\Delta z^2} - k_c A \frac{T_{i+1} - T_i}{\Delta z} \tag{4.3}$$

$$\frac{dT_{nozzle}}{dt} = k_m \frac{2T_i - T_{i+2} - T_{i-2}}{\Delta z^2} - k_c A \frac{T_i - T_{i-1}}{\Delta z} - \sigma\epsilon(T_i^4 - T_\infty^4) - \bar{h}(T_i - T_\infty) \tag{4.4}$$

The discretized formulation is used for transient simulation of the nozzle state 4.6. The matrix $E(T)$ represents the thermal capacitance of the system, each node is assigned a value γ given by:

$$\gamma(T) = \rho \cdot c_p(T) \tag{4.5}$$

To reduce the number of system solves and hence improve computational efficiency, an explicit time integration scheme is used, Forward Euler. To keep the matrix banded, alternate ordering rather than column major ordering is used. To extract the nozzle nodes, a matrix C is used on the state to give the transient temperature response $y(t)$.

$$E(T) \cdot \frac{dT}{dt} = \frac{dT}{dz} + bu(t) \tag{4.6}$$

$$T^{(t+1)} = T^{(t)} + \vec{f}dt \tag{4.7}$$

$$y(t) = C \cdot \vec{T(t)} \tag{4.8}$$

Here, the transient temperature responses for different diameter nozzles are plotted, showing different steady state behaviours. A selection of material parameters are shown. Non-linearity in thermal capacitance or conductivity are ignored. The validation of this numerical scheme will be shown in a subsequent experiment, with an alumina ceramic nozzle.

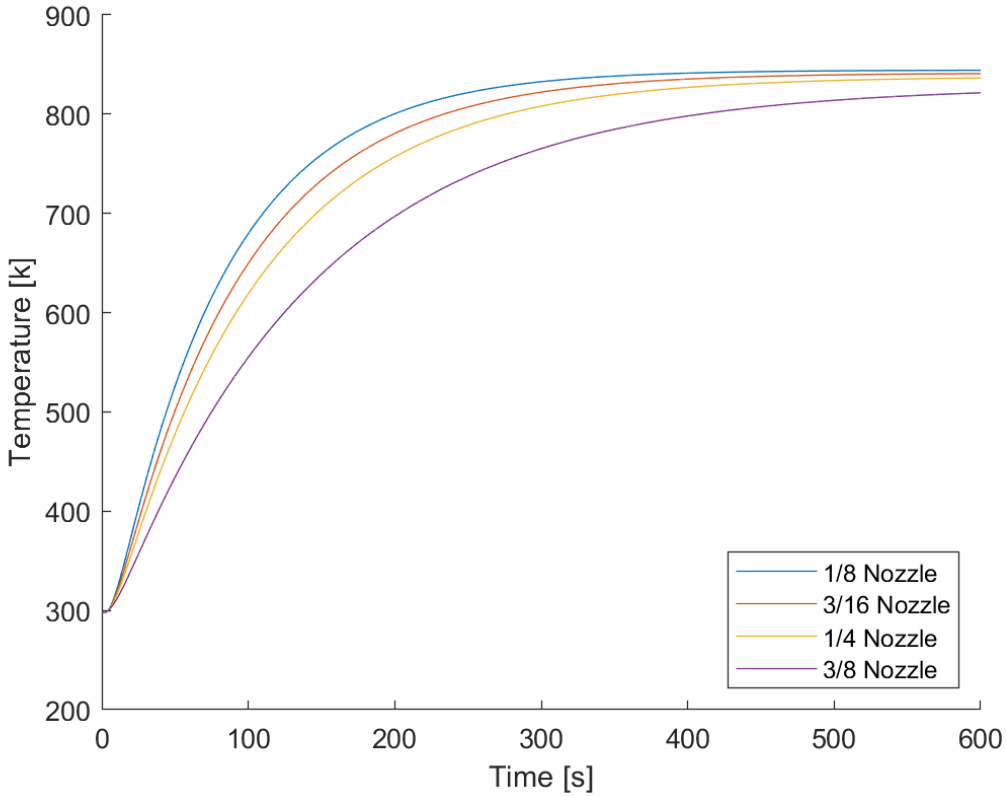

Figure 4-2: Nozzle Temperature Response

dt	1e-3s
Nodes	100
Length	0.15m
Aluminum c_p	903 $\frac{J}{kgK}$
Shaft c_p	500 $\frac{J}{kgK}$
Bushing c_p	385 $\frac{J}{kgK}$
Aluminum ρ	2700 $\frac{kg}{m^3}$
Shaft ρ	7500 $\frac{kg}{m^3}$
Bushing ρ	375 $\frac{J}{kgK}$
Aluminum k_c	120 $\frac{W}{mK}$
Shaft k_c	15 $\frac{W}{mK}$
Bushing k_c	398 $\frac{W}{mK}$
Convection $\bar{h}$	5 $\frac{W}{m^2K}$
Power Density	50 W/m^3
ϵ	0.9
T_∞	298K

Table 4.1: Thermal Simulation Parameters

4.2 Fluid Flow

The liquid metal printing process involves the deposition of molten metal in granular media along a 3D path to describe some form. To that end, several parameters affect the resulting printed part, namely

- feed rate v_f
- nozzle diameter d_n
- volume in the crucible V_c
- print depth h_s
- stopper rod diameter d_s

The flow out of the nozzle is assumed to be laminar, which subsequent experiments will show. Further, because of the small length scales of the geometries in the system, entrance effects are neglected, the flow is fully developed, no rotational velocity is present, and the crucible and print geometries are cylindrical. Beginning with continuity of mass, it follows that the volume flux denoted Q of the crucible, nozzle and printed bead are all conserved.

$$Q_{crucible} = Q_{nozzle} = Q_{bead} \tag{4.9}$$

These volume fluxes can be expanded to include velocity and cross sectional area:

$$v_c A_c = v_n A_n = v_f A_b \tag{4.10}$$

From this point, two divergent methods of analysis follow, one which assumes the flow out of the nozzle is dominated by inertial forces, i.e. that described by Torricelli's law, or dominated by viscous forces which can be derived using Navier-Stokes and continuity equations [34]. Here, both will be presented and compared to the experimental results in the following section. We start by considering the balance of energy head at two points in the system, at point 1, the top surface of molten material in

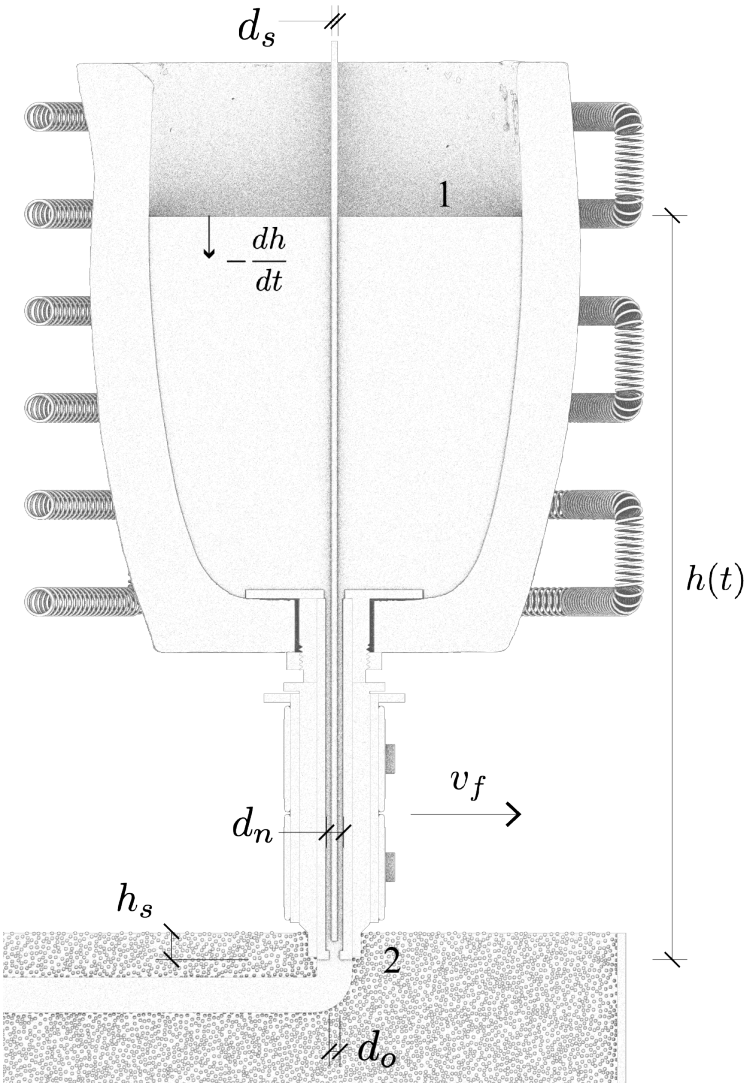

Figure 4-3: Fluid Analysis Schematic

the crucible and point 2,the tip of the nozzle at some depth h_s below the surface of the glass bead, shown in figure 4-3. The energy balance is given by:

$$\Delta H = H_2 - H_1 = H_f + \sum h_m \tag{4.11}$$

Here, H_f refers to the head loss in the form of frictional loss along the pipe length and because the flow is laminar. This term will be augmented to incorporate minor losses h_m in the system, namely the sharp changes in flow geometry, first at the entrance of the nozzle shaft from the crucible and next at the exit of the nozzle tip, the vena

contracta.

Evaluating the head loss gives:

$$H_f + \sum h_m = \frac{v_n^2}{2g}\left(f\frac{L}{d} + \sum K\right) \tag{4.12}$$

For a laminar regime, the Darcy friction factor f is related to the Reynolds number:

$$f = \frac{64}{\mathrm{Re}} = \frac{64\mu}{\rho v_n d} \tag{4.13}$$

$$H_f + \sum h_m = \frac{v_n^2}{2g}\left(\frac{64\mu}{\rho v_n}\frac{L}{d^2} + 0.42(1 - \frac{d_o^2}{d_n^2})\right) \tag{4.14}$$

The energy head difference evaluates to:

$$\Delta H = \frac{v_n^2}{2g} + \frac{P(h_s)}{\rho_{gb} g} - \frac{v_c^2}{2g} - h(t) = \frac{v_n^2}{2g}\left(\frac{64\mu}{\rho v_n}\frac{L}{d^2} + 0.42(1 - \frac{d_o^2}{d_n^2})\right) \tag{4.15}$$

This form can be rewritten using the conservation equation 4.10 noting the equivalence of nozzle and crucible velocity. Furthermore, considering the vertical velocity of the crucible is merely $\dfrac{dh}{dt}$ yields the following nonlinear ordinary differential equation.

$$\left(\frac{A_c}{A_n}\right)^2 \frac{v_c^2}{2g} + \frac{P(h_s)}{\rho_{gb} g} - \frac{v_c^2}{2g} - h(t) = \frac{A_c}{A_n}\frac{v_c}{2g}\left(\frac{64\mu}{\rho}\frac{L}{d^2}\right) + 0.42\left(\frac{A_c}{A_n}\right)^2 \frac{v_c^2}{2g}(1 - \frac{d_o^2}{d_n^2}) \tag{4.16}$$

$$\frac{dh}{dt}^2 \frac{1}{2g}\left(\left(\frac{A_c}{A_n}\right)^2 - 1 - 0.42\left(\frac{A_c}{A_n}\right)^2 (1 - \frac{d_o^2}{d_n^2})\right) - \frac{dh}{dt}\frac{A_c}{A_n}\frac{32\mu}{\rho g}\frac{L}{d^2} + \frac{P(h_s)}{\rho_{gb} g} - h(t) = 0 \tag{4.17}$$

The equation is separable but intractable to work with, so we reduce to a simple quadratic using coefficients a, b, c:

$$a = \left(\frac{A_c}{A_n}\right)^2 - 1 - 0.42\left(\frac{A_c}{A_n}\right)^2 (1 - \frac{d_o^2}{d_n^2}) \qquad b = -\frac{A_c}{A_n}\frac{64\mu}{\rho}\frac{L}{d^2} \qquad c = 2\frac{P(h_s)}{\rho_{gb}} - 2gh(t) \tag{4.18}$$

$$a\frac{dh}{dt}^2 + b\frac{dh}{dt} + c = 0 \tag{4.19}$$

$$\frac{dh}{dt} = \frac{-b \pm \sqrt{b^2 - 4ac}}{2a} \tag{4.20}$$

This result extends the traditional form of the Torricelli theorem which relates outlet velocity to the square root of potential energy head in a reservoir to account for parameters in the system. Furthermore, the quasistatic assumption for crucible or reservoir velocity is unnecessary in this formulation. Additionally the viscous effects of pipe flow are considered in the form of frictional head loss.

While the extended Torricelli theorem is a potentially expressive formulation for the printing process, it is typically used to describe flow conditions dominated by inertial effects, high Reynolds numbers, but not turbulent. The small length scales however, suggest creeping flow, or flow dominated by viscous effects instead of inertia. To characterize these kinds of flows, termed Stokes flows, the Navier Stokes and continuity equations will be used.

For convenience, the cylindrical coordinates of the Navier Stokes equations will be used, written here in expanded vector form:

$$\rho(\frac{\partial v_r}{\partial t} + v_r\frac{\partial v_r}{\partial r} + \frac{v_\theta}{r}\frac{\partial v_r}{\partial \theta} - \frac{u_\theta^2}{r} + v_z\frac{\partial v_r}{\partial z}) = -\frac{\partial P}{\partial r} + \mu\left(\nabla^2 v_r - \frac{v_r}{r^2} - \frac{2}{r^2}\frac{\partial v_\theta}{\partial \theta}\right) + \rho g_r \tag{4.21}$$

$$\rho(\frac{\partial v_\theta}{\partial t} + v_r\frac{\partial v_\theta}{\partial r} + \frac{v_\theta}{r}\frac{\partial v_\theta}{\partial \theta} + v_z\frac{\partial u_\theta}{\partial z} + \frac{v_r v_\theta}{r}) = -\frac{1}{r}\frac{\partial P}{\partial \theta} + \mu\left(\nabla^2 v_\theta - \frac{v_\theta}{r^2} + \frac{2}{r^2}\frac{\partial v_r}{\partial \theta}\right) + \rho g_\theta \tag{4.22}$$

$$\rho(\frac{\partial v_z}{\partial t} + v_r\frac{\partial v_z}{\partial r} + \frac{v_\theta}{r}\frac{\partial v_z}{\partial \theta} + v_z\frac{\partial v_z}{\partial z}) = -\frac{\partial P}{\partial z} + \mu(\nabla^2 v_z) + \rho g_z \tag{4.23}$$

$$\frac{1}{r}\frac{\partial}{\partial r}(r v_r) + \frac{1}{r}\frac{\partial}{\partial \theta}(v_\theta) + \frac{\partial}{\partial z}(v_z) = 0 \tag{4.24}$$

The flow direction occurs solely in the v_z directions, without any angular or radial components. Similarly, gravity is assumed to act only in the z direction. The lateral motion of the nozzle and any inertial effects upon the fluid will be ignored. We will consider the fully developed steady state flow conditions through the nozzle. To that

end there is assumed an additional fluid potential similarly outlined in Lemons et al [23].

After considering the assumptions of the molten material exiting the nozzle, the equations reduce to the following.

$$0 = -\frac{1}{\rho}\frac{\partial P}{\partial z} + \frac{\mu}{r}\frac{\partial}{\partial r}(r\frac{\partial v_z}{\partial r}) + g_z \tag{4.25}$$

$$\frac{\partial v_z}{\partial z} = 0 \tag{4.26}$$

The velocity field along the nozzle depends on radius, not length along the z axis, indicating fully developed flow. Further, we consider no slip boundary conditions along the interface between the molten material and the nozzle ID. Additionally, we include the presence of the stopper rod which changes the flow from a cylindrical column to an annular one. The first left hand side term captures the difference in pressure across the nozzle pipe length L:

$$-\frac{1}{\rho}\frac{\partial P}{\partial z} = -\frac{1}{\rho}\frac{\rho_{gb}gh_{gb} - \rho gh(t)}{L} = \frac{gh}{L} - \frac{P(d)}{\rho L} \tag{4.27}$$

This term combines with the other gravity term to describe the force terms in the z direction related to potential energy head from the material in the crucible, the head of the glass bead and the self weight of the fluid itself.

$$\int\int \frac{r}{\mu}(\frac{\rho_{gb}gh_{gb}}{\rho L} - \frac{gh}{L} - g_z) = \int\int \frac{\partial}{\partial r}(r\frac{\partial v_z}{\partial r}) \tag{4.28}$$

Integrating twice yields the function for the velocity field as a function of radius $v_z(r)$. Two boundary conditions are used to determine constants C_1 and C_2. These are the no slip conditions at the surface of the nozzle inner diameter and the stopper rod outer diameter, namely $v_z = 0$ when $r = R_s, r = R_n$. Let the pressure and gravity terms be lumped into a parameter k:

$$k = \frac{\rho_{gb}gh_{gb}}{\rho L} - \frac{gh}{L} - g_z \tag{4.29}$$

$$v_z(r) = -\frac{r^2}{4\mu}k\left(R_n^2 - r^2 + ln(\frac{R_n}{r})\frac{R_s^2 - R_n^2}{ln(\frac{R_s}{R_n})}\right) \tag{4.30}$$

Finding the volume flux Q_n at the nozzle tip then requires integration of the velocity field over an annular surface between R_n and R_s.

$$Q_n = \int_{R_s}^{R_n} v_z(r) 2\pi r dr \tag{4.31}$$

$$Q_n = \frac{\pi}{8\mu}(\frac{\rho_{gb} g h_{gb}}{\rho L} - \frac{gh}{L} - g_z)\left(R_n^4 - R_s^4 - \frac{R_n^2 - R_s^2}{ln(\frac{R_n}{R_s})}\right) \tag{4.32}$$

The following continuity equation can relate the dependence on height h of the molten material in the crucible to the volume flux at the nozzle.

$$\frac{\pi}{8\mu}(\frac{\rho_{gb} g h_{gb}}{\rho L} - \frac{gh(t)}{L} - g_z)\left(R_n^4 - R_s^4 - \frac{R_n^2 - R_s^2}{ln(\frac{R_n}{R_s})}\right) = -A_c\frac{dh}{dt} \tag{4.33}$$

This separable differential equation reduces to this form, considering a boundary condition at $h(0) = H$ the maximum fluid height at the beginning of a print.

$$h(t) = \frac{L}{g}\left((\frac{Hg}{L} + \frac{\rho_{gb} g h_{gb}}{\rho L} - g_z)^{\frac{L}{g}} e^{-\frac{g}{L}\xi t} - \frac{\rho_{gb} g h_{gb}}{\rho L} - g_z)\right) \tag{4.34}$$

A preliminary comparison of three fluid models are shown in figure 4-4. The Torricelli theorem and a numerically solved augmented Torricelli form are plotted alongside the Navier Stokes solution. The extended Torricelli form captures essential characteristics of the Liquid Metal Printing Process, such as viscous flow through a narrow pipe and deposition into granular media with some pressure as a function of depth, neither of which are present in the simplified Torricelli theorem. The plot shows the deposition of fluid from the crucible levelling off at some non zero value, equivalent to the pressure exerted by the granular media. This captures some intuition about the system as no fluid can leave the nozzle without sufficient potential energy head further upstream.

Modulating the pressure exerted by the glass bead dramatically changes the numerical solution, which captures the reality of some experimental data, as print depth is an extremely sensitive parameter affecting the bead diameter. The viscous flow shows a slow exponential decay which also appears to capture the reality of the printing process. The inertial effects are disregarded, and the flow is entirely dominated by viscous drag.

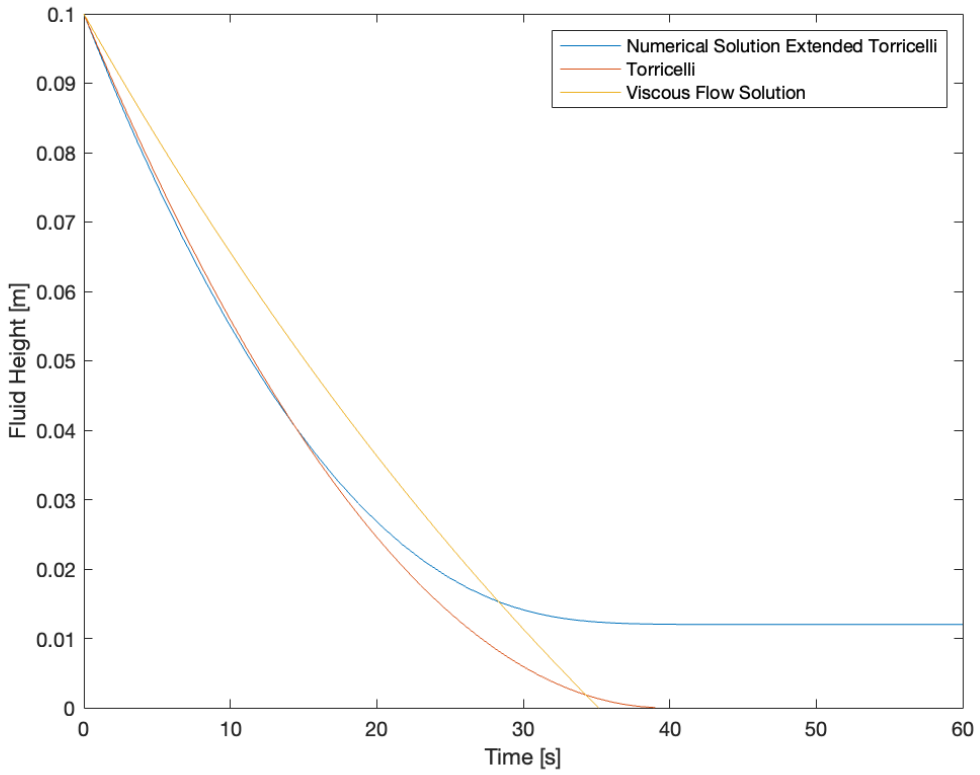

Figure 4-4: Crucible Height
The various flow rates are shown for each solution. The Stokes flow shows a slow flow rate, the numerical Torricelli solution shows a faster flow rate due to the inclusion of an inertial term.

These theoretical models will be revisited in a chapter 5, which will offer comparison with the results of experimental printed specimens.

Chapter 5

Methods

This chapter will describe the experiments used to characterize the LMP process. The machine, described in detail in a previous chapter is used to perform a series of prints. This machine has a positioning system, a mechanism to control material flow, and mechanisms to regulate the build environment. The LMP machine is a modified 5 axis Shopbot Router, where the spindle is replaced by a furnace capable of reaching $900°C$. The current feedstock is aluminum scrap recycled from 3 different machine shops on MIT campus. Material flow is controlled using a plug-rod that moves vertically thereby opening and closing the nozzle orifice. The build environment is a steel framed box filled with 100 micron glass bead which supports the molten material through a print cycle. Ongoing design development around the build environment will lead to the next version of the machine.

There are three kinds of experimentation to undertake, the first involves validation of process physics models, the second involves testing of material properties of the printed specimens, and the third kind involves geometric experimentation to describe formal design rules. Two numerical models have been described, one which characterizes nozzle thermal performance, and the other which characterizes volume flux at the nozzle tip in response to process parameters. These physical models are critical to understanding the consequences of machine design decisions and to build intuition about the role of various process parameters in designing toolpaths. Material characterization is similarly integral, to verify if the LMP process itself has negative

consequences to the quality of the printed part. Part porosity and inclusions too small to be visible upon machining will be investigated directly through standard metallographic inspection. Additionally, tensile testing will compare the quality of an LMP printed specimen against a conventionally cast specimen. Porosity is a challenge that all manufacturers of metal products must overcome, which has profound impacts on the structural performance. Hence by investigating both grain structure and structural performance, we can assess the quality of an LMP part. Finally, a series of geometric experiments that range from simple linear and overlapping toolpaths to more complex shapes are be printed. For larger complex parts, larger vena contracta at the nozzle tip, a smaller diameter stopper rod, minimal print depth, and a large volume crucible are used. As previously derived numerical analysis will show, these parameters will yield larger print diameters, capable of acting structurally. These experiments in summary, will demonstrate the capabilities of the LMP process, and signal its potentials in mechanical and industrial design as well as highlight further areas of research necessary to improve the process.

5.1 Experiments

5.1.1 Nozzle Temperature Response

Maintaining a consistent nozzle temperature is an important requirement in the liquid metal printing process. Therefore the validation of theoretical models to describe nozzle thermal response is undertaken here. The nozzle temperature is measured, subject to energy flux supplied from two 350W bandheaters from Tempco. A standalone testing setup, separate from the machine, was designed and fabricated using aluminum framing and stainless steel brackets. The nozzle assembly includes a high strength alumina ceramic tube, sleeved into a 1" diameter copper bushing, and further sheathed in a stainless steel tube to provide a bolted connection to the stainless steel brackets. A PID controller with a setpoint temperature of 650°C is used, with a dedicated thermocouple measuring the nozzle tip. Simultaneously, another thermocouple,

co-located with the PID thermocouple and connected to a Tinkerforge Thermocouple Bricklet, records nozzle temperature time data which is saved to a computer. These temperatures are recorded each second, with an uncertainty of $\pm 1.5°C$.

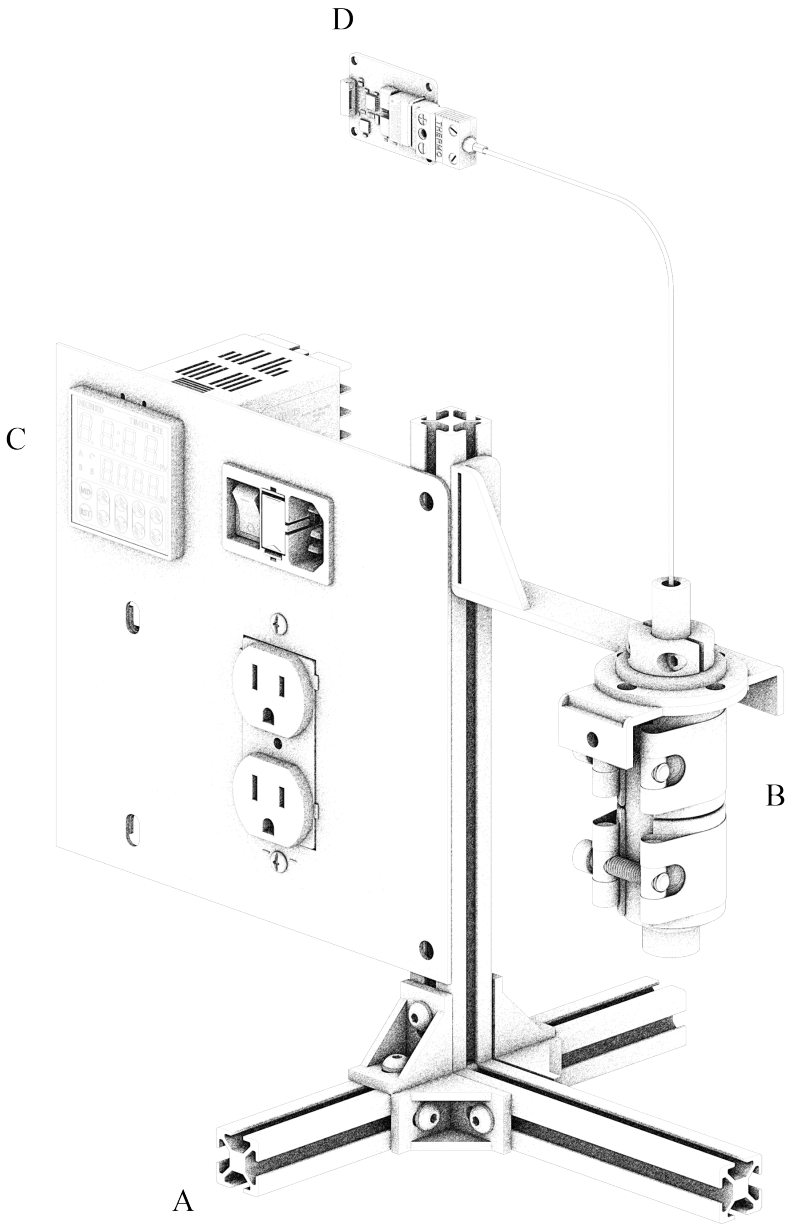

Figure 5-1: Thermal Measurement Setup

The results of the simulation will be validated by measuring the transient response of various nozzle designs at the point of interest, the nozzle tip.

5.1.2 Bead Diameter

A theoretical model to determine bead diameter and hence resolution has been proposed as a function of several variables: print depth, feed rate and parameters related to nozzle geometry. To validate these models, a series of specimens are printed at different depths and feed rates.

Table 5.1: Specimen Parameters

Feed Rate	Depth
35 mm/s	12mm
75 mm/s	25mm
125 mm/s	38mm

The specimens were printed with a number 3 graphite crucible which has a maximum volume capacity $881 \times 10^3 mm^3$, and is filled to roughly three quarters, with approximately $640 \times 10^3 mm^3$ of aluminum for each sample. For large scale geometric experiments, a number 10 graphite crucible with a maximum volume capacity of $2.3 \times 10^6 mm^3$ is used.

An alumina nozzle shaft with an inner diameter of 6.35mm, a stopper rod outer diameter of 4.76mm comprises the nozzle assembly. The alumina shaft includes a vena contracta that reduces the 6.35mm inner diameter to a 3.8mm orifice diameter. The specimens are linear segments 175mm in length. Once printed, the specimens are scanned using a HandySCAN 3D Black from Creaform©with an accuracy of $\pm 0.025mm$. Some critical assumptions are made in subsequent analysis of the specimens. For this analysis, we assume that molten material is deposited as the nozzle traverses in space, and no subsequent material is deposited at a previous point along x, for example no back-filling of material occurs. Further, the velocity ramping profiles

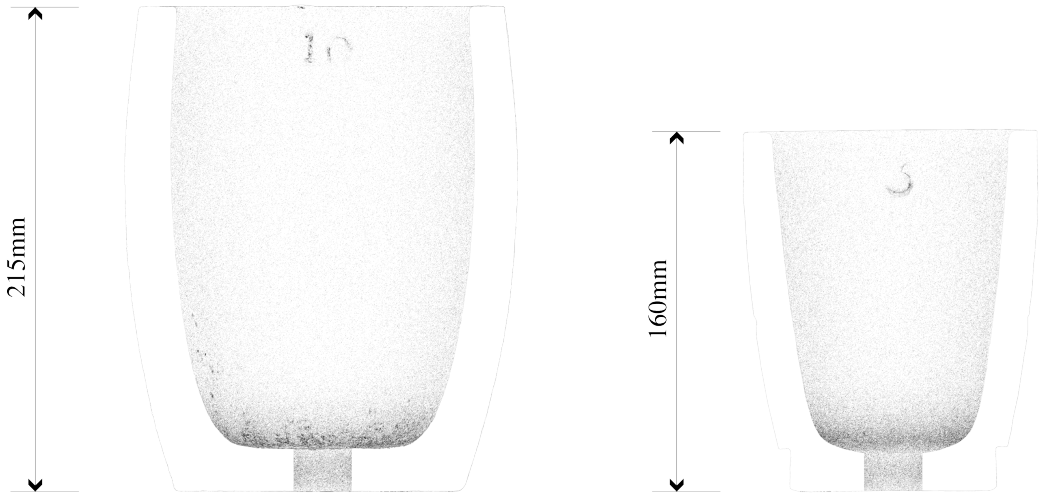

Figure 5-2: Graphite Crucible Cross Section

of the machine positioning system are ignored, the feed rate velocity v_f is constant along the specimen. Finally, the retract portion of each print is ignored in the analysis, thus only the volume printed along the toolpath is considered. The data collected from 3D scanned specimens includes both time and total data.

Table 5.2: Specimen Data

Feed Rate	Depth	V_{total}	Time	X	Y	Area	V_{inc}	V_{disc}

Time data is a series from $t = 0$ to $t_{end} = \frac{175mm}{v_f}$ with an increment of $dt = 0.1s$. At each time step, some material is deposited, and the nozzle moves $\Delta z = v_f \cdot dt$. Here, z refers to the axis along the printed specimen. At each Δz step along the specimen, both X and Y dimensions, a cross sectional area are recorded. Further, the volume of each segment of the specimen of length Δz is recorded as a discrete volume V_{disc}. Finally, at each step, the current V_{disc} is added to previously printed discrete volumes to give cumulative volume data V_{inc}. The last value of $V_{inc} = V_{total}$.

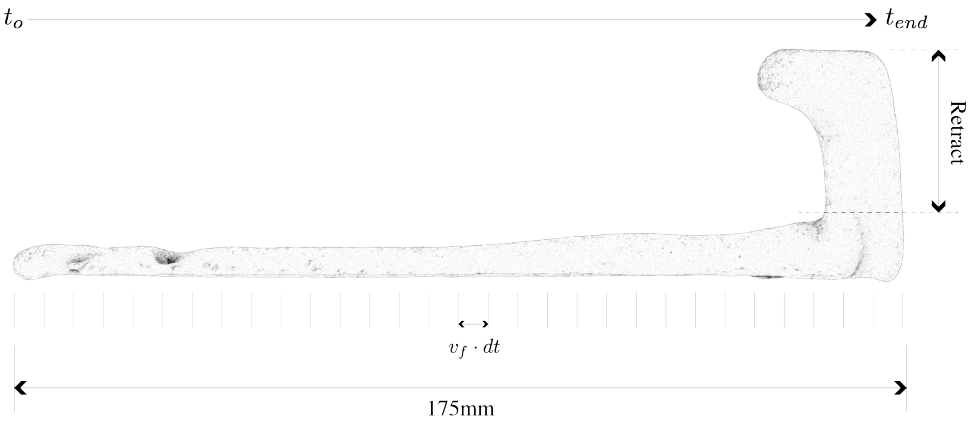

(a) Specimen Metrology

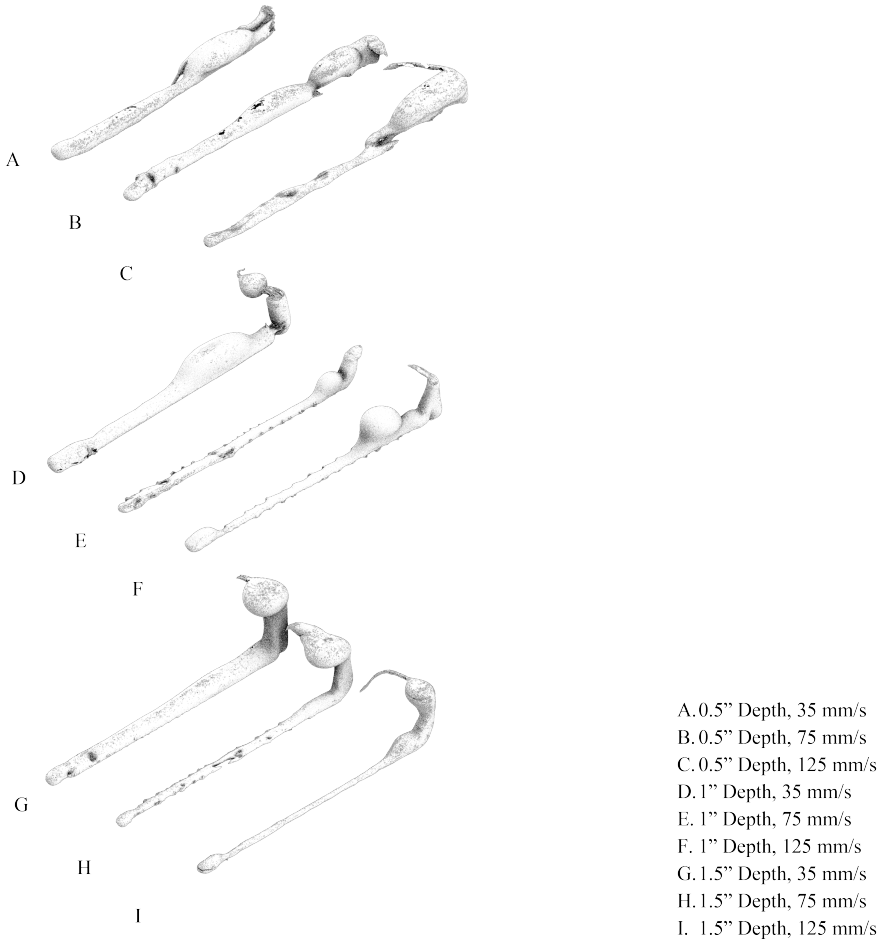

(b) Printed Specimens

(a) shows metrology of the specimens based on sections taken $dt \cdot v_f$ apart.
(b) shows a matrix of experiments across depth and feed rate.

5.1.3 Thermal Imaging

Real-time monitoring of the progress of a print has remained a challenge for this process. While other metal additive manufacturing methods occur at the surface, or are not concealed in any way by the process itself, the monitoring of a print job is in some way trivial. However, the LMP process utilizes a print bed of glass bead which obscures the process. A method for monitoring the progress is hence of extreme value in determining how newly dispensed molten material is interacting with the nozzle tip, and with previously laid material. Thus, thermal imaging is proposed as a solution to partially visualize the flow of molten metal by measuring its radiation at the surface of the glass bead. To this end, a high range thermal imaging camera capable of measuring at least $700°C$ temperatures is required. However as a proof of concept, a low resolution, lower range camera is used, a thermal imaging "bricklet" by Tinkerforge ©. The resolution of the camera is 80x60 pixels, with an accuracy of $\pm 5°C$ and a frame rate of 4.5Hz. The maximum temperature range before saturating is $450°C$. Figure 5-4 shows the basic setup, of a thermal camera (A) mounted in front of the machine and monitoring the progress of a print. The furnace and nozzle assembly (B) and further the nozzle tip not shown, is submerged in the print bed (C) where the printed bead is obscured from view but notionally shown with a dashed arrow.

5.1.4 Hardness and Tensile Strength Tests

Finally, structural testing is undertaken to validate the quality of printed specimens using LMP. Thus a series of printed specimens were prepared alongside identical conventionally cast specimens. Initially, hardness testing was intended to characterize the elasticity of printed specimens, however both cast and printed specimens exhibited excessive plastic deformation beyond what the B Scale of a Rockwell Hardness Tester could measure. A larger diameter ball indenter such as one used with the E scale or H-V scales to characterize soft metals might have been successful. However in the absence of larger diameter indenter, the specimens were testing using a tensile

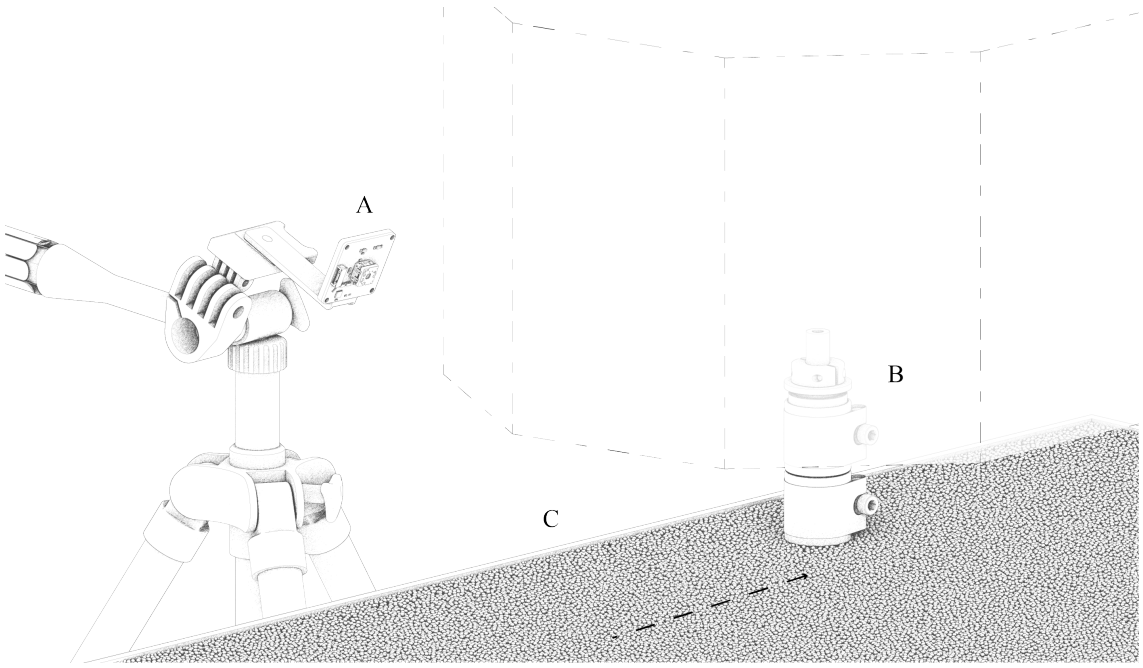

Figure 5-4: Thermal Imaging Setup

testing machine. The printed specimens were machined to conform roughly to an

Figure 5-5: Tensile Specimen

ASTM Standard B557M-15 [1] with a gauge length of 50mm, a thickness of 8mm and a with of 8mm. The specimens were machined from larger diameter print beads, printed at a depth of 15mm with a feed rate of 50mm/s. These specimens served additionally as the pattern for sand casting to produce cast specimens. The cast

(a) Cast Specimen (Top)

(b) Cast Specimen (Side)

Figure 5-6: Cast Tensile Specimens and Gating System

specimens demonstrate the scrap rate involved in conventional casting and eschewed in additive manufacturing. The sand cast specimens require a two part mold, cope and drag, packed with oil sand. The gating system for this cast includes a sprue with a modest pouring basin and a choke, two ingates, at each end of a specimen and a riser to supply additional molten metal as the part cools. Two cast specimens are shown in figure 5-6. The cast specimens show good surface finish considering breaking of the sand pattern at corners of the casting, and no signs of surface defects or shrinkage within the gauge length. A 5/16" through hole is machined on each end of the tensile specimens so that they can be gripped using a steel pin.

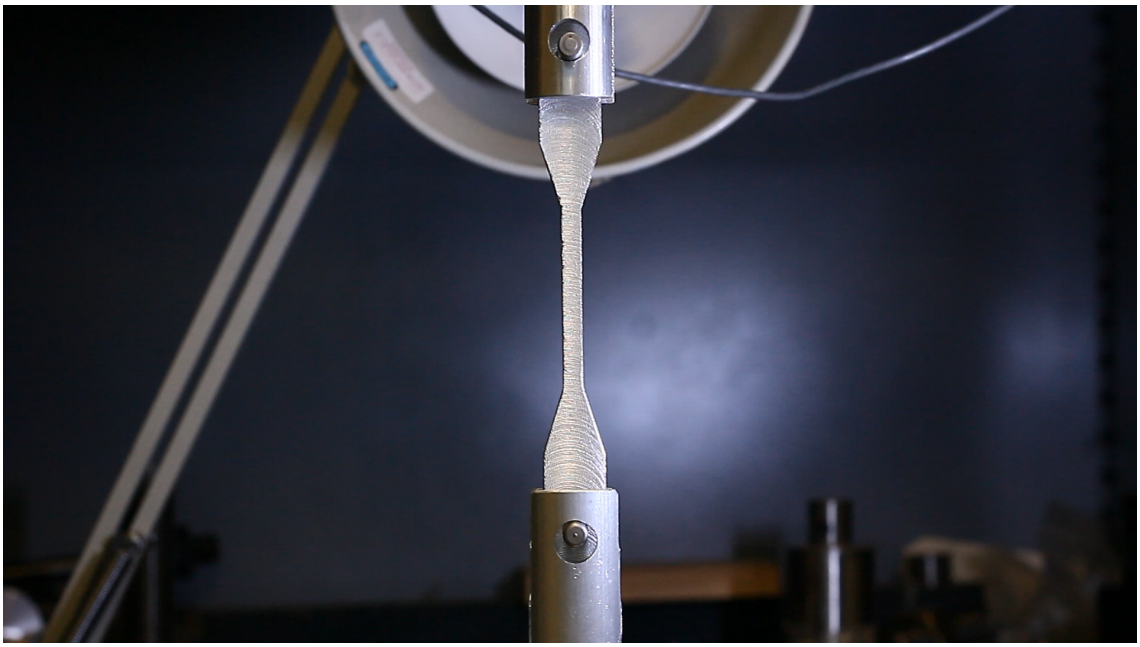

Figure 5-7: Tensile Test

5.1.5 Geometric Experiments

These experiments will serve to establish basic design rules and strategies to achieve particular formal results. Basic forms will be attempted here, that range from single lines to complex forms. For these experiments, a number 10 graphite crucible was used, and filled roughly to 3/4 of its height. Furthermore, each geometric experiment did not exceed $2 \times 10^6 mm^3$ in volume. Simple straight line prints have been

demonstrated with a preceding experiment aimed at characterizing bead diameter, feed rate and print depth. Here, we explore compound shapes and their resulting forms. Figure 5-8 are a series of experiments to understand the process parameters

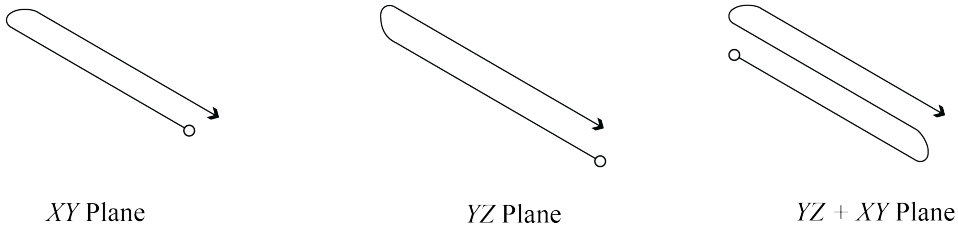

Figure 5-8: Compound Bead

necessary to achieve thicker beads not as a consequence of hardware configuration, rather as a result of toolpath geometry. For each of the figures 5-8 - figure 5-12, the symbol $\circ$ denotes the beginning of the print, and $\rightarrow$ denotes the direction of travel and the endpoint. Here, the relevant parameters are feed rate, depth, and step-over, that is how far away from a previously laid bead will a new bead be printed. The intent is that the stepover is sufficiently far to avoid displacing the previously printed bead and close enough that a bond can occur. The surface based strategies shown in

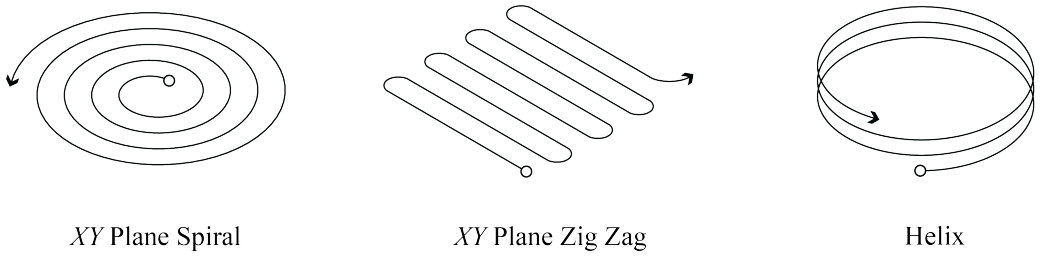

Figure 5-9: Continuous Surfaces

figure 5-9 extend the compound bead logic to describe a surface, spiral or zig zag toolpaths describing in plane surfaces and a helix to describe surface along the Z axis. Pitch and radius are the relevant parameters for describing curved printed forms. With an enlarged print bed and crucible, more complex geometries are attempted. Here a small frame is printed which features a hole, which is achieved by printing a helix at the hole location. Figure 5-11 shows another example of a compound path

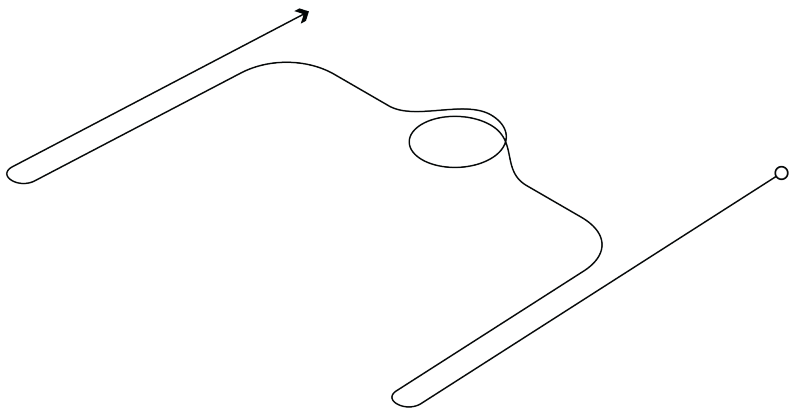

Figure 5-10: Compound Helix and Double Bead Path

experimenting with overlapping beads in the XY plane to describe holes. This part demonstrates an irregular single layer structure that could be machined to precisely fit with other mechanical components in an assembly, for example precision machined surfaces could host threaded connections or bearing seats. Hence the possibility of LMP to be used to print complex blanks extremely quickly and coarsely, but that may be remachined precisely later, is explored here. A full scale prototype is printed of a chair frame, employing the language of design rules explored previously. The chair frame is printed twice, and re-machined selectively to interface with wooden components milled separately. Figure 5-12 shows the toolpath strategy. The frame occupies a footprint of roughly 920mm x 430mm and like the previous experiments is printed obliquely to permit compound bead formation in the XZ and YZ plane. The total Z dimension of the frame obliquely placed in the print bed is 40mm.

As an experiment in producing parts for a mechanical assembly, a desktop CNC frame is printed based on the TinyZ, a machine developed by the author as a solution to remote digital fabrication during the COVID pandemic [21]. The original frame consisted of several aluminum profiles bolted together using t-nuts and brackets. The assembled machine is shown in figure 5-13. The design of the printed frame avoids

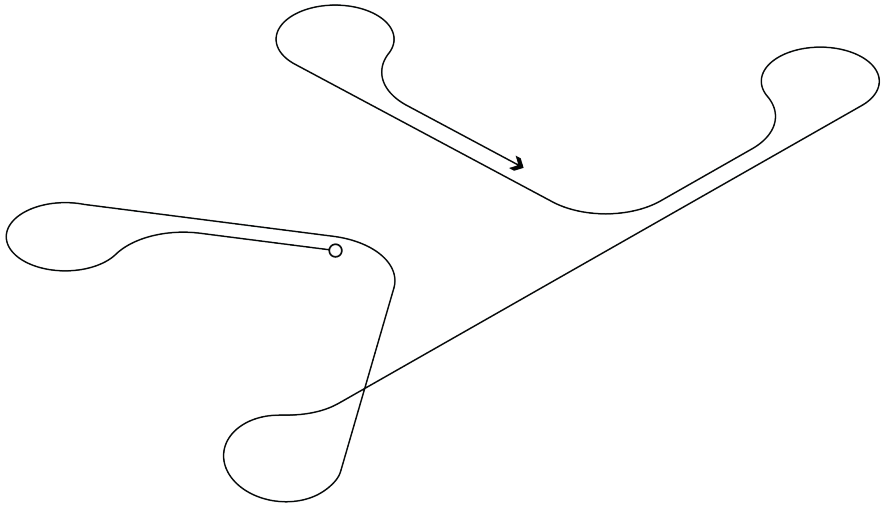

Figure 5-11: Irregular Single Layer Structure

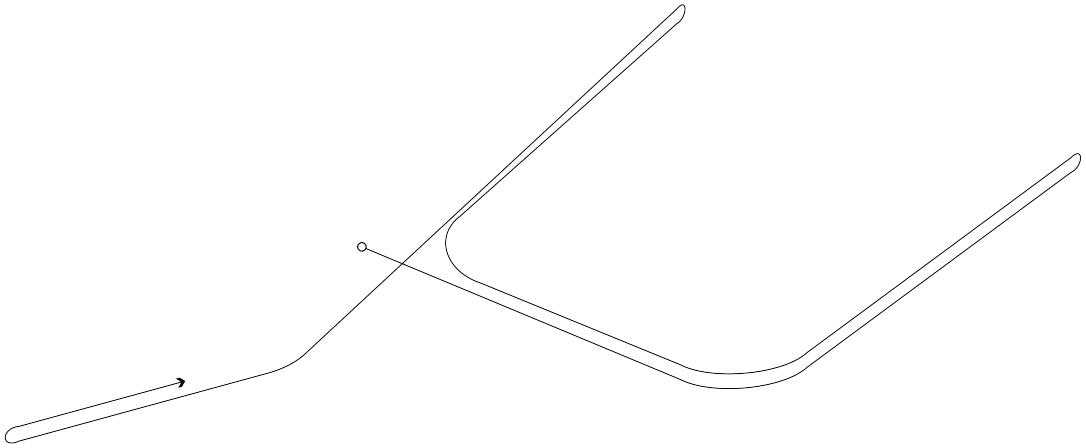

Figure 5-12: Chair Frame

these mechanical connections, instead each component of the TinyZ is printed in multiple layers to produce a monolithic frame. This strategy yields a rough print which can be machined to fit precision ground shafts, lead screws, stepper motor mounting features and bearings. Figure, 5-15 shows three toolpaths corresponding to a base, the x axis, a gantry comprising the y axis, and a smaller carriage that rides on this gantry, the z axis. The toolpaths necessary to print these parts involve spatial printing in the positive and negative Z direction. Overlapping beads are printed in

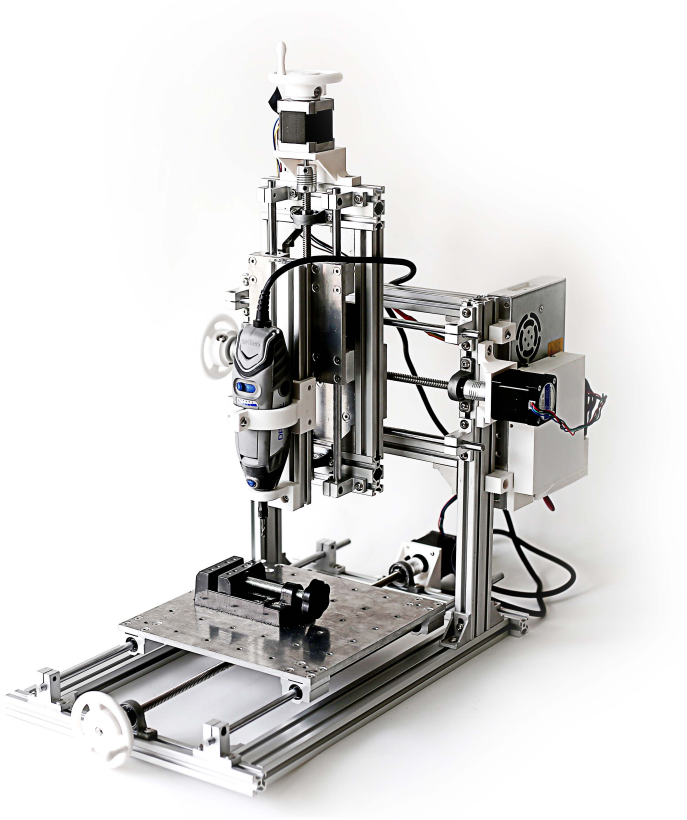

Figure 5-13: TinyZ Desktop CNC Machine

the Z axis to provide additional cross section necessary to house the bearing races, support the precision ground shafts, and act as a mounting plate for the stepper motors. To achieve large cross sections at depth, a new ceramic nozzle is produced with no vena contracta to maximize volume flux. Hence the ceramic nozzle is simply a straight tube, with an inner diameter of 6.35mm. To determine a suitable feedrate, the numerical Torricelli solution is plotted with this nozzle configuration, shown in figure 5-14. The solution shows a maximum bead diameter of roughly 32mm occurring with a print depth of 12mm and a minimum bead diameter of 12mm at 38mm print depths. Based on the geometry of the frame, a 50mm/s feed rate is chosen, providing bead diameters between roughly 18mm and 28mm. As the print depths vary across the print, the printed depths of 12mm and 38mm can be considered boundaries of the process window. Each frame is printed upside down, with a maximum print depth of 38mm. The overlapping strategy is based on proximity to ensure oxidation of the molten aluminum does not impede bonding. Like the original machine, each frame

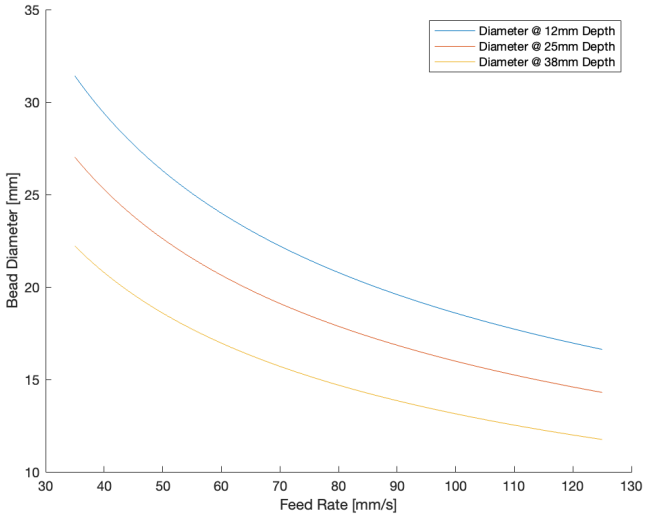

Figure 5-14: Bead Diameter Prediction
This figure shows the prediction based on augment Torricelli flow, showing bead diameters steadily decreasing with feed rate at different depths.

follows roughly similar form, differing in proportion based on the range of travel possible, X axis being the largest, and Z being the smallest. The frame assembly is shown in figure 5-16. Each frame toolpath is oriented based on assembly. With the design language shown here, myriad machine forms could be devised and printed without consequence to the printing process itself.

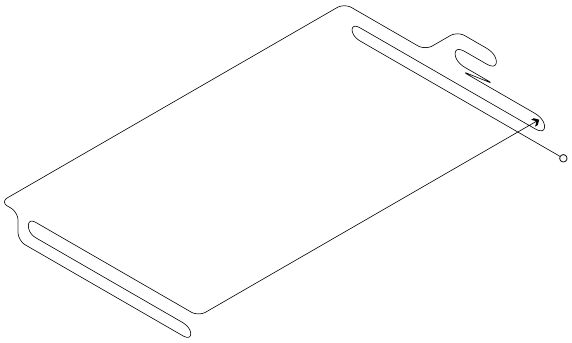

(a) X axis Base

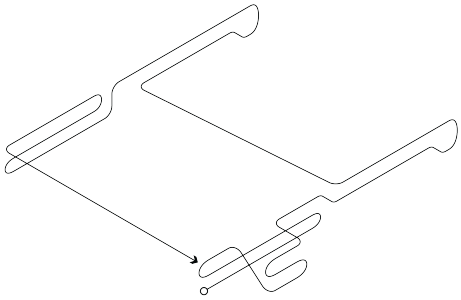

(b) Y axis Gantry

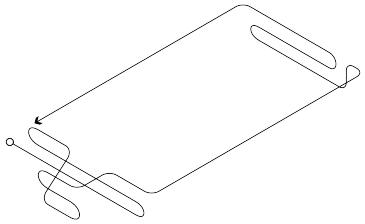

(c) Z axis Carriage

Figure 5-15: Printed TinyZ Toolpaths

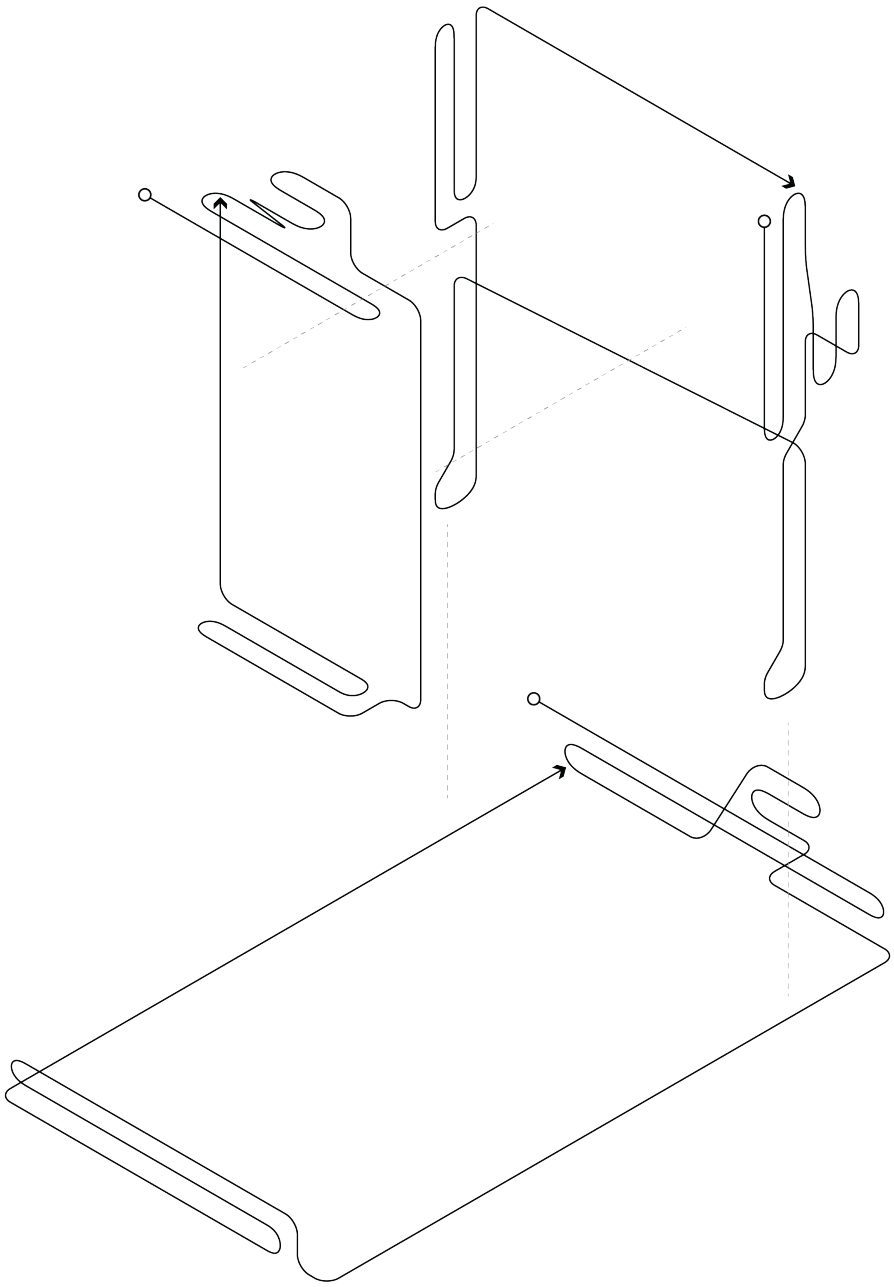

Figure 5-16: Assembled Printed TinyZ

Chapter 6

Results

6.1 Nozzle Temperature Response

The temperature response is measured using the standalone experiment setup described in section 5.1.1. The numerical simulation agrees with the experiment, with some differences likely due to geometry, nonlinearities in material properties, and input power density. Finally, the simulation here describes a simplified radially symmetric system while the reality of printing may introduce irregularities in temperature response as a consequence of printing at high speeds or through room temperature granular media. Nevertheless, the numerical simulation shown here can be a useful tool in designing nozzle assemblies and predicting their performance with reasonable accuracy on the order of $\pm 10°C$. The plot shows thermocouple readings lagging initially, behind the numerical simulation, indicating the system has more thermal capacitance in reality than what is described by the numerical simulation. Additionally, the temperature at steady state reached in roughly 30 minutes is slightly higher than the temperature provided by the numerical simulation. However, for the purpose of designing a nozzle assembly that can reach a desired temperature, this error is acceptable. Finally, it should be noted that this simulation models a static material in the nozzle shaft, ie, the material can be molten aluminum to describe the printing process, or near room temperature ceramic, which is the case for this simulation. The numerical model treats the relationship between material in the ceramic and the noz-

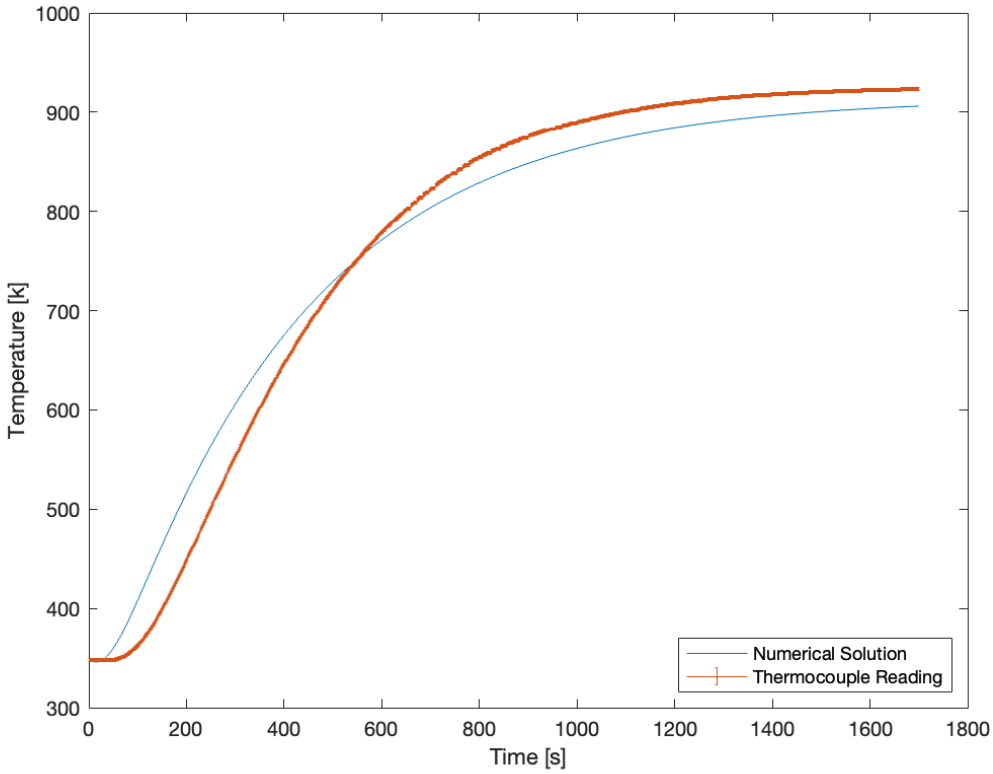

Figure 6-1: Experimental Temperature Response
This figure shows good agreement between the numerical solution and experimental data.

zle shaft as a radial conduction problem however in reality, this scenario is a forced convective condition wherein a volume of fluid material flows out of the nozzle at melt temperature either heating or cooling the surrounding nozzle shaft. The coupling of this thermal process and the fluid analysis shown next would be an interesting subject of further research, especially as this kind of coupled analysis would reflect the reality of printing with more precision.

6.2 Fluid Analysis of a Printed Bead

The results of the fluid analysis describing the LMP process is compared to experimental results. The prediction of bead diameter as a function of process parameters like nozzle geometry, feed rate and print depth are integral in understanding how to

print, building intuition about parameter sensitivities and defining resolution. The physical models underlying the LMP process can eventually be used in tool-pathing algorithms to ascribe different process parameters to different geometrical conditions, ie to produce variable thickness or to achieve target dimensions. To begin, we confirm the velocity of aluminum flowing from the nozzle orifice is laminar by computing the Reynolds number Re where ρ and μ are the density and viscosity of molten aluminum, and v_{avg} is the average velocity.

$$\mathrm{Re} = \frac{\rho v_{avg} d_o}{\mu} \tag{6.1}$$

Average velocity is computed by examining the total volume of each specimen V, and the print time t_f which is simply the length of the specimen L divided by the feed rate v_f.

$$v_{avg} = \frac{V}{A_{avg} t_f} \tag{6.2}$$

$$t_f = \frac{L}{v_f} \tag{6.3}$$

By mass continuity, the flow rate leaving the nozzle must be the same as the extrusion of the aluminum bead:

$$\dot{Q}_n = \dot{Q}_b \tag{6.4}$$

$$v_{avg} \frac{\pi d_o^2}{4} = \frac{V}{t_f} \tag{6.5}$$

Combining equations 6.1,6.3, and 6.5 gives:

$$\mathrm{Re} = \frac{4 \rho V v_f}{\pi \mu d_o L} \tag{6.6}$$

The Reynolds numbers shown in figure 6-2 for the specimens printed confirm laminar fluid flow.

We now compare the analytical solutions describing print bead geometry to the results of printed experiments. In particular, the Stokes closed form solution which describes flow restrained by viscous shear and the extended Torricelli numerical solu-

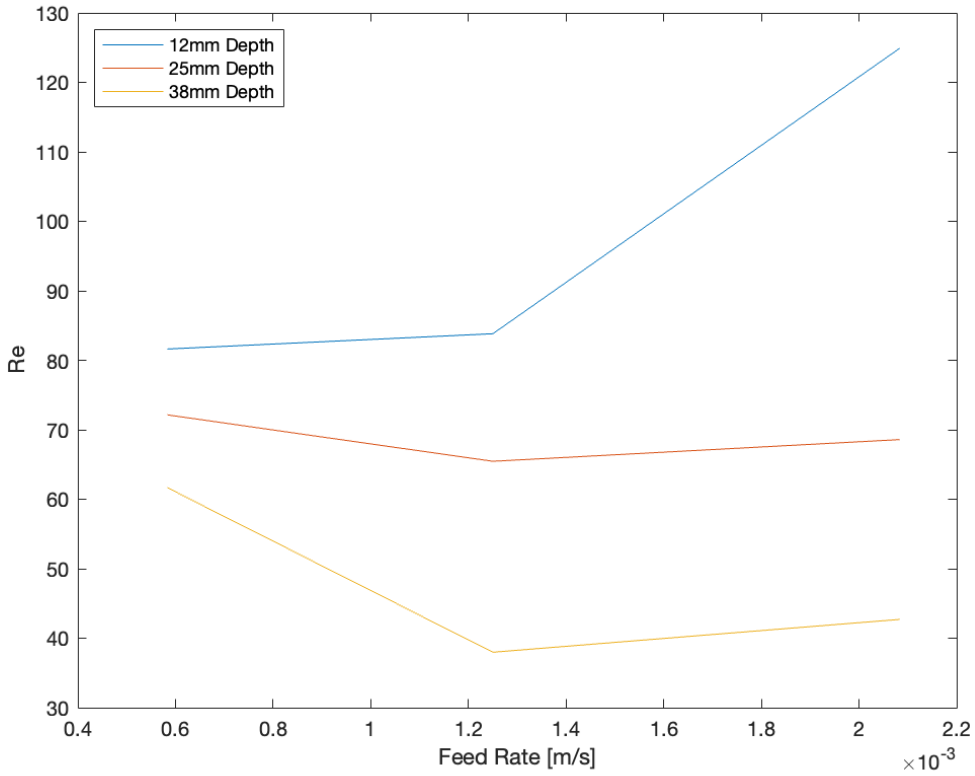

Figure 6-2: Reynolds Numbers
The calculated Reynolds numbers are well below 2000, indicating laminar flow.

tion derived from energy conservation, which considers both viscous shear and inertial force is compared.

Figures 6-3 and 6-4 show average diameter resulting from a printed volume at various feed rates and depths. Experimental measurements are compared with the numerical solutions figure 6-3 compares Stokes flow, followed by figure 6-4 which compares the augmented Torricelli flow.

Consistently, the Stokes form underestimates the volume flux at the nozzle tip, while the augmented Torricelli solution agrees with more accuracy, the experimental results. This is especially so at shallower print depths, where the inertial forces serve to displace the granular media more effectively. However at greater print depths, where the pressure head of the granular media is higher, the Stokes solution and augmented Torricelli solution agree, especially at faster feed rates. The effect of print depth and feed rate on bead diameter are well characterized by the Torricelli solution

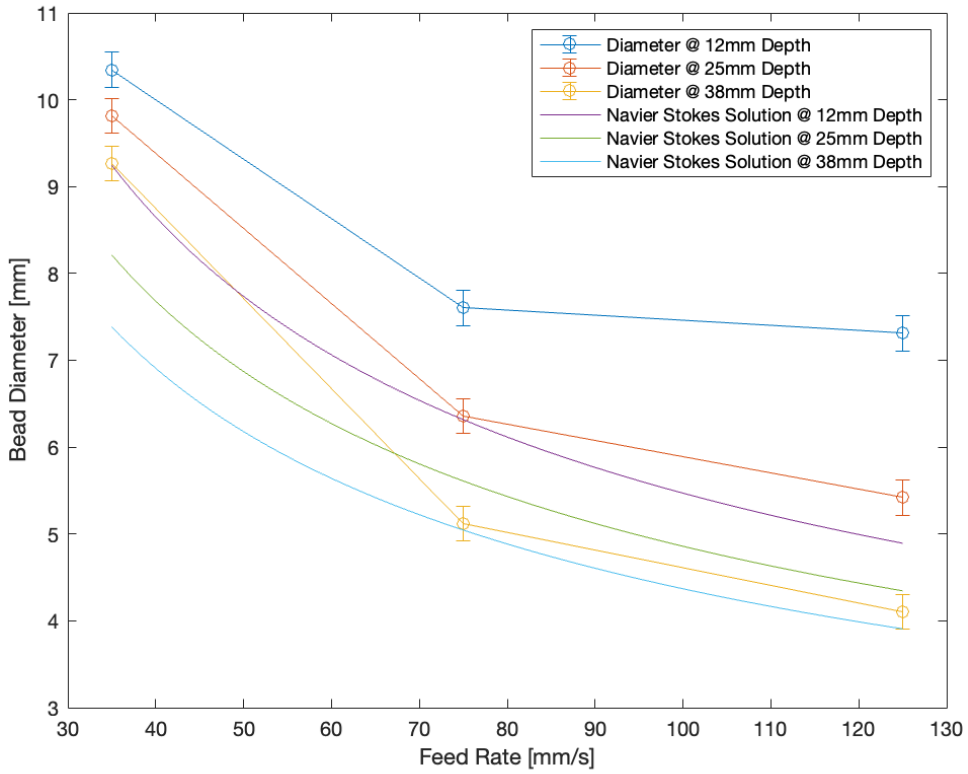

Figure 6-3: Bead Diameter and Feed rate
The Stokes solution typically underestimates volume flux and hence bead diameter.

and extremely sensitive to hydraulic diameter and pressure head at of the material in the crucible. While the nominal diameter of the bead decays more and more dramatically at faster feed rates, this suggests that potentially finer features may be printed in this manner while coarser features may be printed closer to the surface of the print bed or at very slow speeds.

The figures 6-3 and 6-4 show the bead diameter as a function of feed rate.

Figure 6-5 shows time data of volume printed at 35 mm/s at various depths and compares this data with Stokes and augmented Torricelli flows. While the average bead diameter shows the Stokes flow dramatically underestimates the resultant bead diameter, the time based data show that the Stokes flow characterizes the volume flux extremely closely. The augmented Torricelli solution is consistent in this regard between average diameter and time based volume flux data. Inconsistencies in bead diameter exist especially near the beginning and end of the toolpath. These inconsis-

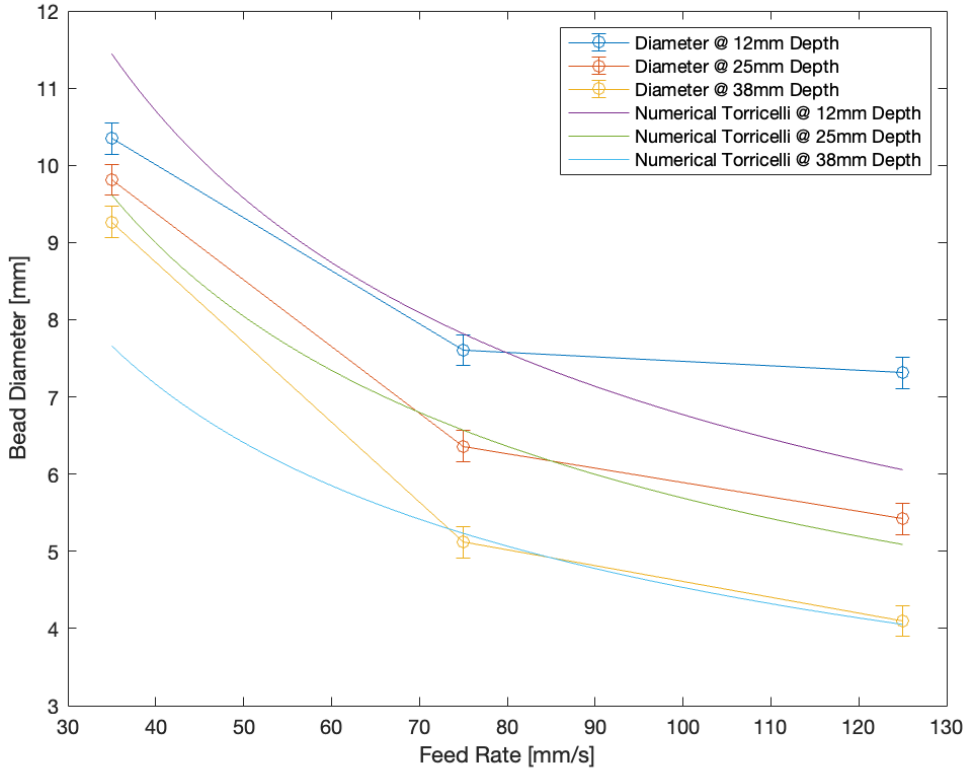

Figure 6-4: Bead Diameter and Feed rate
The Torricelli solution shows good agreement especially at faster speeds and lower print depths.

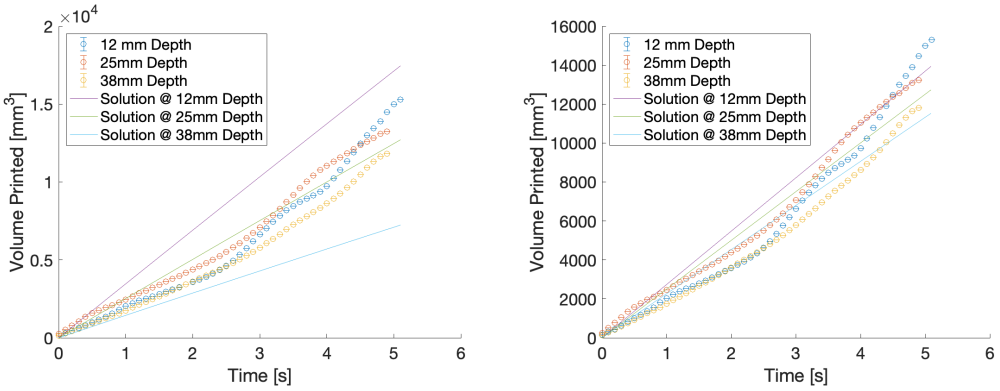

(a) Augmented Torricelli Solution (b) Stokes Solution

Figure 6-5: Volume Printed at 35 mm/s
The print speed of 35mm/s shows more of a viscous dominated regime, where the Stokes solution may be more appropriate.

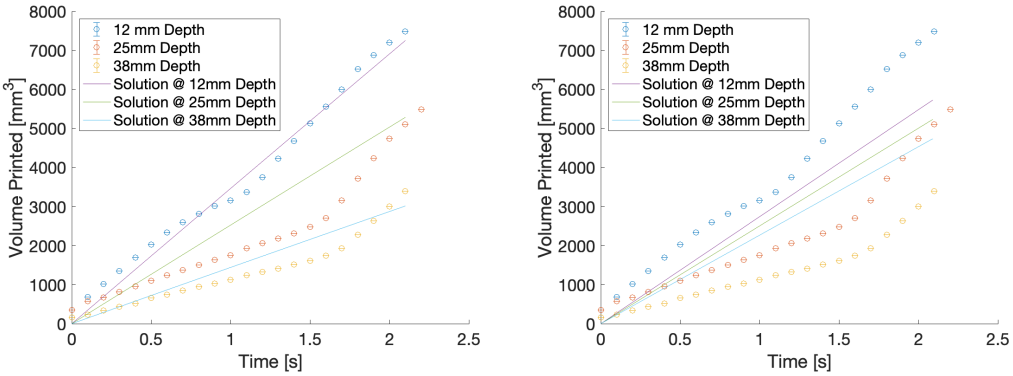

(a) Augmented Torricelli Solution (b) Stokes Solution

Figure 6-6: Volume Printed at 75 mm/s
The augmented Torricelli solution shows good correspondence with the experimental results. The Stokes solution is typically insensitive to changes in depth, indicating the relevance of inertia in the flow regime.

tencies are more noticeable closer to the surface of the print bed rather than at lower depths which remain more consistent. The following figures 6-6 and figure 6-7 show

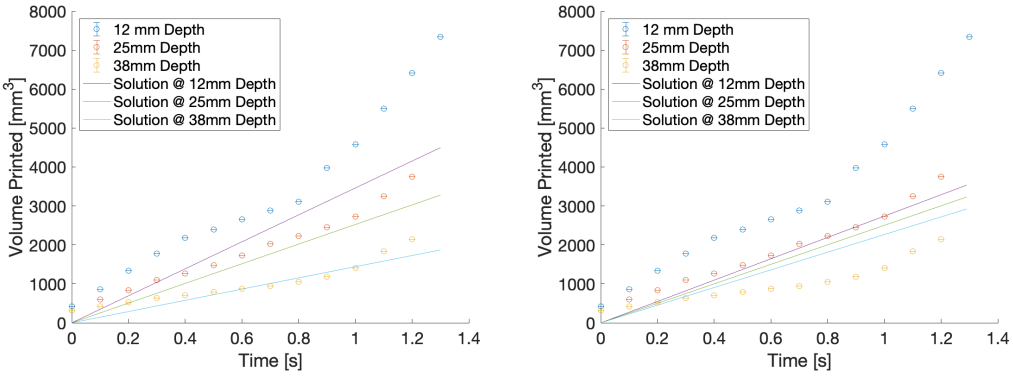

(a) Augmented Torricelli Solution (b) Stokes Solution

Figure 6-7: Volume Printed at 125 mm/s
The results for a feed rate of 125mm/s show similar correspondence as for a feed rate of 75mm/s. The flow regimes at these print speeds are similar.

good agreement between the augmented Torricelli solution and experimental results. The Stokes solution consistently underestimates volume flux except at lower depths. There is a noticeable kink in the experimental results that may account for the discrepancy of the Stokes flow to the which is a consequence of velocity ramping at the end of the toolpath and a subsequent increase in volume flux. This trend is more

noticeable at faster feedrates because the ramp is far more extreme. Furthermore the number of data points is a function of a predefined dt set for each feed rate to be 0.1 seconds. At slower feedrates like 35 mm/s, this selection is reasonable however at faster feedrates, the volume data becomes far more sparse and the effect of velocity ramping more extreme. To compensate for velocity ramping, an adaptive feedrate should be used to level out the volume flux toward the beginning and end of a print especially at faster feedrates. Additionally with finer choices of dt, characteristics like Rayleigh instability might be visible which impact the volume flux. To see the effect more clearly, consider the printed samples in figure 6-8, which shows the oscillation of print diameter and hence volume flux at the nozzle tip. The specimens analyzed here

Figure 6-8: Thin Printed Samples showing Rayleigh Instability

show similar volume flux values to numerical solutions provided by Stokes flow and augmented Torricelli flow. Ultimately there exist two regimes where inertial forces described by the augmented Torricelli solution are more appropriate or where inertial forces are less prominent and the flow is characterized more aptly with Stokes flow. These regimes are essentially related to print depth. The challenge of printing

with aluminum at greater depths is that density and hence inertia becomes far less dominant. In earlier versions of the LMP process where the feedstock was a lower melting point alloy, Pewter, the higher density enabled printing of pewter at much greater depths and faster speeds than are possible with aluminum. Hence the material properties of the feedstock play a crucial role in the volume flux at the nozzle tip and furthermore, the resolution of the printed bead.

6.3 Thermal Imaging

Preliminary results of the thermal imaging show the potential of using this technique in near real-time monitoring of printing progress. The current thermal camera saturates at $450°C$ so a color legend is omitted. Nevertheless, the relative color grading measured from the thermal camera clearly shows the outlines of printed beads very near the surface of the sand. If the print had occurred further in the print bed, or if the print bed was heated, the resulting images would be far more obscure. There is noticeable lag in the position of the tool tip and the dispensing of molten aluminum which is a measure of the time that the heat from the printed bead diffuses to the surface of the sand and is captured by the camera. While the results here show an indirect way to measure the printed bead by considering the heat diffused at the surface of the sand, this method may be coupled with thermal cameras mounted in other positions potentially as a way to arrive at a 3D result, ie through the use of photogrammetry. Additional camera angles and constructing time based 3D forms will be the subject of further research.

6.4 Tensile Testing

Structural testing of several printed and cast specimens is shown here, illustrating the effects to mechanical properties the LMP process can have on a part. Tensile tests were conducted for both printed and cast specimens, where the printed specimens were machined and used as patterns for the cast specimens. The cast specimens

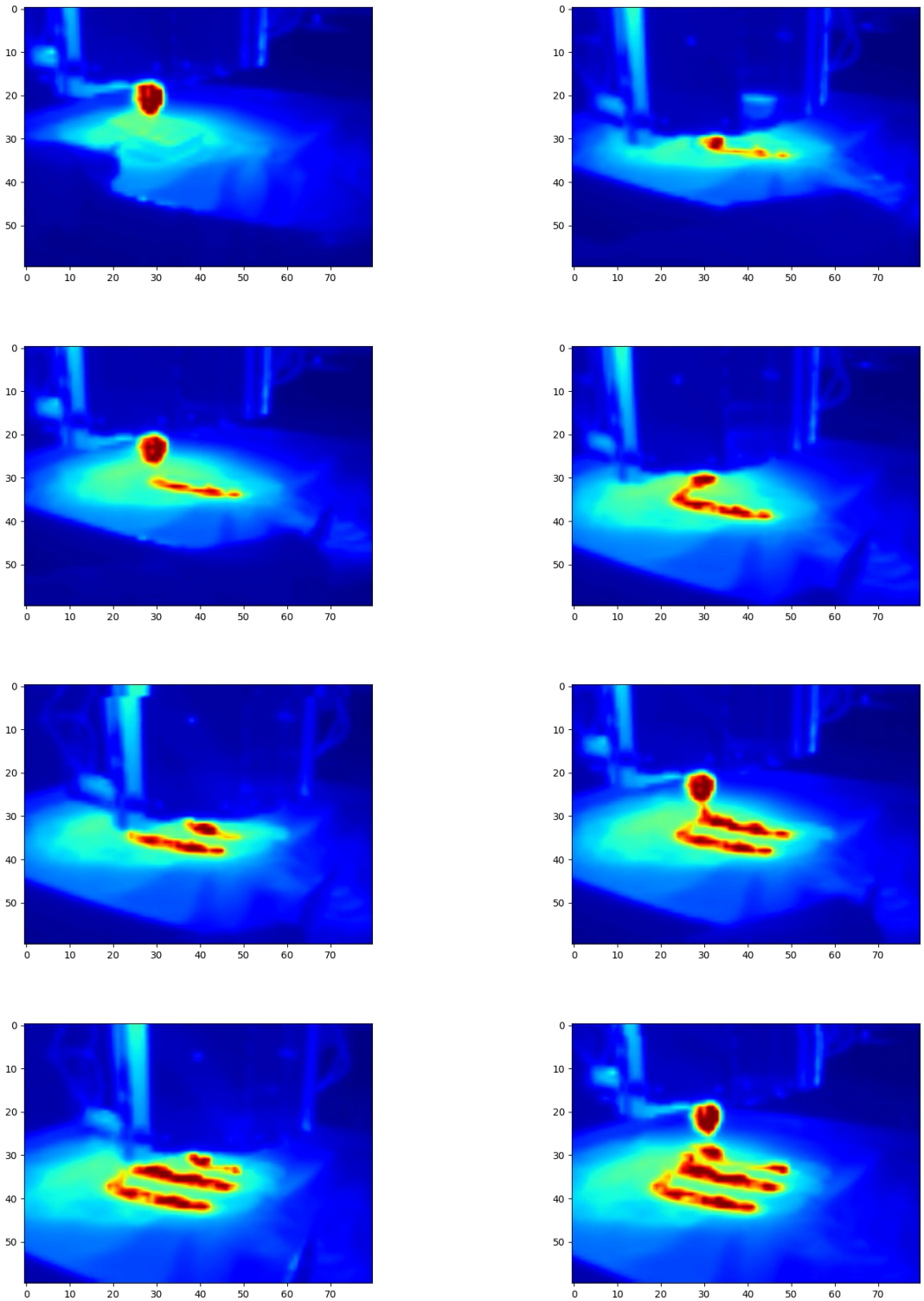

Figure 6-9: Thermal Imaging of Print Sequence

were not machined but exhibited reasonable surface finish. The elastic moduli of

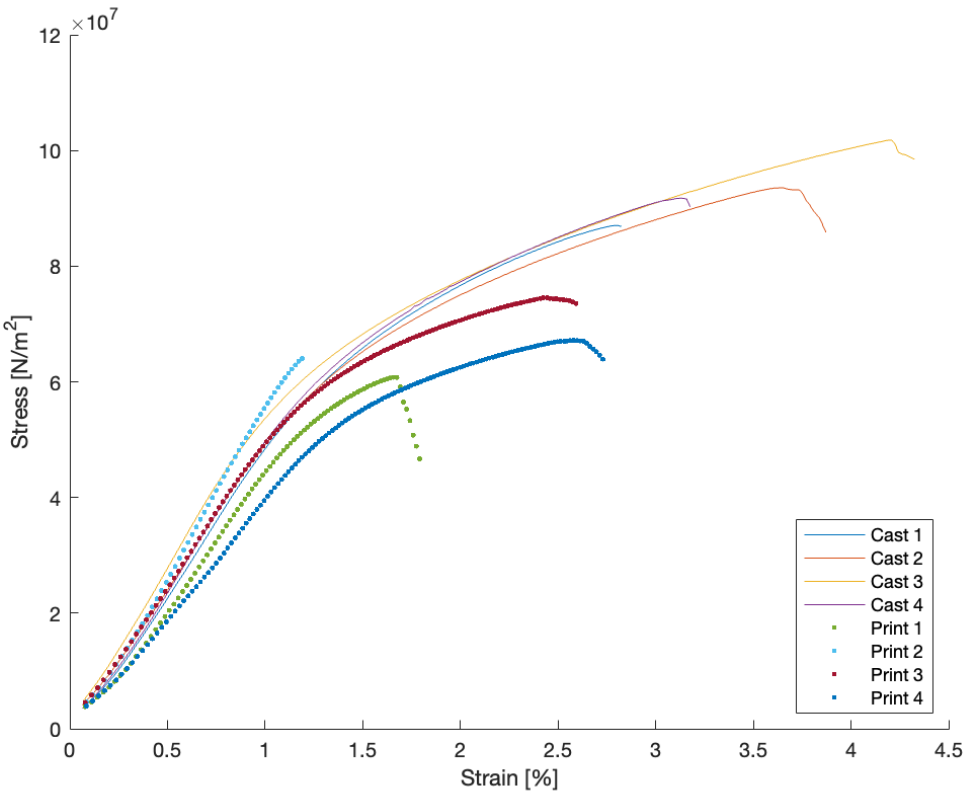

Figure 6-10: Tensile Specimen Results
This figure shows the results of printed versus cast aluminum specimens. The cast parts consistently outperform the printed parts. The printed parts suffer from brittle fracture, with very little plastic deformation.

the printed specimens are not substantially different from the cast specimens but the yield and plastic regions are wholly different. The printed specimens are embrittled, potentially by the inclusion of glass bead and air, especially when printed near the surface of the print bed. The cast specimens exhibit roughly 4% elongation over a 50mm gauge length, deforming plastically before fracturing. Comparing these results with industrially cast aluminum, the tensile strength of these specimens is roughly $\frac{1}{3}$ the strength of an alloy group 1 high strength aluminum casting alloy, which ranges from 262 - 330 MPa [33]. The cast specimens typically fail around 100 MPa, and the printed specimens fail at 74MPa. Additionally, the elasticity is roughly one tenth the elasticity of aluminum, around 6 Gpa. These results can be explained by the circum-

stances of the solidification rate, which is likely slower than in industrial processes, the careful selection of alloys, ensuring the melt is free from moisture and contaminants, and strain hardening or cold working. These factors all play some role in the determination of the final structural properties of the material.

Control of grain sizing and direction such as can be achieved with extruded and strain hardened aluminum is absent from the printing and casting process used here. Furthermore the reaction of molten aluminum being poured or printed with moisture in the air and sand mold produces hydrogen porosity which can have detrimental effect to the grain structure of the part, especially in high concentrations. This might be ameliorated by degassing of the aluminum melt which would reduce hydrogen porosity. A faster rate of solidification of the cast would improve the part performance substantially, potentially yielding finer grain size. Finally the choice of alloy have impacts on the cast-ability of the melt. The scrap used in the specimens was primarily 6061-T6 aluminum. The addition of alloying elements can improve the structural properties of aluminum, however if the solid solution is not homogenous, the structural properties are compromised. This problem could be solved by solutionize heat treating the specimens, which requires an oven with very accurate control of temperature. Comparing the cast specimen with the printed specimen shows similar elastic response and different plastic response. The main difference between the two types of specimens ultimately is the rate of solidification, the inclusion of impurities, and casting pressure. While the rate of solidification and impurities can be controlled by tighter control of the temperature of the build environment and cleanliness of melt, the casting pressure is a result of process parameters like print depth, and pressure head at the crucible. In traditional sand casting, this pressure is supplied by the height of the crucible pour and the presence of risers or other gating system components. In LMP, the "sprue" can be considered the column of aluminum flowing from the crucible through the nozzle shaft and out of the nozzle tip, so that the casting pressure in LMP along the toolpath is equivalent to the pressure drop at the sprue exit in casting. While conceptually, this should indicate higher casting pressure and hence better grain structure of the printed part, the pressure head of the glass bead does not

maintain the same conditions as can be found in a sand mold or permanent mold. In LMP the glass bead is displaced, permitting the formation of a print bead and preventing any compaction from occurring as would occur in a conventional cast. In order to replicate the higher casting pressure seen in sand casting, both the fluid column in LMP and the granular media should increase. This means a taller crucible, a denser granular medium, or printing at greater depths.

6.5 Metallography

Here a compound bead sample cross section is analyzed for evidence of glass bead inclusions or other forms of porosity. The metallography was undertaken using standard practice of machining with a cubic boron nitride saw shown in figure 6-11a, polishing with progressively higher grits of SiC paper to roughly 1200 grit shown in figure 6-11b, and finish polishing with $3\mu m$ suspended diamond polishing media. It

(a) Cutoff Saw (b) Polishing

Figure 6-11: Sample Preparation

was determined after this process that further etching was unnecessary to identify grain boundaries. Figure 6-12 shows the macro-scale cross section. Immediately it can be inferred that the presence structure of a double bead is homogeneous, no sign of a seam or joint is present, but the porosity is poor. The porosity is calculated by summation of all pixels in the image lower than some threshold, in this case 100, on a scale of 0-255. This yields a porosity map as shown in figure 6-13. The resulting porosity is roughly 3% which is an unacceptable cross sectional density for typical casting. Heat treating or hot isostatic pressing could be employed here to improve the density of parts like this. Further inspection reveals characteristics of the grain

Figure 6-12: Double Bead Cross Section

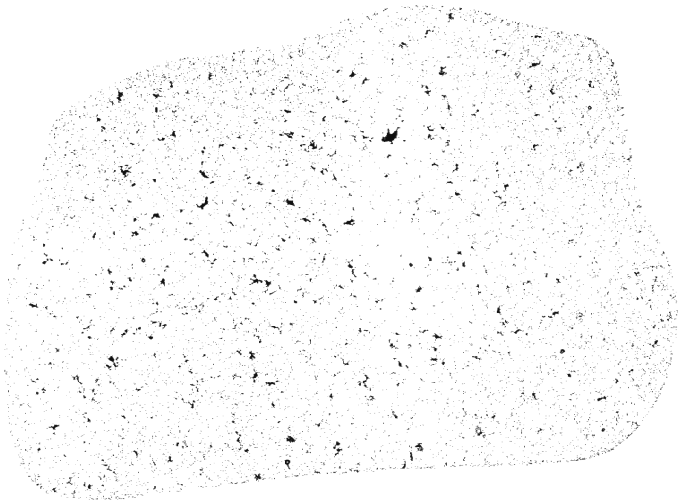

Figure 6-13: Double Bead Pores

structure, alloying elements and contaminants entrapped and partially dissolved in the melt. The alloying elements are present at so-called interdenritic locations as hypoeutectic, eutectic and hypereutectic alloys that solidify with aluminum in phases [13]. Figure 6-14a shows the dispersion of Magnesium-Silicon and Aluminum Iron Silicon and Silicon compounds at the grain boundaries. Figure 6-14b shows porosity generated from reactions with Hydrogen in the form of moisture in the air and glass bead. The dendrite cell size is significant, roughly double the size of cells produced

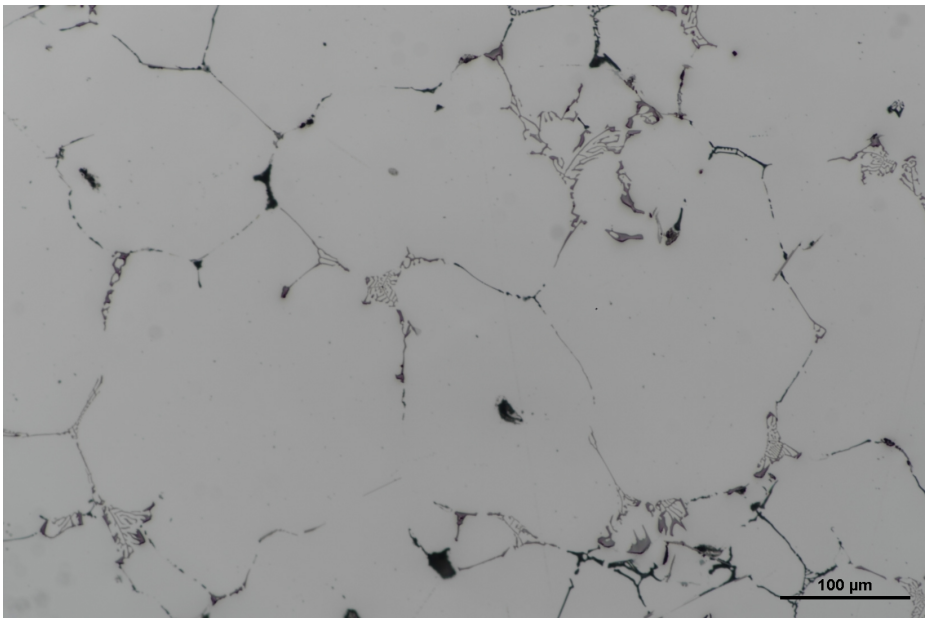

(a) Si, Mg, Fe Alloying Elements

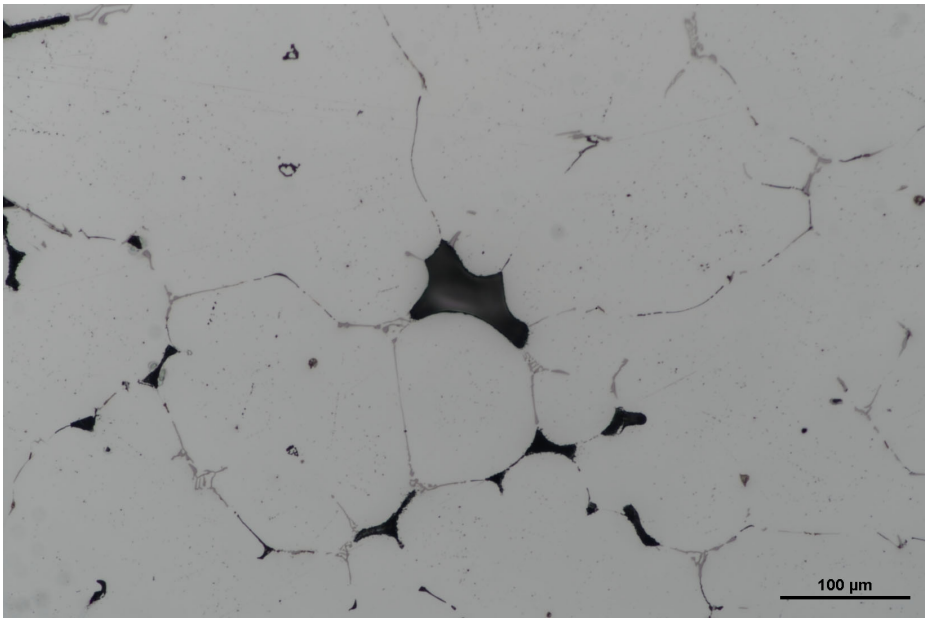

(b) Porosity

Figure 6-14: Micro-structure of Double Bead Sample

in typical of casting settings. This explains the absence of plastic behaviour in the tensile specimens, which is a function of cell size. With cell sizes of around $115\mu m$, one can expect roughly 2% elongation, which is consistent with what is observed in the tensile testing shown previously.

6.6 Geometric Experiments

Here, a series of geometric experiments are undertaken to describe the space of possible forms that LMP is capable of producing. While the numerical methods shown previously can aptly describe volume flux at the nozzle tip for straight line prints, the modelling of compound overlapping beads and abrupt changes in curvature and hence feed rate require involve more complexity. Hence empirical study of various forms and toolpath strategies is presented here.

6.6.1 Compound Beads

Printing the XY plane is shown in figure 6-15. The toolpath is sufficiently small in step-over such that bonding can occur. However, for lengths beyond 300mm, the oxide layer buildup from the previous bead becomes too excessive for bonding to occur. The samples shown in figure 6-15 are printed 15mm in depth with a feedrate of 75mm/s. While this bead diameter shows potential for structural application,

Figure 6-15: Single Bead (Bottom) and XY Compound Bead (Top)

bonding in the YZ plane is far more effective at generating width, especially at lower feed rates. The nozzle initially displaces granular media in printing the first bead, then after stepping upward in the Z and doubling back, the displaced granular media form a trough for a significant amount of molten material to fill. Figure 6-16 shows the result of bonding in the YZ plane and in the YZ and then XY plane, the former producing a thick double bead, and the latter forming an extremely thick triple bead. A section of the triple bead is shown in figure 6-17 demonstrating the bonding which

Figure 6-16: Single (Top), YZ Compound Bead (Middle), YZ and XY Compound Bead (Bottom)

occurs between the three beads. This toolpathing strategy can only occur very near the surface of the print bed. The path in the granular media carved away by the nozzle profile becomes the cross section of the triple bead. The triple beads shown here are printed at a 20mm depth, with a feed rate of 50mm/s.

(a) Cross Section (b) Elevation

Figure 6-17: Triple Bead

6.6.2 Surface Strategies

This section will describe some preliminary results of surface based experiments. The formal strategies shown here attempt to create successive layers of printed aluminum along the XY plane to produce a surface. The surface tests are ultimately unsuccessful at producing an homogeneous surface, due to the diameter of the nozzle interfering with previously printed beads. Stepping in an oblique plane or in the Z axis, as demonstrated with the triple bead experiments shown previously, may be a more appropriate strategy for large diameter nozzle geometries. Alternatively, a smaller nozzle diameter may lead to more successful overlapping at greater depths. While the in plane spiral shows clean dispensing of material, the oxide layer formed immediately after printing prevents any bonding from occurring except at the center. This is likely due to the lower feed rates as a result of smaller radii, or greater curvature. Reaching the programmed feedrate occurs across larger length scales and lower curvature. Tighter changes in direction ultimately lead to slower machine travel and hence larger diameter beads. In order to achieve more accurate control over bead diameter for curved toolpaths, it may be necessary to compensate for reduction in velocity by tuning another parameter, for example print depth. For greater curvatures, the depth of the print could be reduced. The zig zag strategy similarly suffers from oxide buildup interrupting any bonding from occuring. Instead the nozzle displaces previously dispensed material rather than joining to it. The helix test demonstrates

(a) 25mm Depth, 75mm/s, 20mm Pitch

(b) 25mm Depth, 50mm/s, 20mm Pitch

Figure 6-18: Surface Tests

(a) 25mm Depth, 75mm/s, 12mm Spacing

(b) 12mm Depth, 75mm/s, 20mm Spacing

(c) 12mm Depth, 35mm/s, 20mm Spacing

Figure 6-19: Surface Tests

overlapping in the Z axis, where the nozzle geometry does not interfere with previously laid material. The helical form shows partial bonding of layers along the Z axis. The oxide layer that forms immediately after a bead is printed prevents the bonding of subsequent beads unless it is sufficiently perturbed. Partial bonding is shown in figure 6-20b.

6.6.3 Compound Toolpath Experiments

More complex forms are shown here, which involve compound beads in the XY and YZ plane. The part shown in figure 6-21 demonstrates the possibility of combining a selection of the previous experiments together in a single print. The frame shown here combines double layer beads in the oblique plane and a helix at the center of the print to form a hole which might be precision machined later on. The bonds were successful here because of immediacy with which the nozzle doubles back on previously laid material preventing the oxide layer from fully forming. An irregular frame is shown in figure 6-22 which attempts to bond several times in the XY plane within a single print. Ultimately the final loop in the toolpath was not printed because of insufficient pressure drop in the crucible. Additionally, no bonding occurred, likely due to not only to the distance over which the bond was intended to occur but also considering the sharp changes in curvature which would have slowed the machine from its programmed feedrate thereby taking longer reconnect. Notwithstanding, the printed geometry is uniform in cross section, and capable of performing in some structural capacity. Additionally, this irregular shape is machined on a mill, to demonstrate the possibility of precision machining features of interest in an otherwise irregular or complex part. Two operations are shown here, 6-23a shows the machining of a circular through bore 2.25" in diameter. From here, threads are cut using a thread mill, an arbitrary thread geometry is chosen, $2\frac{3}{8} - 16$. The surface finish from the boring operation is good, however the thread surface finish is moderate. The part machines like soft aluminum, with chips that cling to the tool flutes with more tenacity than extruded aluminum. A chair frame is printed to demonstrate the potential for LMP printed parts to be useful in product or industrial design. Employing the compound bead strategies of

(a) Viewed from Top

(b) Viewed from Side

(c) Viewed from Alternate Side

Figure 6-20: Helix 175mm Radius, 12mm Pitch, 40mm Tall

Figure 6-21: Frame

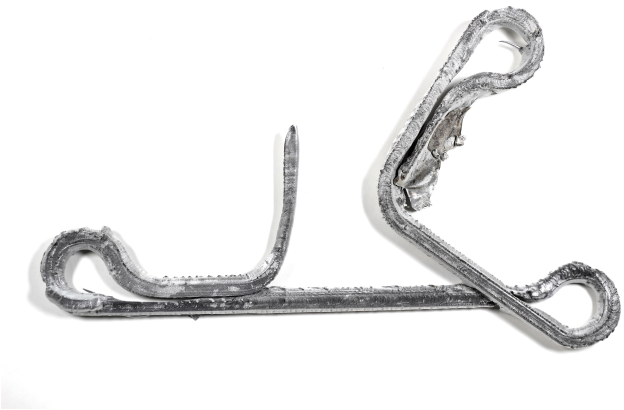

Figure 6-22: Irregular Frame

previous experiments, the chair frame shown in figure 5-12 demonstrates that variable thickness can be produced with intent, to lend additional structure or reduce weight where necessary. Thicker cross sections made by compound beads in the YZ plane are used where the seat of the chair frame meets the legs. Additionally, the chair frame back is printed with a compound bead which is later machined to accept a wooden back. This part demonstrates the potential of LMP parts to be machined sufficiently to become part of a greater assembly. The wooden seat and back are flip-milled maple with features to accept half inch square dados undersized by 0.005".

(a) Machining a Smooth Bore

(b) Thread Machining

Figure 6-23: Re-machining a Printed Part

The mating tenons for the seat and back are machined out of the aluminum frame using a flat end mill for the top surface and a woodruff keyway cutter to for the underside. The fit is sufficiently tight to warrant assembly and use without adhesive, nevertheless an epoxy is used to bond the joint permanently. The remachining of complex and irregular parts produced by LMP would require specialized fixturing in an industrial context. Additionally, an LMP part could be printed with locating features that could support easier workholding for subsequent part processing and shaping.

To demonstrate the potential of the LMP process to produce components in a mechanical assembly, a desktop scaled CNC frame is printed and machined to fit precision components like lead screws and bearings. The toolpaths for the printed TinyZ shown in the preceding chapter are complex spatial toolpaths involving bead overlaps and both positive and negative Z travel. The resulting frames generally showed successful bonding across the triple bead portions of the toolpath. Nevertheless, there are areas where due to surface wetting of the nozzle tip or oxidation of the molten aluminum bead, some joints were unsuccessful, especially where the beginning and end of the toolpath meet. Therefore, TIG welding of the unbonded segments was undertaken, in order to ensure sufficient stiffness when machining. Figure 6-26b shows the bonding failure which was a result primarily of insufficient pressure head from the crucible. This indicates that the crucible did not have sufficient material towards the end of the print to maintain the intended volume flux. Once printed, the frames are machined using various tooling and techniques. However, limitations in available

Figure 6-24: Chair Frame

Figure 6-25: Assembled Chair

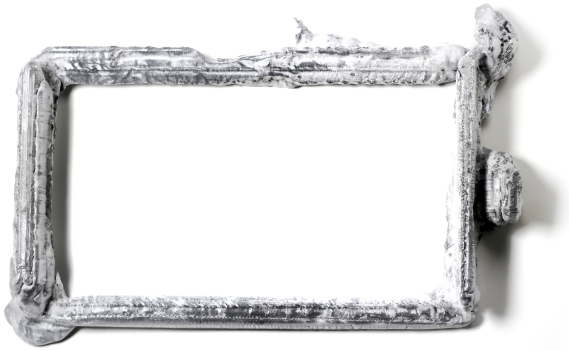

(a) X Base Frame

(b) Y Gantry Frame

(c) Z Carriage Frame

Figure 6-26: Printed Frames for Assembly

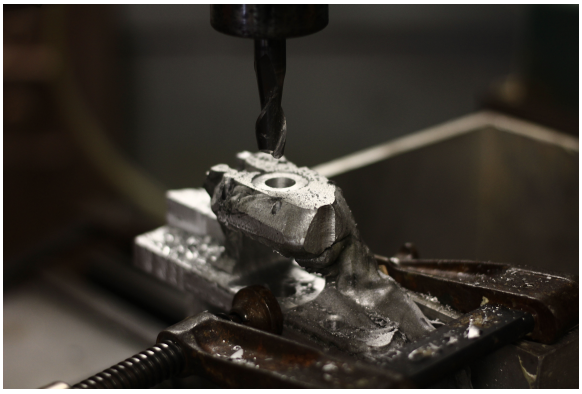

(a) Vertical Fixturing and Machining

(b) Right Angle Machining

Figure 6-27: Frame Machining

tooling and part size required reorientation of the frames, hence additional surfaces are machined to re-establish coordinate references. For example the Z and Y carriage required mounting flat to machine features for the stepper motor and flex coupling that connects the stepper motor output shaft to the lead screw. Additionally, in order to machine features for the precision ground shafts, these frames required mounting vertically. Figure 6-27a shows a typical operation involving vertical fixturing. Additional surfaces were machined on these frames to enable reorientation and referencing. The X base frame on the other hand is large enough that no reorientation of the part was required. The base frame is laid flat and conventional milling is performed. Additionally, a right angle attachment is used to machine horizontal features shown in figure 6-27b. Thus bearing races, through holes for mounting the stepper motor and precision shafts are machined in the YZ plane using a combination of manual and CNC toolpaths. The assembled printed frames are shown in figure 6-28.Levelling feet are added to the X base frame to account for the uneven underside of the print.

This part shows the minimum features necessary to participate in a fully functional machine tool assembly. A major challenge of this approach to fabricating mechanical components is the fixturing of irregular geometry. Clamping typically requires flat surfaces to ensure stability of the workholding. However this was not possible with the printed components. To accommodate variations in surface, wood was used as soft substrate to clamp against. Nevertheless, the frames generally did not sit flat, thus strategic shimming of clamped portions reduced the amount of elastic deformation that occurred from workholding. Despite the fixturing challenges the frame is reasonably square. Tramming of the machine will be done in subsequent work, to establish the quality of the machined parts. Smooth travel of the Z carriage upon the Y gantry suggests the precision rods and lead screw are sufficiently parallel. The

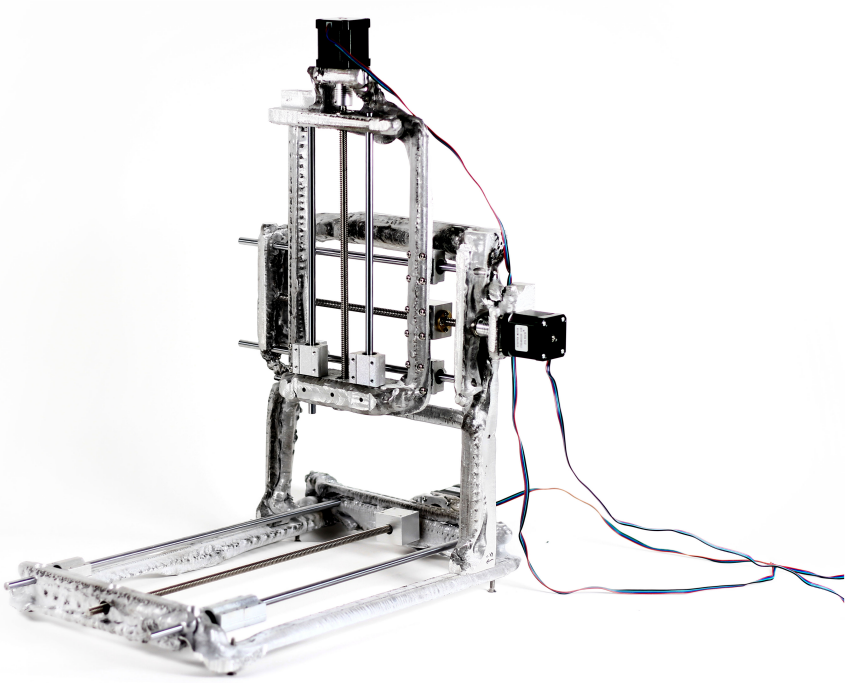

Figure 6-28: Assembled Printed Desktop CNC Machine

figure, 6-30 shows various details of the printed TinyZ, demonstrating strategies for integrating precision hardware in otherwise irregular and complex forms.

(a) Y Gantry and X Base Connection

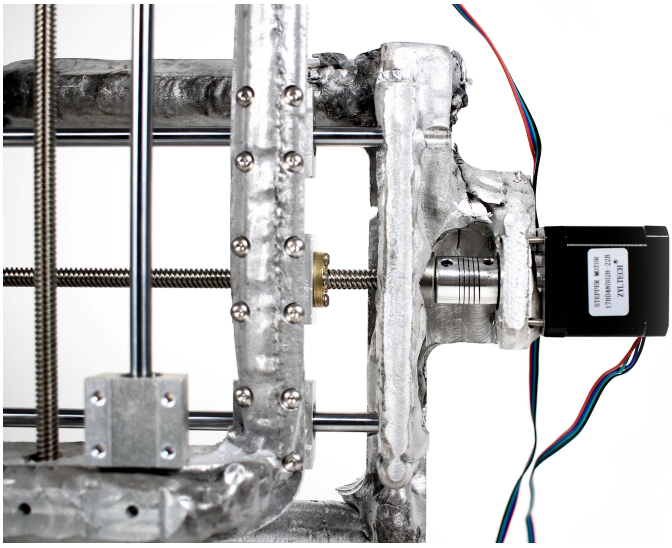

(b) Stepper Motor Mounting

Figure 6-29: Printed TinyZ Details

(a) Bearing and Actuator Components

(b) Lead Screw Mounting

Figure 6-30: Printed TinyZ Details

Chapter 7

Discussion and Conclusion

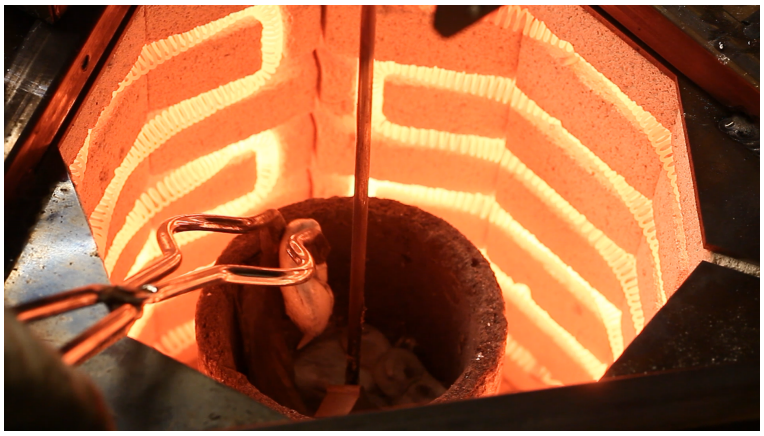

Figure 7-1: Furnace Melt

The design and fabrication of a metal additive manufacturing machine for high melting point materials such as aluminum, was demonstrated in a process called Liquid Metal Printing, originally developed by the Self Assembly Lab for printing low melting point alloys. This configuration of the LMP machine is capable of printing at process rates rivalling conventional manufacturing processes at scales comparable to those of conventional casting and injection molding. However, the resolution of parts printed with LMP are decidedly coarse. Nevertheless, the experiments show good machine-ability of printed components and the possibility of precision forming of sensitive features to enable LMP printed parts to participate in larger assemblies. The cost involved in this process is minimal, with feedstock recycled to produce new

prints. While the performance of the printed parts precludes their use as structure, the tuning of process parameters heat treatment may yield more favorable results enabling LMP to produce high strength components. Experimentation with heat treatment regimes will be the subject of future research.

Furthermore, a series of analytical models have been proposed to characterize the underlying process physics of LMP which is very similar to casting. The thermal response of the nozzle is characterized by a finite difference scheme involving heat diffusion across the nozzle geometry with radiation and convective heat loss at the nozzle surface. This numerical tool can be used to further refine and support nozzle related design decisions. The numerical tool is validated against experimental results. Additionally two fluid models have been proposed to predict print bead and hence resolution as a function of several process parameters. The models based on energy head and differential fluid analysis both capture essential elements of the printing process. These models can be useful in developing path planning algorithms and parameter tuning of toolpath strategies, such as ideal feed rate and print depth to achieve a particular part geometry.

Additionally a method for evaluating real-time print progress is proposed, with a proof of concept experiment demonstrated, that is thermal imaging of the print sequence. This strategy can be used to validate subsequent fluid simulations of complex toolpaths, especially where the numerical models described earlier may not generalize. As demonstrated in the geometric experiments, the complexity of fluid flow with toolpaths of varying print depth, curvature and feed rate, in addition to solidification rate and oxidation of the print, require trial and error experimentation. A multi-physics simulation describing the thermal, fluid, and rigid body dynamics of the nozzle, granular media, and molten aluminum will be necessary to fully predict the outcome of a print. The real-time validation of such a simulation may be accomplished with thermal imaging and potentially with its extension using multiple thermal cameras, thermal photogrammetry.

Finally a series of large scale print experiments were undertaken to assess the feasibility of prototyping products with LMP. A chair was produced which demon-

Figure 7-2: Flat to Form Pewter Chairs

strates the capability of the machine to print large single layer structures capable of performing in domestic scenarios. Furthermore the coupling of the LMP process with conventional and more precise methods of forming and shaping is demonstrated by the joining of metal printed chair frames with conventionally machined hardwood. The possibility that LMP could be coupled with metal machining has been explored. Bending or forming operations have also been explored in a previous iteration of the machine to produce products shown in 7-2. These pewter frames were printed flat and bent into shape. The possibility of plastically deforming 2D single layer structures into 3D is an extremely promising prospect for the LMP process which has not yet achieved full 3D printing. This capability is also absent from the current metal feedstock, aluminum, which has significantly reduced plasticity by the printing process. This is shown in the tensile test responses and in the examination of the grain structure. With tighter control over the solidification rate and casting pressure, and potentially with solutionize heat treating, the plasticity of printed aluminum parts can be regained.

In conclusion, a novel manufacturing technique, LMP has been advanced by the

redesign of several hardware components, the process and outputs have been characterized using a holistic framework for comparing additive manufacturing technologies, and potential application spaces have been identified. LMP holds the potential to become a disrupting and productive force in the landscape of manufacturing and design, both as a tool for prototyping, and as an exemplar of large scale circular production.

Bibliography

[1] ASTM B557-15 Standard Test Methods for Tension Testing Wrought and Cast Aluminum and Magnesium Alloy Products (Metric).

[2] Rohit Agrawal and Vinodh S. State of art review on sustainable additive manufacturing. *Rapid Prototyping Journal*, 25(6):1045–1060, July 2019.

[3] D. Altenpohl. *Aluminum Viewed from Within*. Aluminum-Verlag, Dusseldorf, 1982.

[4] D Altenpohl. *Aluminum: Technology, Application, and Environment*. The Minerals and Metals Society, 6 edition, 1998.

[5] Troy Y. Ansell. Current Status of Liquid Metal Printing. *Journal of Manufacturing and Materials Processing*, 5(2):31, April 2021.

[6] Mark Armstrong, Hamid Mehrabi, and Nida Naveed. An overview of modern metal additive manufacturing technology. *Journal of Manufacturing Processes*, 84:1001–1029, December 2022.

[7] M. F. Ashby. *Materials selection in mechanical design*. Butterworth-Heinemann, Burlington, MA, 4th ed edition, 2011. OCLC: ocn639573741.

[8] Ralph Baker. METHOD OF MAKING DECORATIVE ARTICLES.

[9] Hiram Brown. *Aluminum and its Applications*. Pitman Publishing Corporation, New York, 1948.

[10] Penrose Cdb. 2022 GLOBAL STATUS REPORT FOR BUILDINGS AND CONSTRUCTION. 2022.

[11] Wen Chen, Luke Thornley, Hannah G. Coe, Samuel J. Tonneslan, John J. Vericella, Cheng Zhu, Eric B. Duoss, Ryan M. Hunt, Michael J. Wight, Diran Apelian, Andrew J. Pascall, Joshua D. Kuntz, and Christopher M. Spadaccini. Direct metal writing: Controlling the rheology through microstructure. *Applied Physics Letters*, 110(9):094104, February 2017.

[12] C.R. Cunningham, S. Wikshåland, F. Xu, N. Kemakolam, A. Shokrani, V. Dhokia, and S.T. Newman. Cost Modelling and Sensitivity Analysis of Wire and Arc Additive Manufacturing. *Procedia Manufacturing*, 11:650–657, 2017.

[13] J.R. Davis. *Aluminum and Aluminum Alloys*. ASM Materials Information Society, Materials Park, Ohio, 1993.

[14] Lei Di and Yiran Yang. Cost Modeling and Evaluation of Direct Metal Laser Sintering with Integrated Dynamic Process Planning. *Sustainability*, 13(1):319, December 2020.

[15] Merton C. Fleming. *Solidification Processing*. McGraw-Hill Book Company, New York, 1974.

[16] Annamaria Gisario, Michele Kazarian, Filomeno Martina, and Mehrshad Mehrpouya. Metal additive manufacturing in the commercial aviation industry: A review. *Journal of Manufacturing Systems*, 53:124–149, October 2019.

[17] Timothy Gutowski, Sheng Jiang, Daniel Cooper, Gero Corman, Michael Hausmann, Jan-Anders Manson, Timo Schudeleit, Konrad Wegener, Matias Sabelle, Jorge Ramos-Grez, and Dusan P. Sekulic. Note on the Rate and Energy Efficiency Limits for Additive Manufacturing: Rate and Energy Efficiency Limits for AM. *Journal of Industrial Ecology*, 21(S1):S69–S79, November 2017.

[18] Nicholas Hoye, Hui Jun Li, Dominic Cuiuri, and Anna M. Paradowska. Measurement of Residual Stresses in Titanium Aerospace Components Formed via Additive Manufacturing. *Materials Science Forum*, 777:124–129, February 2014.

[19] Saeedeh Imani Moqadam, Lutz Mädler, and Nils Ellendt. A High Temperature Drop-On-Demand Droplet Generator for Metallic Melts. *Micromachines*, 10(7):477, July 2019.

[20] J.C. Ion, H.R. Shercliff, and M.F. Ashby. Diagrams for laser materials processing. *Acta Metallurgica et Materialia*, 40(7):1539–1551, July 1992.

[21] Zain Karsan. TinyZ: A Desktop CNC Machine to Enable Remote Digital Fabrication. In *Realignments: Towards Critical Computation [Proceedings of the 41st Annual Conference of ACADIA]*, Online and Global, October 2021.

[22] K. Bel Knani and James M. Boileau. *Developments in Lightweight Aluminum Alloys for Automotive Applications: 2001-2005*. Society of Automotive Engineers, Warrendale, USA, pt-130 edition, 2006.

[23] Don S. Lemons, Trevor C. Lipsombe, and Rickey J. Faehl. Vertical quasistatic Poiseuille flow: Theory and experiment. *American Journal of Physics*, 90(1):59–63, January 2022.

[24] Ming Li, Wenchao Du, Alaa Elwany, Zhijian Pei, and Chao Ma. Metal Binder Jetting Additive Manufacturing: A Literature Review. *Journal of Manufacturing Science and Engineering*, 142(9):090801, September 2020.

[25] Z.Y. Liu, C. Li, X.Y. Fang, and Y.B. Guo. Energy Consumption in Additive Manufacturing of Metal Parts. *Procedia Manufacturing*, 26:834–845, 2018.

[26] Haoyang Luo, Xing Sun, Le Xu, Wei He, and Xiaoyu Liang. A review on stress determination and control in metal-based additive manufacturing. *Theoretical and Applied Mechanics Letters*, 13(1):100396, January 2023.

[27] John O. Milewski. *Additive Manufacturing of Metals*, volume 258 of *Springer Series in Materials Science*. Springer International Publishing, Cham, 2017.

[28] Chong Peng, Ling Zhan, Wei Wu, and Bingyin Zhang. A fully resolved SPH-DEM method for heterogeneous suspensions with arbitrary particle shape. *Powder Technology*, 387:509–526, July 2021.

[29] Cyril Santos, Daniel Gatões, Fábio Cerejo, and Maria Teresa Vieira. Influence of Metallic Powder Characteristics on Extruded Feedstock Performance for Indirect Additive Manufacturing. *Materials*, 14(23):7136, November 2021.

[30] Skylar Tibbits, Jared Laucks, Bjorn Sparmann, Schendy Kernizan, Miya Nobuhiro, and Masaki Otomori. Liquid Metal Printing, April 2021.

[31] Alexander H. Slocum. *Precision machine design*. Prentice Hall, Englewood Cliffs, N.J, 1992.

[32] Ming Tang, P. Chris Pistorius, and Jack L. Beuth. Prediction of lack-of-fusion porosity for powder bed fusion. *Additive Manufacturing*, 14:39–48, March 2017.

[33] Kent Van Horn. *Aluminum Fabrication and Finishing*, volume 3. American Society for Metals, Metals Park, Ohio, 1967.

[34] Frank White. *Fluid Mechanics*. McGraw-Hill Book Company, 1979.

[35] I. Yadroitsev, P. Krakhmalev, I. Yadroitsava, S. Johansson, and I. Smurov. Energy input effect on morphology and microstructure of selective laser melting single track from metallic powder. *Journal of Materials Processing Technology*, 213(4):606–613, April 2013.

[36] Li Yang, Keng Hsu, Brian Baughman, Donald Godfrey, Francisco Medina, Mamballykalathil Menon, and Soeren Wiener. *Additive Manufacturing of Metals: The Technology, Materials, Design and Production*. Springer Series in Advanced Manufacturing. Springer International Publishing, Cham, 2017.